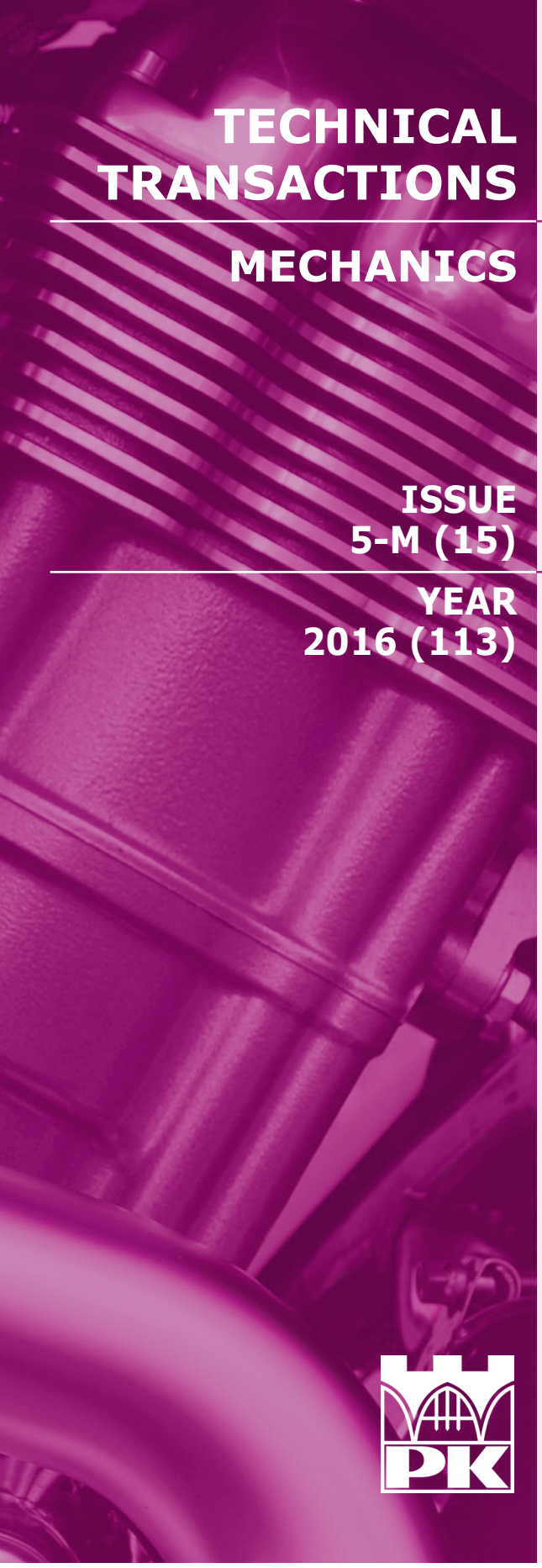

TECHNICAL TRANSACTIONS

CZASOPISMO TECHNICZNE

MECHANICS

MECHANIKA

ISSUE 5-M (15)

ZESZYT 5-M (15)

YEAR 2016 (113)

ROK 2016 (113)

WYDAWNICTWO POLITECHNIKI KRAKOWSKIEJ

TECHNICAL TRANSACTIONS | CZASOPISMO TECHNICZNE

MECHANICS | MECHANIKA

ISSUE 5-M (15) | ZESZYT 5-M (15)
YEAR 2016 (113) | ROK 2016 (113)

Basic version of each Technical Transactions magazine is its online version
Pierwotną wersją każdego zeszytu Czasopisma Technicznego jest jego wersja online
www.ejournals.eu/Czasopismo-Techniczne www.technicaltransactions.com www.czasopismotechniczne.pl

TECHNICAL TRANSACTIONS | CZASOPISMO TECHNICZNE
MECHANICS | MECHANIKA
5-M/2016

DOI: 10.4467/2353737XCT.16.281.6113

NIRESH BEHARI*, MARCIN NOGA**

VIBRATION TRANSMISSIBILITY BEHAVIOUR OF SIMPLE BIODYNAMIC MODELS USED IN VEHICLE SEAT DESIGN

PRZENOSZENIE DRGAŃ W PROSTYCH MODELACH BIODYNAMICZNYCH UŻYWANYCH W PROJEKTOWANIU FOTELI DLA POJAZDÓW

A b s t r a c t

Five biodynamic models are investigated to approximate vertical seat vibration transmissibility and mechanical impedance in an effort to reduce experimental time and data collection when designing vehicle seats. The research has found that these biodynamic models of two, three and four degrees of freedom are ideally suited for initial seat design, since whole body vibrations can be easily depicted at approximately 5Hz. Further research is necessary to investigate the resonant frequencies for defined anatomical structures, passenger variability and the use of a backrest support.

Keywords: biodynamic model, vehicle seat, vibration transmissibility, mechanical impedance

S t r e s z c z e n i e

W artykule przedstawiono porównanie przenoszenia drgań oraz impedancji mechanicznej dla pięciu prostych modeli biodynamicznych używanych w procesie projektowania foteli dla pojazdów. Przedstawione modele są używane w obliczeniach w celu ograniczenia czasu badań eksperymentalnych i zbierania danych podczas procesu projektowania produktu. Badania wykazały, że porównywane modele o dwóch, trzech i czterech stopniach swobody dają bardzo dobre wyniki na wstępnym etapie projektowania siedzeń. Analiza wykazała, że dalsze prace są potrzebne do zbadania częstotliwości rezonansowych dla określonych cech budowy anatomicznej oraz różnych cech osobniczych dla populacji pasażerów.

Słowa kluczowe: modele biodynamiczne, siedzenia pojazdów, przenoszenie drgań, impedancja mechaniczna

* M.Sc. Eng. Niresh Behari, Oman LNG, Department of Process Safety Engineering.
** Ph.D. Eng. Marcin Noga, Institute of Automobiles and Internal Combustion Engines, Faculty of Mechanical Engineering, Cracow University of Technology.

1. Introduction

The human body is exposed to various whole body vibration inputs from vehicles on a daily basis. These vibrations cause: increased driver fatigue; poor concentration during driving, pain and discomfort experienced in the lower back and neck regions, depending upon the exposure duration and magnitude [6, 11, 2, 7]. It is therefore critical that whole body vibration are limited or eliminated on vehicle seats.

The development of an idealized seat has prompted many researchers to measure vertical vibration transmissibility for the seated human; however, such measurements are inefficient and expensive, and do not adequately represent the physiological and psychological reactions of a person [7]. The utilization of biodynamic models to perform simulations during the seat design process is thus a useful and inexpensive tool that can be used in different vibration environments without the need of costly experiments or using commercially available software.

2. Biodynamic Models and Vibration Transmissibility Behavior

Five biodynamic models with equations of motion given in equations (1) to (11) are proposed to simulate vibration seat transmissibility with mechanical impedance associated with major body resonances, and compared to experimental data and published standards. The aim of this paper is to compare different biodynamic models subjected to vertical seat vibration, which are confined between two to four degrees of freedom (DOF) in order to find a simple and reliable model that can adequately simulate the vertical vibration transmissibility and mechanical impedance properties of a human for the purpose of initial seat design.

2.1. 2-DOF Model by Griffin (1990)

Fig. 1 below consists of 3 masses where m_1 lacks anatomical description and m_2 represents the feet, supported by a footrest.

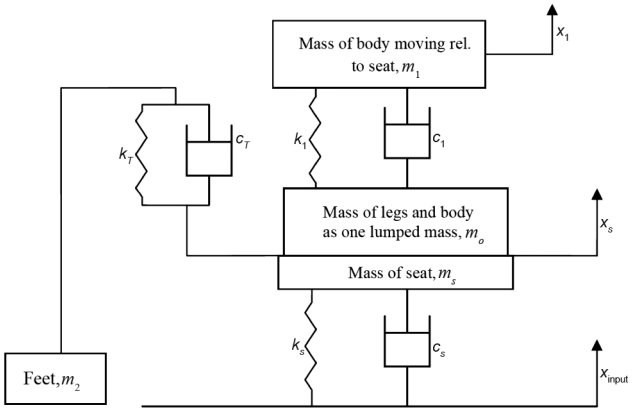

Fig. 1. Schematic of 2 DOF model by Griffin

The thigh stiffness and damping k_T and c_T as well as mass m_2 are neglected since the footrest moves in phase with the seat [4] whereas the legs and thighs are considered as one lumped mass m_o, which does not move relative to the seat. Equations of motion for this model are shown below – (1) and (2).

$$m_1 x_1 = k_1 \left(x_s - x_1\right) + c_1 \left(\dot{x}_s - \dot{x}_1\right) \tag{1}$$

$$\left(m_o + m_s\right) \ddot{x}_s = k_1 \left(x_1 - x_s\right) + k_s \left(x_{input} - x_s\right) + c_1 \left(\dot{x}_1 - \dot{x}_s\right) + c_s \left(\dot{x}_{input} - \dot{x}_s\right) \tag{2}$$

The 2 DOF model is designed to simulate the driving point mechanical impedance and behavior of vibration transmissibility response from the seat person interface to the rest of the human body.

2.2. 2-DOF Model by Rakheja, Afework, and Sankar (1994)

The model shown in Fig. 2 characterizes the dynamics of the upper torso, whereas the buttocks, legs and skeletal frame are treated as a lumped mass. The mass m_o is the driver's buttocks and legs supported by the seat, and the displacement $(x_1–x_s)$ represents the displacement of the pelvis, abdomen, chest and head mass m_1 with relation to the seat.

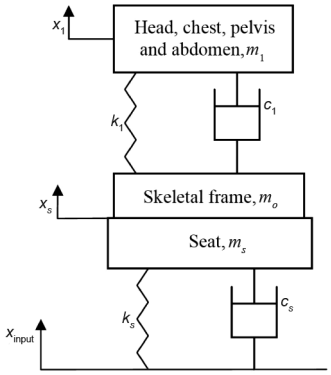

Fig. 2. Schematic of 2 DOF model by Rakheja et al.

The parameters k_1 and c_1 are the stiffness and damping coefficients of the human body model from [10]. This model can be used to predict both driving point mechanical impedance and vertical vibration transmissibility. The equations of motion for this model are identical to (1) and (2).

2.3. 3-DOF Model by Cho and Yoon (2001)

Fig. 3 shows the mass m_o, which represents the main body comprising the legs, lower torso, upper torso and arms. The mass m_1 represents the head and is connected to the main body by a neck spring k_1 and damper c_1. The main body is then connected to the hip having stiffness and damping of k_2 and c_2 respectively.

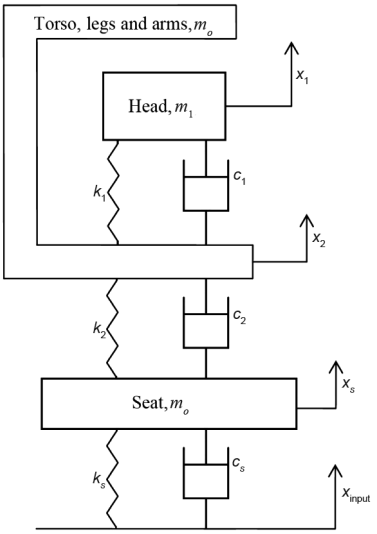

Fig. 3. Schematic of 3 DOF Model by Cho et al.

The foot is assumed negligible mass and is excluded. This model is used for vertical seat transmissibility behavior for initial seat design and excludes a backrest from [3]. The equations of motion for this model are described as (3), (4) and (5).

$$m_1 x_1 = k_1 \left(x_2 - x_1\right) + c_1 \left(\dot{x}_2 - \dot{x}_1\right) \tag{3}$$

$$m_o x_2 = k_1 \left(x_1 - x_2\right) + c_1 \left(\dot{x}_1 - \dot{x}_2\right) + k_2 \left(x_s - x_2\right) + c_2 \left(\dot{x}_s - \dot{x}_2\right) \tag{4}$$

$$m_s x_s = k_2 \left(x_2 - x_s\right) + c_2 \left(\dot{x}_2 - \dot{x}_s\right) + k_s \left(x_{input} - x_s\right) + c_s \left(\dot{x}_{input} - \dot{x}_s\right) \tag{5}$$

2.4. 3-DOF Model by Patten and Pang (1998)

Fig. 4 shows the head and neck regions, represented by mass m_1, whereas the lower torso is represented by mass m_2. Both m_1 and m_2 are connected to the seat by a rigid skeletal frame with negligible mass.

This model assumes the human is a lumped mass dispersed over the entire area of the seat cushion [8] and used to predict vibration transmissibility arising from the seat-person interface since the skeletal frame is entirely supported by the seat.

The seat-person contact area is also increased depending on the magnitude of masses m_1 and m_2. The model can be used for different types of vehicle seat suspensions and for the design of non-linear foam based seat cushions [8]. The sets of equations describing this model are presented below as (6), (7) and (8).

$$m_1 x_1 = k_1 \left(x_s - x_1\right) + c_1 \left(\dot{x}_s - \dot{x}_1\right) \tag{6}$$

$$m_2 \ddot{x}_2 = k_2 \left(x_s - x_2 \right) + c_2 \left(\dot{x}_s - \dot{x}_2 \right) \tag{7}$$

$$\begin{aligned} m_s \ddot{x}_s &= k_2 \left(x_2 - x_s \right) + c_2 \left(\dot{x}_2 - \dot{x}_s \right) + k_1 \left(x_1 - x_s \right) + \ldots \\ &\ldots + c_1 \left(\dot{x}_1 - \dot{x}_s \right) + k_s \left(x_{input} - x_s \right) + c_s \left(\dot{x}_{input} - \dot{x}_s \right) \end{aligned} \tag{8}$$

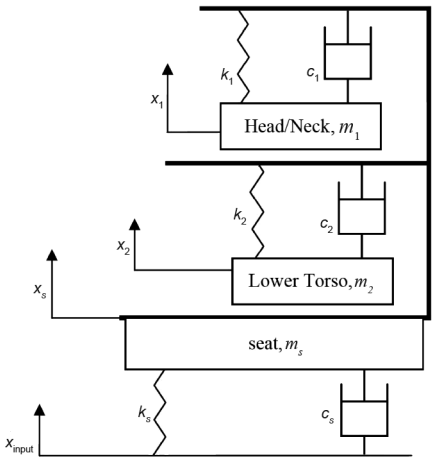

Fig. 4. Schematic of 3 DOF model by Patten et al.

2.5. 3-DOF Model proposed by Rakheja et al. (1994) and Cho et al. (2001)

Fig. 5 comprises 2 masses suspended from a common skeletal frame, representing the rigid spinal column supported by a backrest. Mass m_1 represents the pelvis and abdomen, while mass m_2 are contributions of the head and chest. Mass m_o includes the buttocks and legs, whereas the arms and feet are excluded from this model. Since mass m_o is situated directly above the seat and thigh-seat contact surface area increases, the model can predict, on a linear basis, the seat transmissibility and mechanical impedance response behaviors. A non-linear modelling strategy is recommended for the response of the cushion, especially for old seats where the cushion has bottomed out.

The set of equations describing vertical motion in the 3-DOF models proposed by Rakheja et al. and Cho et al. is presented below as (9), (10) and (11).

$$m_2 \ddot{x}_1 = k_2 \left(x_s - x_1 \right) + c_2 \left(\dot{x}_s - \dot{x}_1 \right) \tag{9}$$

$$m_1 \ddot{x}_2 = k_1 \left(x_s - x_2 \right) + c_1 \left(\dot{x}_s - \dot{x}_2 \right) \tag{10}$$

$$\begin{aligned} \left(m_o + m_s \right) \ddot{x}_s &= k_1 \left(x_2 - x_s \right) + c_1 \left(\dot{x}_2 - \dot{x}_s \right) + k_2 \left(x_1 - x_s \right) + c_2 \left(\dot{x}_1 - \dot{x}_s \right) \ldots \\ &+ k_s \left(x_{input} - x_s \right) + c_s \left(\dot{x}_{input} - \dot{x}_s \right) \end{aligned} \tag{11}$$

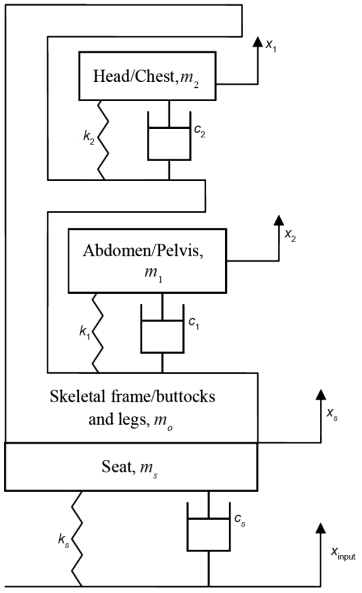

Fig. 5. Schematic of 3 DOF Model by Rakheja et al. and Cho et al.

3. Results and comparison of models

A Laplace Transform was applied to the governing equations to derive the seat to head transmissibility and mechanical impedance versus frequency. The parameters referenced in Table 1 were based on experiments related to stiffness, damping and masses of various body ligaments within the range of 44 to 76 kg. The seat stiffness, mass and damping values from [4] were made constant for all models in order to compare vertical transmissibility and mechanical impedance behavior for the various biodynamic models and experimental results.

Table 1

Biodynamic parameters for mass, stiffness and damping

Model Description	Mass [kg]	Stiffness [kN/m]	Damping [kNs/m]
2 DOF by Griffin (1990)	m_s=1, m_o = 8.7, m_1 = 66.3	k_s =120, k_1 =39.7	c_s = 3.23, c_1 = 1.36
2 DOF by Rakheja et al. (1994)	m_1 = 52.9, m_o = 22.1	k_1 = 27.95	c_1 = 0.5
3 DOF by Cho et al. (2001)	m_1 = 7.3, m_o = 67.7	k_1 = 41, k_2 = 74.3	c_1 = 0.32, c_2 = 2.81
3 DOF by Patten et al. (1998)	m_1 = 12.5, m_2 = 62.5	k_1 = 24, k_2 = 68	c_1 = 0.19, c_2 = 1.54
3 DOF by Rakheja et al. (1994) and Cho et al. (2001)	m_o = 22.06, m_1 = 8.82, m_2 = 44.1	k_1 = 23.3, k_2 = 14.73	c_1 = 0.36, c_2 = 0.15

The derived seat to head transmissibility versus frequency curves with three resonant frequencies occurring at 3.5 Hz, 5 Hz and approximately 6.3 Hz are shown in Fig. 6, and their mathematical relationship is described in [1].

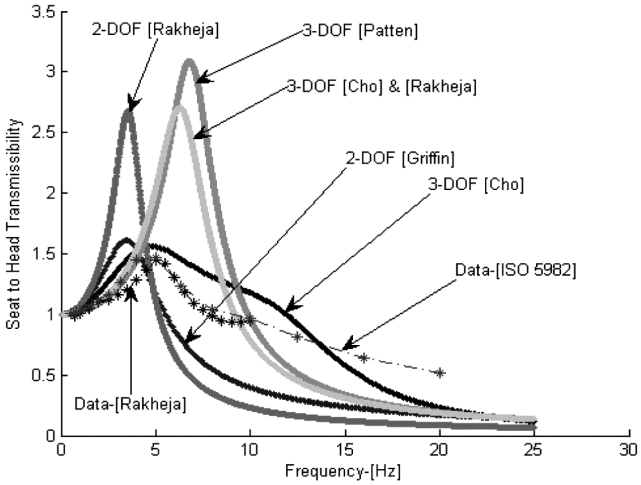

Fig. 6. Seat to head transmissibility as a function of frequency for the analyzed models

The 2-DOF curves have a common resonant frequency occurring at about 3.5 Hz, although there is considerable difference between the two peak seat to head transmissibility magnitudes due to the stiffness parameters. The 3-DOF by Patten, 3-DOF by Rakheja and Cho curves have similar seat to head transmissibility at 6.8 Hz and 6.3 Hz respectively that depict whole body resonant frequency. The 3-DOF by Cho and experimental curves from ISO Standard [5] have similar seat to head transmissibility response and a common peak resonant frequency occurring between 4–5 Hz. Published experimental data from ISO and Rakheja et al. have been used to simulate the seat to head ratio and mechanical impedance responses without the use of a backrest support.

Similarity of the peak seat to head transmissibility magnitude and resonant frequency in the 3-DOF by Patten, 3-DOF by Rakheja and Cho, and 2-DOF curves are influenced by the seat configuration and backrest support described in [3]. The 3-DOF by Patten whole body vibration frequency of 6.8 Hz derived from the seat to head transmissibility is slightly higher than the experimental results since the biodynamic model described in Fig. 4 includes only the head and neck region as a lumped mass supported by the seat backrest.

The 3-DOF by Rakheja and Cho curve is similar to the 3-DOF by Patten curve, although occurring at a lower peak magnitude, due to the mass of the head and chest regions approximated as a single lumped mass together with lower stiffness and damping parameters. The 3-DOF by Cho curve is able to approximate published experimental seat to head transmissibility data, since the model excludes the use of a backrest support. The inclusion of a backrest increases the natural frequency of the seated person when compared to a seat without a backrest from [3]. It can thus be seen that the 2-DOF and 3-DOF by Cho whole body frequencies are lower compared to the other models.

Mechanical impedance described by [4] is the ratio of the driving force acting on a system to the resulting velocity of the system measured at the same point and in the same direction as the applied force with units of [Ns/m]. A similar definition by [9] suggests the mechanical impedance is the force per unit velocity directed towards the person, which originated from the seat-person interface. The impedance response behavior is a "to the body" type transfer function, whereas the vibration transmissibility is construed as vibration transmission "through the body". The mechanical impedance curves expressed as a function of frequency are shown in Fig. 7.

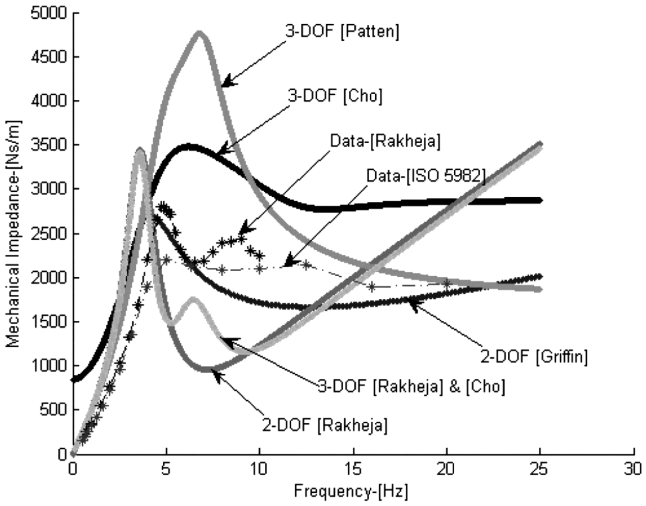

Fig. 7. Mechanical impedance curves as a function of frequency for the analyzed models

All mechanical impedance curves approximate the whole body resonant frequency occurring within the region of 4.5–6.8 Hz. The 3-DOF by Rakheja and Cho, 2-DOF by Rakheja and 3-DOF by Cho curves show similar peak impedance magnitudes, whereas the 3-DOF by Patten curve has a higher peak impedance magnitude. The 3-DOF by Rakheja and Cho curve highlights a second resonant frequency region, which are not replicated in other models, but supported with experimental data and associated with motion of the legs.

The 2-DOF by Rakheja and 3-DOF by Rakheja and Cho curves have similar impedance responses, which have a lower resonant frequency value, compared to the other curves. The similarity in the impedance response is due to the approximately equal mass distribution of the lower skeletal frame occurring at the seat-person interface. The high peak impedance and transmissibility magnitudes observed in the 3-DOF by Patten model are caused by the high stiffness parameters with similar findings supported by Smith [12]. Experimental data shown in Fig. 7 is closely approximated using a 4-DOF model that was described in [5] together with the 2-DOF by Griffin curve. The results indicate that the used biodynamic stiffness and damping parameters represent a compromise in accuracy towards achieving both mechanical impedance and seat to head transmissibility responses.

4. Conclusion

The five biodynamic models provide an easy method to determine peak seat to head transmissibility and mechanical impedance behaviors when compared to experimental results. As an initial design approximation to the seat suspension system, the 2-DOF models could be utilized to predict the discomfort level or peak transmissibility and impedance magnitude arising from the seat cushion-person interface and lower torso. The 3-DOF models can be used to investigate the transmissibility effects relating to the skeletal frame, whole body vibration and to reconfirm the discomfort level relating to the lower torso in addition to investigating the use of a backrest.

The reason why the 2-DOF models give results closest to the experimental data is due to the exclusion of the backrest support and absence of greater anatomical description related to the legs and feet. The 3-DOF model is sensitive to the backrest support and thus a higher resonant frequency is observed for whole body vibration. The effect of various backrest support positions and its influence on vibration transmissibility and whole body vibration is a subject of future research.

Acknowledgements

The authors would like to thank Dr Jan Pieter de Wilde for the review and suggestions made to this article.

The presented results of research realized in the framework of task No. M-4/353/2016/DS were a subsidy for research granted by the Ministry of Science and Higher Education of the Republic of Poland.

References

[1] Behari N., *Comparison of Dynamic Models of Humans Sitting on Seats*, Masters Thesis, University of Stellenbosch, December 2005.

[2] Bellmann M., *Perception of Whole-Body Vibrations: From basic experiments to effects of seat and steering-wheel vibrations on the passengers comfort inside vehicles*, Ph.D. Thesis, University of Oldenburg, 2002.

[3] Cho Y., Yoon Y.S., *Biomechanical model of human on seat with backrest for evaluating ride quality*, International Journal of Industrial Ergonomics, Vol. 27(5), 2001, 331–345.

[4] Griffin M.J., *Handbook of Human Vibration*, Academic Press, London 1990.

[5] ISO 5982:2001(E), Mechanical vibration and shock-Range of idealised values to characterize seated body biodynamic response under vertical vibration, International Organisation for Standardisation.

[6] Książek, M.A., *New ways of Modelling of Human Vibration Discomfort*, Internoise 99, Fort Lauderdale, 1999, 1–6.

[7] Kubo M., Terauchi F., Hiroyuki A., Matsuoka Y., *An investigation into a synthetic vibration model for humans: An investigation into a mechanical vibration human*

model constructed according to the relations between the physical, psychological and physiological reactions of humans exposed to vibration, International Journal of Industrial Ergonomics, Vol. 27(4), 2001, 219–232.

[8] Patten W., Pang J., *Validation of a Nonlinear Automotive Seat Cushion Vibration Model*, Vehicle System Dynamics: International Journal of Vehicle Mechanics and Mobility, Vol. 30(1), 1998, 55–68.

[9] Rakheja S., Wu X., Boileau P.E., *A body mass dependent mechanical impedance model for applications in vibration seat testing*, Journal of Sound and Vibration, Vol. 253(1), 2002, 243–264.

[10] Rakheja S., Afework Y., Sankar S., *An Analytical and Experimental Investigation of the Driver-Seat-Suspension System*, Vehicle System Dynamics: International Journal of Vehicle Mechanics and Mobility, Vol. 23(1), 1994, 501–524.

[11] Rosen J., Arcan M., *Modeling the Human Body/Seat System in a Vibration Environment*, Journal of Biomechanical Engineering, Vol. 125(2), 2003, 223–231.

[12] Smith S.D., *Nonlinear Resonance Behaviour in the Human Exposed to Whole-Body Vibration*, Shock and Vibration, Vol. 1(5), 1994, 439–450.

TECHNICAL TRANSACTIONS | CZASOPISMO TECHNICZNE
MECHANICS | MECHANIKA
5-M/2016

DOI: 10.4467/2353737XCT.16.282.6114

ARTUR GAWLIK, ANDRZEJ SOBCZYK, PAWEŁ WALCZAK*

HYDRAULIC HYBRID VEHICLE WITH ENERGY RECUPERATION

HYDRAULICZNY HYBRYDOWY POJAZD Z ODZYSKIEM ENERGII

Abstract

Modern transport vehicles and mobile machines have a high advanced functionality and quality of work. However, it is often associated with high power consumption. That is why research focused on reducing vehicle operating costs is so important. The possibilities of reduction of fuel consumption in combustion engines, which are usually the primary source of energy in many vehicles, seem to be exhausted. It came from design constraints of the combustion engine and increasingly stricter emission's standards. That is way very popular become energy recovery system. Usually, these systems are based on an electric storage battery. Energy is capturing during braking of the vehicle and transferred to the electric motor periodically connected with the drive system. While, in the vehicles driven by hydrostatic system hydraulic energy in a similar way can be captured and stored in the hydro-pneumatic accumulator. This paper presents such solution of energy saving system based on an additional pump and hydro-pneumatic accumulator build into vehicle hydrostatic drive system. Mechanical and hydraulic elements of vehicle drive system were modelled using SimulationX software. The standard drive system is comparing with the energy recuperation drive system. Tests have been conducted for assumed working cycle and several operating parameters by the use of SimulationX. Reached than 10% energy saving in one cycle, confirms the correctness of designed structure of the hydraulic energy recovery system.

Keywords: Energy Recuperation, Hydrostatic Drive, SimulationX

Streszczenie

Współczesne pojazdy transportowe i maszyny mobilne charakteryzują się wysoko zaawansowaną funkcjonalnością i jakością pracy. Jest to jednak często związane z dużym zużyciem energii. Zrozumiałe jest zatem prowadzenie prac ukierunkowanych na ograniczenie kosztów eksploatacyjnych. Możliwość znaczącego obniżenia zużycia paliwa przez silniki spalinowe, będące zazwyczaj źródłem pierwotnym energii w pojazdach użytkowych, wydaje się być wyczerpana. Wynika to zarówno z ograniczeń konstrukcyjnych silnika spalinowego, jak i zaostrzających się norm dotyczących czystości spalin. Stąd też zainteresowanie systemami odzysku energii wspomagającej jednostkę napędową przy zwiększonym obciążeniu. Zwykle są to układy bazujące na akumulatorach elektrycznych, w których jest gromadzona energia przechwytywana w procesie hamowania pojazdu i przekazywana następnie do silnika elektrycznego łączonego okresowo z układem napędowym, nazywane popularnie hybrydowymi układami napędowymi. W artykule opisano rozwiązanie i wyniki testów symulacyjnych systemu odzysku energii kinematycznej dla małego pojazdu transportowego z przekładnią hydrostatyczną. Układ napędowy pojazdu złożony z elementów mechanicznych i hydraulicznych zamodelowano z wykorzystaniem bibliotek programu SimulationX firmy ITI GmbH. W celu porównania energochłonności standardowego układu napędowego i układu wspomaganego przez system rekuperacji energii przeprowadzono testy symulacyjne dla przyjętego cyklu roboczego oraz dla kilku konfiguracji parametrów eksploatacyjnych. Osiągnięta ponad 10% oszczędność energii w cyklu testowym potwierdza słuszność założeń zaprojektowanej struktury proponowanego systemu odzysku energii.

Słowa kluczowe: odzysk energii, napęd hydrostatyczny, SimulationX

* Ph.D. Eng. Artur Gawlik, Prof. D.Sc. Ph.D. Eng. Andrzej Sobczyk, Ph.D. Eng. Paweł Walczak, Institute of Machine Design, Faculty of Machine Design, Cracow University of Technology.

1. Introduction

We hope that this template will make it easier to write the article. In heavy-duty machines characterizing by a quasi-repeatable working cycle is the possibility to recover the kinetic and potential energy [2, 3, 7, 9, 10]. In mobile machines and vehicles are usually systems based on electric accumulators, which store energy captured during vehicle braking and next transmit energy to the electric motor that is periodically connecting with the drive system [4]. Such systems are commonly called hybrid powertrains. The problematic elements of this type of system are an electric accumulator. Due to the limited speed of chemical changes cannot accumulate large portions of energy in a short time and also have a limited number of charge cycles. Whereas, in vehicles with hydrostatic transmission can be used to capture and storage of energy hydro-pneumatic accumulator in a similar way as the electric accumulator [1].

2. The simulation model

The article describes the design and test results of simulation of kinetic energy recovery system for a small transport vehicle with hydrostatic transmission. Vehicle drive system composed of mechanical and hydraulic modelled using SimulationX ITI software.

Tests were conducted for assumed duty cycle and for several configurations of operating parameters to compare the energy consumption of the standard powertrain with a hydrostatic transmission system and powertrain aided by energy recuperation system simulation. In the mathematical model were made following assumptions:

- the wheeled vehicle is traveling on a flat, solid ground.
- no slip between the wheels and the ground,
- constant thermal conditions, the temperature of hydraulic oil changes much slower than changes in pressure,
- dynamics valves are omitted; response time is significantly shorter than time reaction of traveling mechanism.

The proposed solution of the secondary energy source in the form of a hydro-pneumatic accumulator such as Permo Drive system [8] used in trucks. In this system, a reversible hydraulic unit is mounted on the drive shaft of the vehicle, and the energy of the braking phase is stored in the hydro – pneumatic accumulators. The stored energy is redistributed to the reversible unit supporting the drive system during the acceleration phase of the vehicle. This solution is used as a support system for the classic drive system of the heavy transport vehicle [5, 6].

In order to reduce the cost of the components of the proposed system and the possibility of applying different control strategies already at the design stage, the recovery system combined with a mechanism for driving through a belt drive with toothed belt (9), controlled coupling (8) and additional pump (5) (Fig. 1). Installation of elements of the presented energy recuperation system (rectangular block – dashed line) does not require significant modifications of the standard hydrostatic transmission and does not change its basic functionality. The weight of additional elements depending on the final configuration and will be oscillated near several dozen kilos so that it will be had not an affect significantly on the capacity of tested transport vehicle. Complete vehicle kerb weight is 1000 kg.

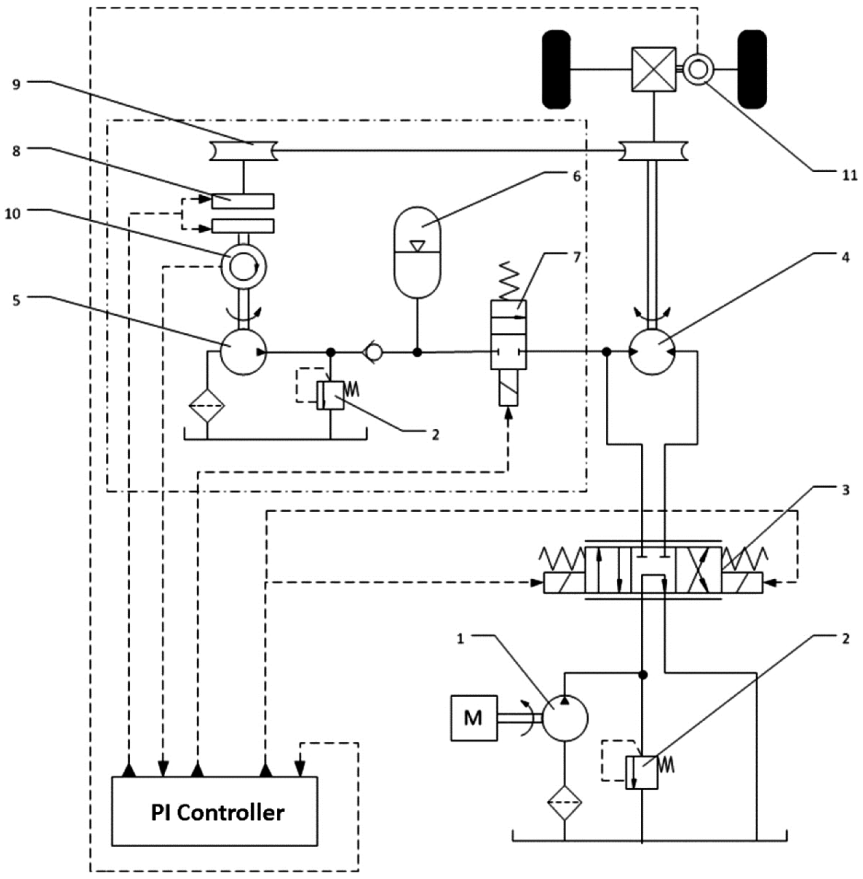

Fig. 1. Schema of hybrid (mechanical – hydraulic) hydrostatic drive system with Energy recuperation where: 1 – main pump, 2 – relief valve, 3 – 4/3 proportional directional valve, 4 – hydrostatic motor, 5 – additional pump, 6 – hydro – pneumatic accumulator, 7 – 2/2 directional valve, 8 – clutch, 9 – teeth belt transmission, 10,11 – rpm transducers

The controller based on signals from velocity sensors of additional pump shaft (5) and the vehicle drive axle generates control signals for proportional directional control valve (3), 2/2 valve on/off type (7) and switching actuator of disc clutch (8). The PI controller used in the controller provides repeatable vehicle traction parameters that are necessary for correct comparison the operating parameters of conventional and recuperation energy system. Working cycle selected for simulation tests consists of two vehicle speed test runs with a five – second acceleration phase, a thirty – five – second phase of constant travelling speed and the three – second deceleration phase. The simulation was carried out for three target speeds of the vehicle, i.e. 10, 15 and 25 km/h and in the consequence for three distances covered from 200 to 500 m. During testing of the system with energy recovery, the hydro – pneumatic accumulator was pre – charged to about 50% of the nominal volume and was not used in the first phase of acceleration of the vehicle. Next, in both periods of deceleration of

the vehicle, accumulator was charged. The additional pump was driven until the speed of the drive shaft in this unit does not decrease below 600 rpm (by reason of the low efficiency of the pump at a lower speed). Table 1 shows the data, taken for simulation and operating parameters shown at the graphs.

Table 1

Summary of key physical quantities adopted for the simulation and determined system parameters

Quantity	Symbol	Value/Unit
Complete vehicle kerb weight	m	1000÷2000 [kg]
the vehicle set speed	v	10÷25 [km/h]
belt transmission ratio	i	3
relief valve opening pressure	p_o	18 [MPa]
hydro-pneumatic accumulator nominal volume	V_{acc}	5÷40 [dm^3]
hydro-pneumatic accumulator pre-fill pressure	p_{acc}	3.5 [MPa]
main pump displacement volume	q_1	18 [cm^3/rev]
auxiliary pump displacement volume	q_2	30÷40 [cm^3/rev]
the hydraulic motor displacement volume	q_s	100 [cm^3/rev]
combustion engine power at 2000 rpm	N_s	24 [kW]
main pump outlet pressure	p_{p1}	[MPa]
auxiliary pump outlet pressure	p_{p2}	[MPa]
hydraulic motor inlet pressure	p_s	[MPa]
travelled distance	L	[m]
combustion engine power in classic system	N_s	[kW]
combustion engine power in system with energy recover	N_{acc}	[kW]

3. Simulation result

Fig. 2 shows selected working parameters of hydrostatic transmission with energy recuperation system.

In 50 and 120 seconds, the moment of the switching of the auxiliary pump during braking phase (pressure p_{p2} increased) is visible. The operation time of this unit is very short, so the hydro – pneumatic accumulator is loaded in 2 seconds cycles, which forced the pre – selection of the size of the additional pump. The pump displacement volume is 40 m^3/rev.

Hydro-pneumatic accumulator model used in the simulation takes into consideration the thermodynamic losses. This effect is visible on the graph of hydro – pneumatic accumulator pressure p_{acc}. This pressure gradually decreases when the accumulator is not using and in this way reducing the efficiency of the proposed system. During vehicle acceleration in the second cycle, the system using the power from the hydro-pneumatic accumulator and that's way input pressure of the hydraulic motor is higher than it was in the first cycle. The possibility of usage of the secondary power source is controlled by on/off valve (7) (Fig. 1). The main directional control valve, controlled by the PI controller, reduces the volumetric

flow rate in the drain line of hydraulic motor to avoid exceeding acceleration limits of the vehicle.

Fig. 3 presents a comparison of the power of combustion engine in conventional drive system N_s and drive with energy recovery system N_{acc}. To estimate energy requirement in the compared systems always was chosen the same simulation time interval, i.e., the second cycle. The difference in areas under the graphs of power illustrates energy recovery in percentage.

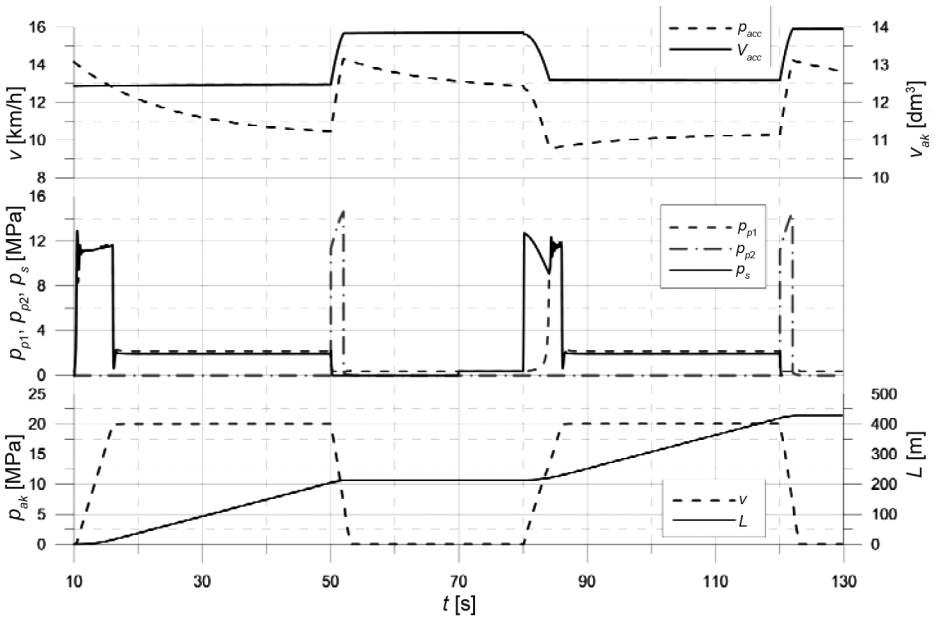

Fig. 2. Exemplary of hydrostatic transmission working parameters with energy recuperation, for 1500 kg vehicle weight riding with velocity 20 km/h

In Fig. 4 the energy yield of the drive system, depending on the set speed of the vehicle for one exemplary configuration of components that store the kinetic energy during the braking phase. The efficiency of the proposed system is decreasing with increasing of vehicle speed. It is the result of increasing the input pressure of the hydraulic motor in the acceleration phase, which significantly limits the possibility of using the stored energy at a lower pressure in the hydro-pneumatic accumulator. Assumptions of the operating cycle are unchangeable, so the vehicle accelerates to the set speed at the same time i.e. 5 s.

Vehicle drive system with a total weight 1000 kg, speed 15 km/h, has a distinctly low value of energy recuperation. It comes from the relatively low inertia of the vehicle and the need to supplement the flow rate by the main pump to keep the required delay resulting from the assumed cycle with simultaneous loading hydro-pneumatic accumulator.

The selection of elements of energy recovery system has a significant impact on the value of the expected energy savings. Required parameters of these components depend strongly on the assumed cycle of load and traction settings. Fig. 5 is a 3D graph, which shows that

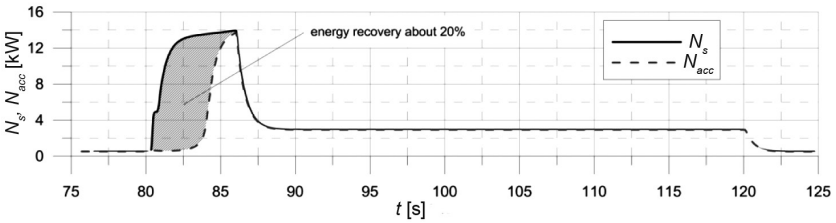

Fig. 3. Comparisons of the power of combustion engine in classic system and in system with energy recover for a vehicle with a total weight 1500 kg and a speed 20 km/h

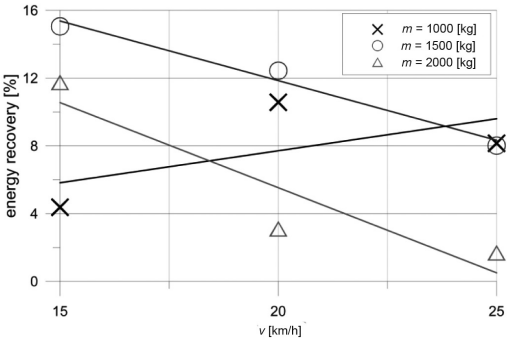

Fig. 4. Values of energy recovery as a function of vehicle speed for different masses of the total for the nominal volume of the hydro-pneumatic accumulator equal 20 dm^3 and displacement of auxiliary pump equal 40 cm^3/rev

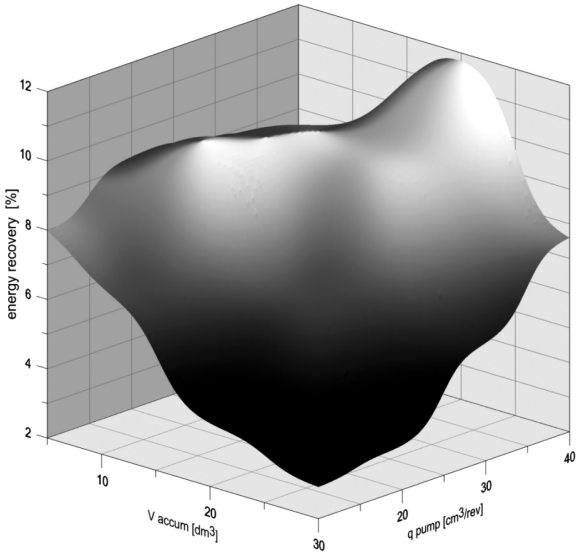

Fig. 5. Energy recuperation as a function of hydro-pneumatic accumulator size and pump displacement for vehicle total mass 1500 kg driving with velocity 25 km/h

for the vehicle with total weight 1500 kg and phase of constant travelling speed of 25 km/h, the most beneficial system of energy recovery from the point of view of efficiency requires pump of displacement volume 40 cm^3/rev and hydro-pneumatic accumulator with a nominal volume of 20 dm^3. Presentation in a similar way other parameters of the proposed system allows to select the best possible configuration.

4. Summary

During simulation was reached more than 10% energy saving in the test cycle. It confirms the validity of the assumptions of designed structure of the proposed energy recovery system. The percentage energy saving is strongly dependent on the working cycle of the vehicle. Long periods of standing and running with constant speed reduce the efficiency of the energy recovery system with hydro-pneumatic accumulator. The energy losses are result of thermal transmittance of accumulator shell. In vehicles with combustion engines these losses can be reduced by directing hot gases from the exhaust system on the accumulator shell.

Another way to use the proposed energy recuperation system is to work the system in the strategy of temporary increase the power of hydrostatic transmission. The oil pressure in the hydro-pneumatic accumulator can be set above the opening pressure of the relief valve in the main hydraulic system. It allows for a temporary increase of acceleration of the vehicle in the initial phase or helps during star motion of overloaded vehicle.

Weight of additional elements depending on the configuration and will not significantly influenced on complete vehicle kerb weight (max. to 5%). The cost of energy recovery system should be about 1 000 Euro. It represents about 10% of price increase of a new vehicle.

Analysis of simulation results indicate that one of the ways to maximize energy savings in the drive system of the vehicle is the selection of components of subsystem energy recuperation to the most common working cycle. Further work will give attention to improving control strategy, so that system could be more universal. Also road tests will be carried out on the modified transport vehicle, where the electric drive system was replaced by a hydrostatic transmission.

References

[1] Chojnacki M., Sobczyk A., Walczak P., *Symulacja możliwości odzysku energii w układzie hydraulicznym koparki*, Inżynieria Maszyn, No. 2, 2014, 28–37.

[2] Gawlik A., *Energy Recovery System for Excavators With Movable Counterweight*, 39th International Scientific Congress on Powertrain and Transport Means, No. 2, Jurata 2013, 113–120.

[3] Gawlik A., Sobczyk A., Walczak P., *System odzysku energii w pojazdach z napędem hydrostatycznym*, Transport Przemysłowy i Maszyny Robocze, No. 2 (24), 2014, 47–50.

[4] Kucybała P., Pobędza J., *Energy Recuperation in Hydrostatic Transmission System*, Hydraulika i Pneumatyka, No. 6, 2008, 31–33.

[5] Lin C-C., Wu B., Filipi Z., Peng H., Assanis D., *Optimal Power Management for a Hydraulic Hybrid Delivery Truck and Wheel Loaders*, Journal of Vehicle System Dynamics, vol. 42, 2004, 23–40.
[6] Liang X., Virvalo T., *Energy Reutilization and Balance Analysis in a Hydraulic Crane*, Iha, Tampere University of Technology, 2003.
[7] Sobczyk A., *Improvement of Hydraulic System Efficiency by Means of Energy Recuperation,* Cracow University of Technology Press, Krakow 2011.
[8] Stecki J., Matheson P., *Advances in Automotive Hydraulic Hybrid Drives*, Proc. of the 6th International Conference on Fluid Power Transmission and Control, China, Hangzhou 2005.
[9] Śliwiński P., *The basics of design and experimental tests of the commutation unit of a hydraulic satellite motor*, Archives of Civil and Mechanical Engineering, nr 16/2016. DOI: 10.1016/j.acme.2016.04.03.
[10] Kędzia K., *Wyznacznik zmienności cyklu obciążenia wielośródłowego hydrostatycznego układu napędowego*, Oficyna Wydawnicza Politechniki Wrocławskiej, Wrocław 2014.

TECHNICAL TRANSACTIONS | CZASOPISMO TECHNICZNE
MECHANICS | MECHANIKA
5-M/2016

DOI: 10.4467/2353737XCT.16.283.6115

MARIA HEBDOWSKA-KRUPA, MICHAŁ ŁACH, JANUSZ MIKUŁA*

VOLCANIC TUFF AS AN INHIBITOR OF CORROSION IN AQUEOUS ENVIRONMENT

TUF WULKANICZNY JAKO INHIBITOR KOROZJI W ŚRODOWISKU WODNYM

Abstract

The aim of the studies was to examine the applicability of volcanic tuff as a corrosion inhibitor in aqueous systems and to identify the mechanisms owing to which the tuff is acting as an inhibitor of corrosion. The scope of research includes: examinations of the structure and selected properties of the tuff from Filipowice, including fractographic examination of the Filipowice tuff rocks, X-ray diffraction analysis, and thermal analysis; study of the corrosion resistance of DC01A low-carbon steel in aqueous systems without and with inhibitor, which is volcanic tuff.

Keywords: corrosion, inhibitors, volcanic tuff

Streszczenie

Celem badań było określenie możliwości zastosowania wulkanicznego tufu jako inhibitora korozji w środowiskach wodnych oraz określenie mechanizmów, które powodują, że tuf wulkaniczny działa jako inhibitor korozji. Zakres badań obejmuje: badania struktury i wybranych właściwości tufu z Filipowic, w tym faktograficzne badania tufu w postaci skał, analizy dyfrakcji rentgenowskiej i analizy termicznej; badanie odporności na korozję DC01A stali niskowęglowej w środowiskach wodnych bez oraz z inhibitorem, którym jest tuf wulkaniczny.

Słowa kluczowe: korozja, inhibitory, tuf wulkaniczny

* Ph.D. Eng. Maria Hebdowska-Krupa, Ph.D. Eng. Michał Łach, D.Sc. Ph.D. Eng. Janusz Mikuła, Institute of Materials Science, Faculty of Mechanical Engineering, Cracow University of Technology.

1. Introduction

Inhibitors are commonly used in the anticorrosion technology as agents reducing the rate of corrosion in metals and their alloys. Corrosion inhibitors can be divided into different groups, depending on the type of environment, the mechanism of action, the type of film (protective barrier) formed on the metal surface, and the type of material used in the inhibitor (organic, inorganic).

In terms of the type of environment in which they operate, the inhibitors can be divided into inhibitors active in aqueous solutions, in the air, and in organic liquids. The first and the largest group of inhibitors includes the inhibitors active in natural and industrial waters, and in solutions of salts, acids and bases [1].

In terms of the mechanism of the electrochemical action of inhibitors forming protective barriers on the metal surface, the inhibitors can be divided into the following types [2]:

– cathodic inhibitors – inhibit the cathodic process of depolarization,
– anodic inhibitors – inhibit the anodic process of metal dissolution,
– mixed inhibitors – affect both electrode processes, and are mainly adsorption inhibitors.

In terms of the nature of the protective barrier formed on the metal surface, adsorption inhibitors can be subdivided into inhibitors entering into reaction with metals by forces: chemical (chemisorption) or physical (physical adsorption) – due to the weak interaction, the latter type is not used in practice.

Corrosion inhibitors mainly operate through a mechanism called the anode passivation, although in their operation there are also other elements involved. As a result of an electrochemical process, inhibitors in the water with protecting liquid are guided to the anode and cathode, and are chemically absorbed on the surface. The resulting layer forms a barrier that effectively isolates the anode from the water in circulation and from contact with the cathode. This slows down the corrosion rate to a low level, usually about 100 or 1000 times lower than the corrosion rate in water without protecting liquid [3].

The passive layer undergoes continuous breaking and reconstruction and its presence depends on the continuous presence of the inhibitor in water, as its task is that of constant repair of the passive layer. With the lack of inhibitor, the protection against corrosion becomes immediately ineffective.

The value of pH – acidic or basic reaction of installation water – also plays a significant role in the corrosion of metals. For example, iron and steel corrode rapidly in an acidic environment, but not under alkaline conditions. The corrosion rate is affected by the type of corrosion product formed under various pH conditions. In an alkaline environment, iron and steel corrode to form Fe_3O_4 magnetite, which acts as a semi-protective layer on the metal surface reducing the rate of corrosion.

1. Silicates – inhibitors of cathodic-anodic type

Silicates have the general formula $\mathbf{Me_2OxSiO_2}$, where x is the molar silica-to-alkaline oxygen ratio. Sodium silicate solutions with a high modulus (high ratio of SiO_2 to Na_2O) contain the following particles [1]:

1) ions of Na^+, OH^-, SiO_3^{2-}, $n(Si_2O_5^{2-})$, $HSiO_3^-$
2) particles of Na_2SiO_3, $Na_2Si_2O_5$, H_2SiO_3, SiO_2nNaOH

3) complex compounds of $(SiO_3)x$, $(H_2SiO_3)x(SiO_2)x$, $(SiO_2)x$, $[(mSiO_3nSiO_2xH_2O)^m]^{2-}$ $(SiO_2xnH_2OySiO_3)$ and other compounds.

Silicates are cheap and popular inhibitors used primarily for the protection of water systems. The corrosion rate in the presence of silicate inhibitors is, however, higher than in the case of chromates [4]. On the other hand, silicates are not toxic in the concentrations normally used, do not confer to water taste, color or odor, eliminate the formation of "red water" and can be applied to systems already partially corroded. Like polyphosphates, silicates reduce the rate of corrosion not only in iron and its alloys, but also in other metals such as Al, Cu, Pb and Zn, in their respective alloys and bimetallic systems [5–7]. Silica concentration required to inhibit corrosion varies within wide limits depending on the type of metal and the composition of water, e.g.:

– crystalline silica – inhibits soft steel corrosion in a variety of cooling water types,
– sodium silicate – reduces the rate of corrosion in tap water by 82% [4],
– the ability of sodium silicate to move the corrosion potential in the negative and positive side, depending on the concentration, indicates that this inhibitor affects both the cathodic and anodic process; silicates added to the solution at higher concentrations result in inhibition of the anodic process, which means that the inhibitor may reduce the rate of the cathodic reaction of oxygen reduction and the anodic reaction of iron dissolution. So it is an inhibitor acting on both the anodic and cathodic process,
– due to their alkaline reaction in aqueous solutions, the effect of silicates does not mainly consist in the neutralization of CO_2 dissolved in water, but in spite of this, the adjustment of the solution pH using silicates provides a much better protection against corrosion than when the same pH value is obtained with the addition of a base alone, such as NaOH.

There is a general belief that silicates inhibit metal corrosion due to the formation of a protective layer on the surface of metals. There are two hypotheses regarding the formation of this layer in the presence of silicate:

– **First** – assumes a chemical reaction taking place between the metal ions or metal corrosion products and negatively charged ions of the silicate or colloidal silica particles, as a result of which iron silicates are formed [8, 9]. The role of silicates would thus consist in creating a protective layer on partially corroded iron, and so on iron on the surface of which there are iron oxides and hydroxides. The most widely accepted is the opinion that positively charged iron hydroxide removes water from negatively charged colloidal silica to deposit a protective film composed of both these substances.
– **Second** – assumes a neutralization of the oppositely charged particles of corrosion products and negatively charged silicate hydrolysis products. These particles undergo coagulation and a protective gel-like layer form on the metal surface [10] – according to this hypothesis, the mechanism of the protective film formation is not associated with the formation of iron silicates.

On a clean surface of iron or steel, silica in water is not deposited [11]. A necessary condition for the formation of a protective film is the presence of iron oxides and hydroxides on the surface, and therefore to make it possible for the silica to act as an inhibitor, the metal must first undergo corrosion. Therefore, the inhibitory effect of silica is often observed after the lapse of several days from the time of the first contact between the steel and the solution

[12, 19]. The mechanism of the action of silicate inhibitors in water is a very complex one and has not yet been clearly explained. It is generally believed that this mechanism is associated with the formation of thin film on the surface of metal. The protective properties of the film depend on the nature of corrosion products present on the surface of metal. The products of corrosion, which are hydrated oxides, capture from the solution the negatively charged particles of hydrated silica sol. As a result of this process, the initial film of a gelatinous structure is formed, and on its surface, a portion of the mechanical suspension present in water may be adsorbed. In this case, since both water and the film have an alkaline pH, iron and components responsible for the water hardness are deposited on the film. The composition of the protective layer can change, but nevertheless, it will always contain variable amounts of silica. Its structure is close to a silica gel, which means that in a wet state it is semi-permeable, while in dry state it forms a thin film, usually of a brownish color or resembling graphite in appearance. The formation of protective film inhibits corrosion and at the same time reduces further growth of the film. In this way, the thickness of the film is self-regulated and is typically about 0.002 mm. The film is regenerated automatically in the event of a partial removal or damage. Metal undergoes corrosion, and in this place, a fresh film is formed, provided silicates in an appropriate concentration are present in the water. In terms of the physico-chemical phenomena, the mechanism of the film formation is complex – besides the effect of absorption, other mechanisms are operating like chemisorption, ion exchange and coagulation of the sol [13].

The time of formation of the protective film is relatively long, and depending on the concentration of silicate in water, it ranges from several days to several weeks. The protective effect is achieved only after some time.

2. Purpose and scope of research

The aim of the studies was to examine the applicability of **volcanic tuff** as a corrosion inhibitor in aqueous systems and to identify the mechanisms owing to which the tuff is acting as an inhibitor of corrosion.

The scope of research includes:

- examinations of the structure and selected properties of the tuff from Filipowice, including fractographic examination of the Filipowice tuff rocks, X-ray diffraction analysis, and thermal analysis,
- study of the corrosion resistance of DC01A low-carbon steel in aqueous systems without and with inhibitor, which is volcanic tuff.

3. Volcanic tuff – composition and properties

Volcanic tuff is porous rock belonging to the family of clastic rocks, which consist of pyroclastic material, often with admixture of other clastic materials, cemented with e.g. silica or clay binder. The characteristic feature of tuff is high porosity and the associated low specific gravity.

Tuff may be of crystaloclastic, lithoclastic or vitroclastic character. Crystaloclastic tuff is mainly composed of single pyrogenic minerals, like quartz, sanidine, biotite. Lithoclastic tuff is composed of effusive rock fragments of different sizes. Vitroclastic tuff consists entirely of glass. The most common is mixed crystalo – litho – vitroclastic tuff [14].

The Permian tuff from Filipowice characterized by a crystalo – litho – vitroclastic properties also contains impurities, i.e. fragments of sedimentary rocks mainly limestone. It occurs in the vicinity of Krzeszowice, among others, in Filipowice wherefrom its name derives. It is a pink-colored rock with bright spots, highly porous, with characteristic randomly arranged automorphic crystals of biotite. The fresh tuff is soft, when dry, it becomes hard and very brittle. It is easy to process and highly valued as a building material resistant to atmospheric conditions.

The tuff in the Sudeten Mountains has a composition similar to the tuff from Filipowice (it occurs frequently in the Rotliegend formations). Dark-colored basalt tuff occurs near Wałbrzych, Nowa Ruda and in Lower Silesia.

The tuff from Filipowice includes the following components: sanidine (the predominant component– Fig. 1, 2), kaolinite, biotite, illite, quartz, heavily modified feldspar, crushed alien rocks, opaque minerals, microcrystalline binder and carbonate binder.

Table 1

Composition of oxides in a sample of tuff from Filipowice used in the present studies

SiO_2	Fe_2O_3	Al_2O_3	CaO	MgO	TiO_2	K_2O	Na_2O	Other
56.04%	5.38%	16.73%	5.39%	0.60%	0.85%	9.16%	0.39%	5.46%

Fractography and EDS analysis of the Filipowice tuff rock

Structural and fractographic studies of the Filipowice tuff rock fragments were performed on a JSM-5510LV scanning electron microscope (made by Jeol Company) with (EDS) X-ray microanalyser. Quantitative analysis of the elemental composition was also conducted.

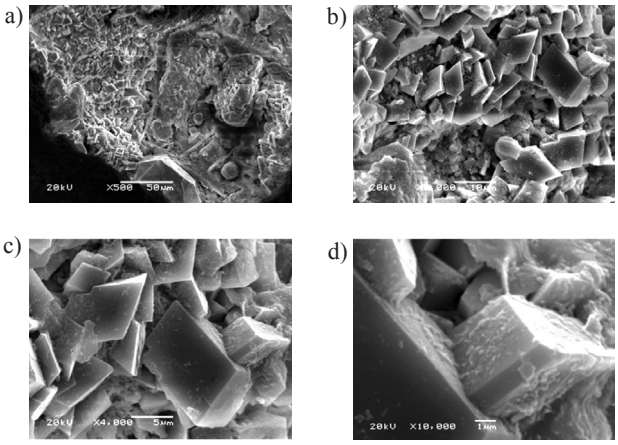

Fig. 1. Porous structure of Filipowice tuff – rhombohedral crystals of potassium feldspar:
a) – 500 x, b) – 2 000 x, c) – 4 000 x, d) –10 000 x

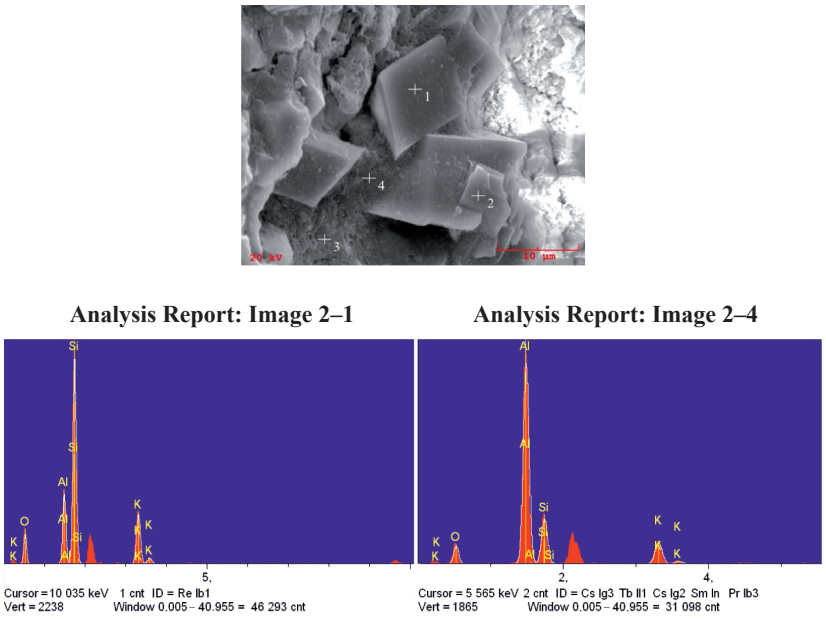

Fig. 2. Crystals of potassium feldspar embedded in a microcrystalline binder – EDS analysis

Studies by SEM and (EDS) X-ray microanalysis have shown that, besides sanidine, the tuff from Filipowice also contains quartz, kaolinite, illite, biotite and possibly allophane.

X-ray diffraction analysis

Phases present in the tuff were examined with X-PERT Philips PW 1830 X-ray diffractometer using tube with the following operating parameters: voltage = 40 kV, current = 30 mA.

The test product was pulverized natural tuff.

The X-ray diffraction analysis of tuff from Filipowice in natural condition revealed the occurrence of two main phases (Fig. 3):

- potassium aluminosilicate $K(AlSi_3O_8)$,
- silica SiO_2.

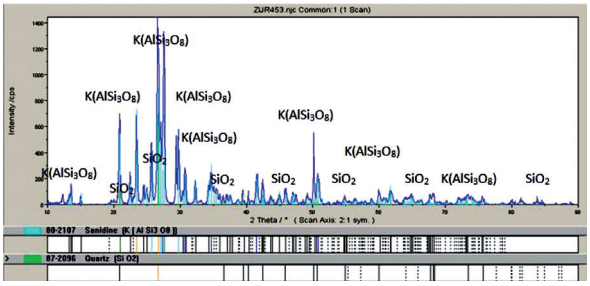

Fig. 3. The diffraction pattern of natural tuff powder

Thermal analysis

Thermal activation of aluminosilicates, conducted at low and high temperatures, leads to significant changes in both structure and texture. The increased temperature leads to dehydration, dehydroxylation and crystallization of new phases. For example, minerals from the kaolinite group, depending on their mineralogical nature and heating time, undergo dehydroxylation in the temperature range of 500–900°C. Consequently, kaolinite is formed, the structure of which is composed of disturbed tetrahedral layer and deformed aluminum octahedra [15].

The differential thermal analysis (DTA) and thermogravimetric studies (TG) were performed. The analysis was carried out using a NETZSCH STA 409 CD QMS 403/5 Skimmer mass spectrometer (Fig. 4–6).

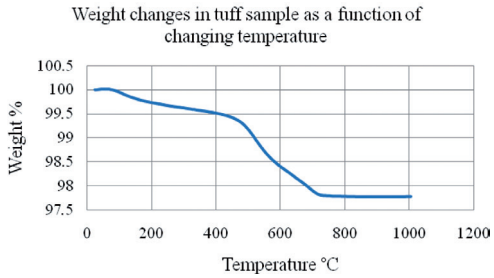

Fig. 4. The results of thermogravimetric studies

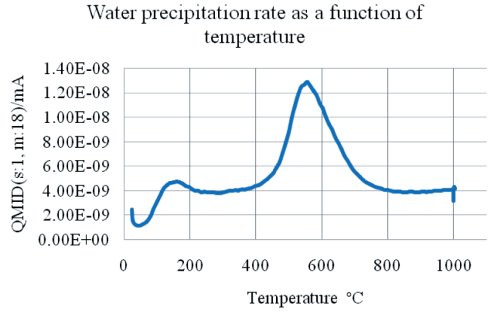

Fig. 5. The rate of water precipitation as a function of temperature

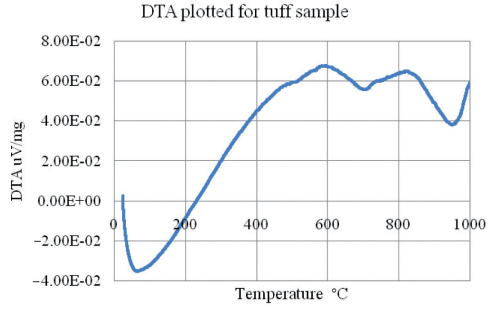

Fig. 6. Thermal effects accompanying transformations taking place in tuff under the effect of temperature

As shown by the thermographic analysis, biggest changes in the weight of natural tuff (powder) occur at a temperature of 702°C, and the weight loss is 2.3%. Water precipitates from the sample at temperatures ranging from 100 to about 820°C and the maximum precipitation rate occurs at about 550°C. It is a well-known fact [16–18] that in the process of thermal treatment, water is gradually removed from the aluminosilicate. In the temperature range from 105°C to 130°C, hydroscopic water is removed, at temperatures ranging from 180°C to about 500°C – water of crystallization, and at a temperature higher than 350°C – zeolitic water. In the case of tuff from Filipowice, the zeolitic water was removed in a temperature range of up to 820°C.

The differential thermal analysis has shown that phase transformations occur in the sample during heating at 468°C, 594°C and 818.7°C (exothermic transformations) and at 702°C and 949.3°C (endothermic transformations).

4. Testing the steel corrosion resistance in an environment of water and in 3% NaCl solution

The aim of the studies was to observe the behavior of DC01 low-carbon structural steel in accordance with PN-EN ISO 1514:2005 in aqueous systems with and without the addition of thermally activated volcanic tuff. The tuff was crushed and milled to an average particle size of 40. Thermal activation of Filipowice tuff was conducted at 850°C for 4h. Laboratory tests in liquids and solutions were carried out by the gravimetric method at ambient temperature. Tests were performed in the following media:

- water,
- 3% NaCl solution,
- water with 7 g of tuff per 1 dm^3 of solution at 20°C,
- 3% NaCl solution with 7 g of tuff per 1 dm^3 of solution at 20°C.

Studies were carried out on standard samples with dimensions of 50 × 40 × 0.8 mm, which, before the tests, were degreased with carbon tetrachloride, and then were placed in a measuring vessel with respective solution. Samples were placed in the vessels with solution in a hanging position. Measurements were going on for 60 days.

The samples, after removal from the solution and the subsequent washing and drying, were weighed and their surface was examined by SEM and EDS X-ray analysis. For comparison, the same examinations were also carried out on samples prior to immersing them in the solution.

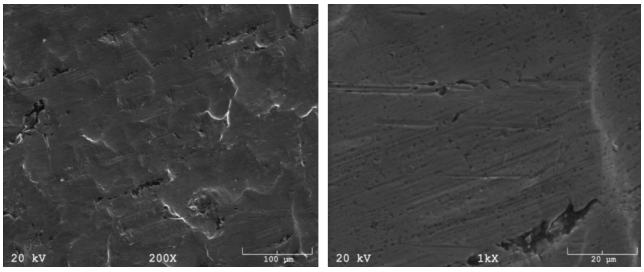

Fig. 7. Steel sheet surface before immersing in the solution

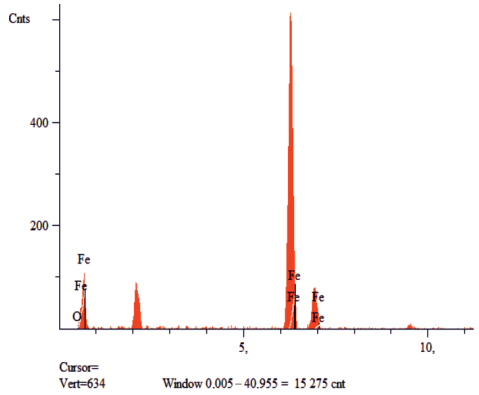

Fig. 8. EDS analysis conducted on sample before immersing in the solution

The EDS analysis (Fig. 8) has shown that the sample, which was not immersed in the solution, contained only iron, manganese and oxygen. The oxygen content ranged from 1.1 to 2.2%.

The results of corrosion tests in an aqueous environment

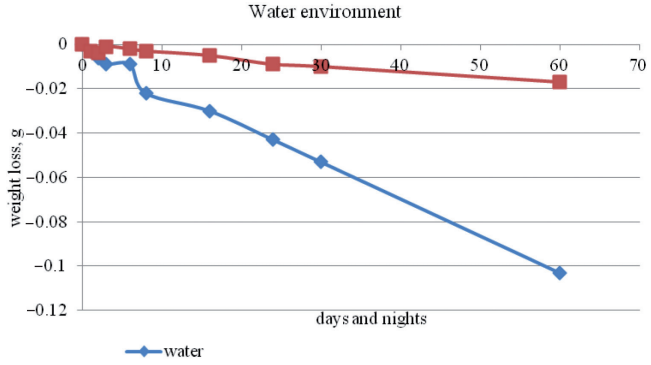

Fig. 9. The weight loss of samples in water – series 1 and in water with the addition of tuff – series 2

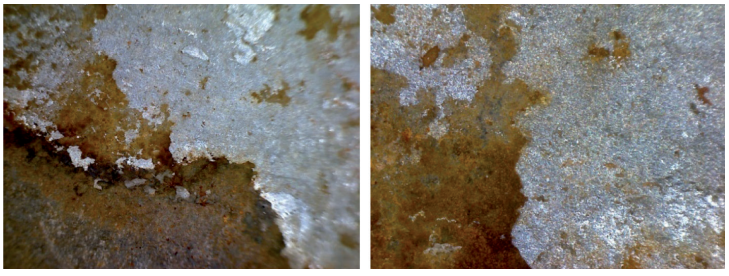

Fig. 10. Steel sheet surface after 60 days of exposure to water environment (40x and 200x)

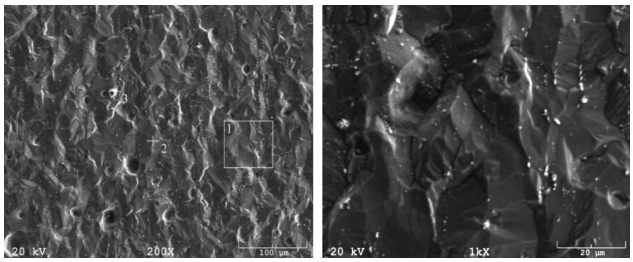

Fig. 11. Steel sheet surface after 60 days of exposure to water environment – sample taken out from water and washed

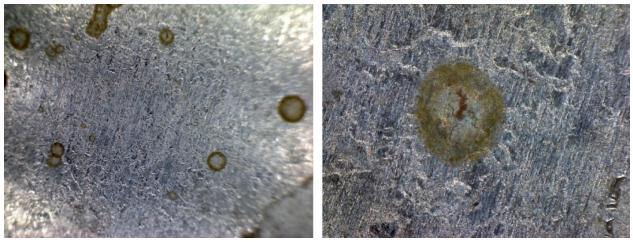

Fig. 12. Steel sheet surface after 60 days of exposure to water + tuff environment – sample taken out from water (40x and 200x)

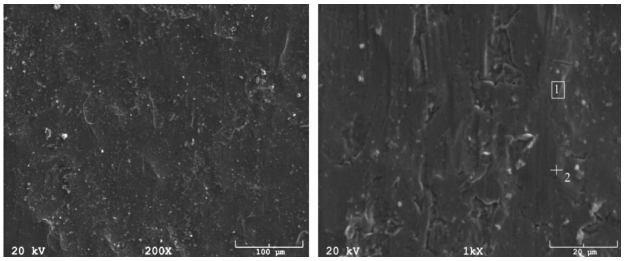

Fig. 13. Steel sheet surface after 60 days of exposure to water + tuff environment

The results of corrosion tests in a seawater environment

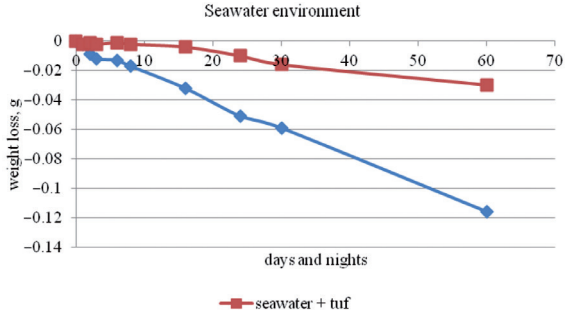

Fig. 14. The weight loss of samples in seawater – series 1 and in seawater with the addition of tuff – series 2

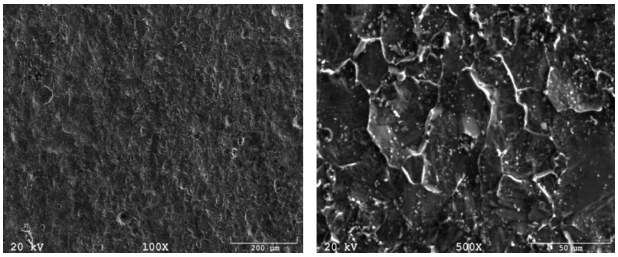

Fig. 15. Steel sheet surface after 60 days of exposure to the effect of 3% NaCl solution – sample taken out from the solution and washed

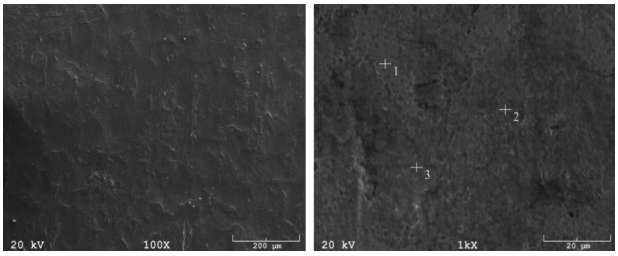

Fig. 16. Steel sheet surface after 60 days of exposure to the effect of 3% NaCl solution+ tuff – sample taken out from the solution

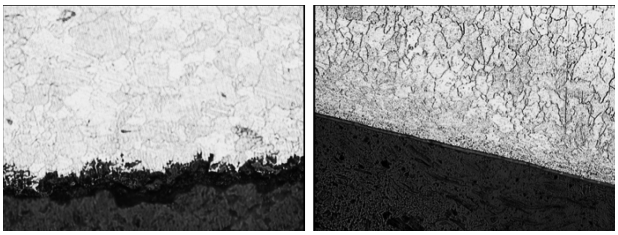

Fig. 17. Steel sheet immersed in 3% NaCl solution with the addition of tuff, the exposure period – 60 days; transverse metallographic section, 100x, specimens etched with 4%HNO_3

In water with the addition of tuff (Fig. 9–13), samples of low-carbon steel showed an average weight loss six times lower than the samples placed in water without tuff. In 3% NaCl solution with the addition of tuff (Fig. 14–17), samples showed an average weight loss four times lower than the samples placed in seawater without tuff.

As a result of tuff addition to water and 3% NaCl solution where samples of the low-carbon structural steel were placed, the appearance of the samples changed as well as the depth of corrosion layer from the developed with deep pitting to a flat silver-colored surface with visible coating of protective layer. Examinations made on transverse metallographic sections of these samples revealed the presence of a protective layer. On the metal surface exposed to the effect of water with the addition of tuff and to the 3% NaCl solution, minor signs of corrosion were observed. Examinations carried out under a stereoscopic microscope showed that this was due to microcracks formed in the protective layer.

Surface examinations by SEM and EDS X-ray microanalysis

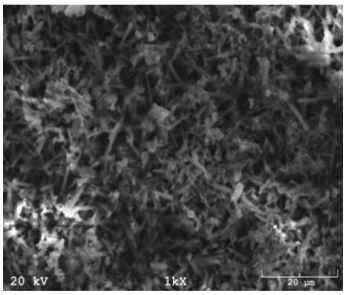

Fig. 18. A layer of film deposited on the steel sheet surface after 60 days of exposure to water environment

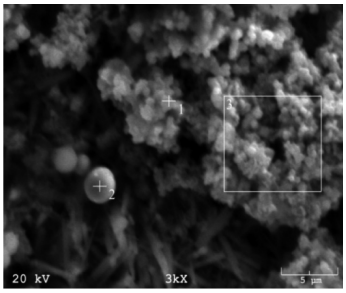

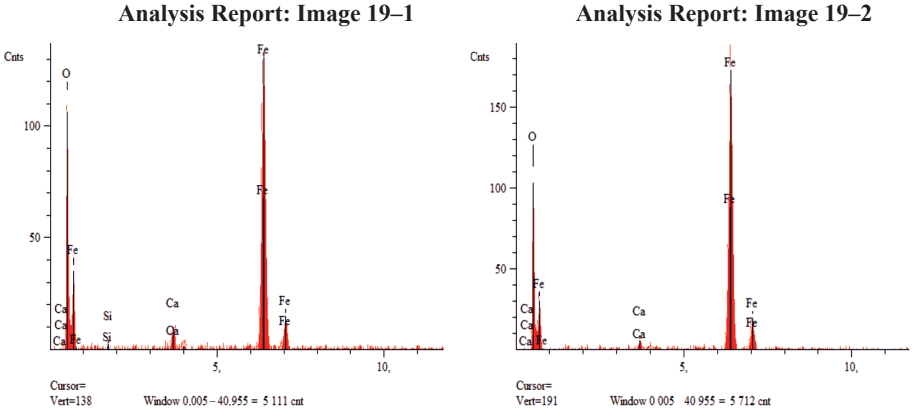

Fig. 19. A layer of film deposited on the steel sheet surface after 60 days of exposure to water environment – EDS analysis

Figures 18 and 19 show a layer of film deposited on the steel sheet surface after 60 days of exposure to water environment.

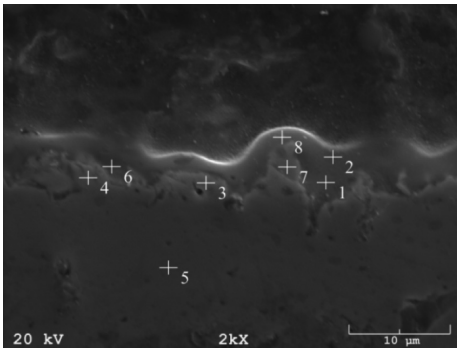

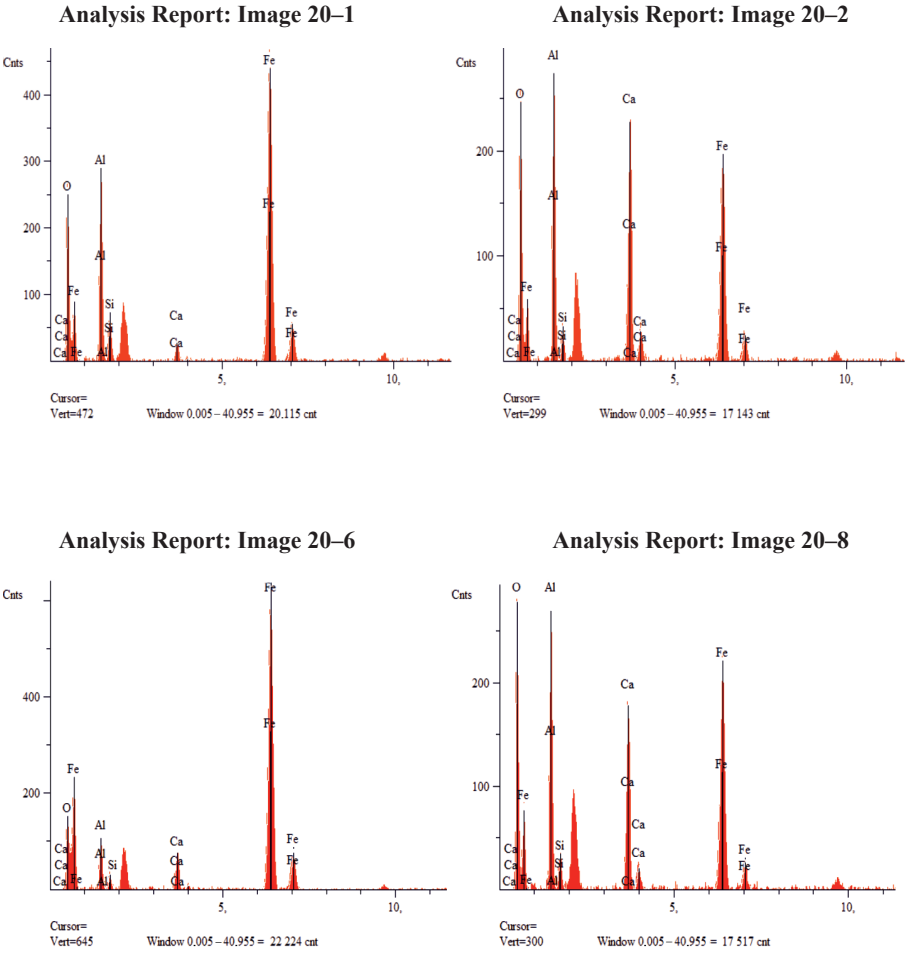

Fig. 20. Steel sheet immersed in water with the addition of tuff, the exposure period in water – 14 days; transverse metallographic section. Visible is the layer of thickness from 2 to 4 µm. EDS analysis

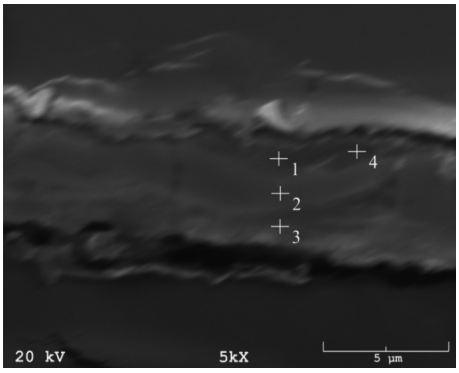

Analysis Report: Image 21–1

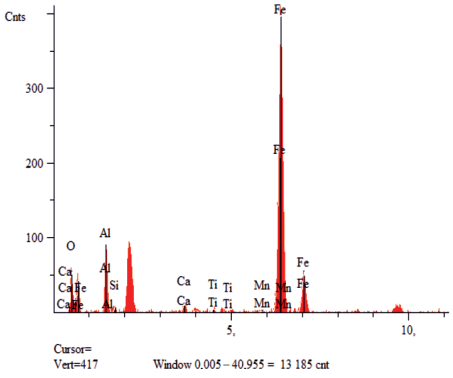

Analysis Report: Image 21–2

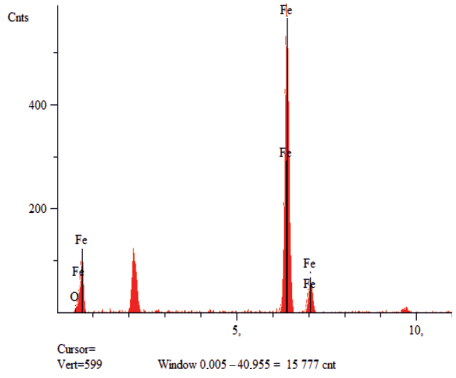

Analysis Report: Image 21–3

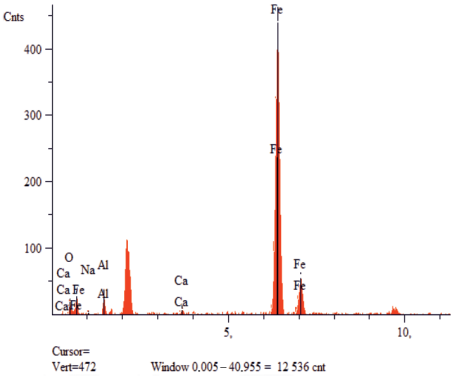

Analysis Report: Image 21–4

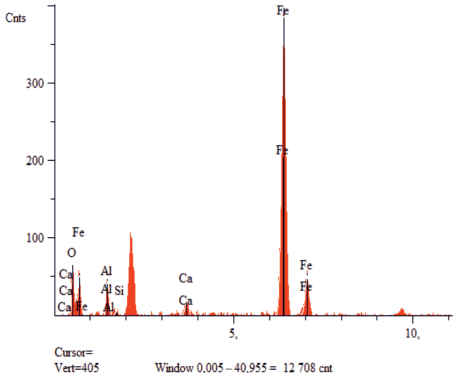

Fig. 21. The cross section of water + tuff sample (after 60 days). EDS analysis

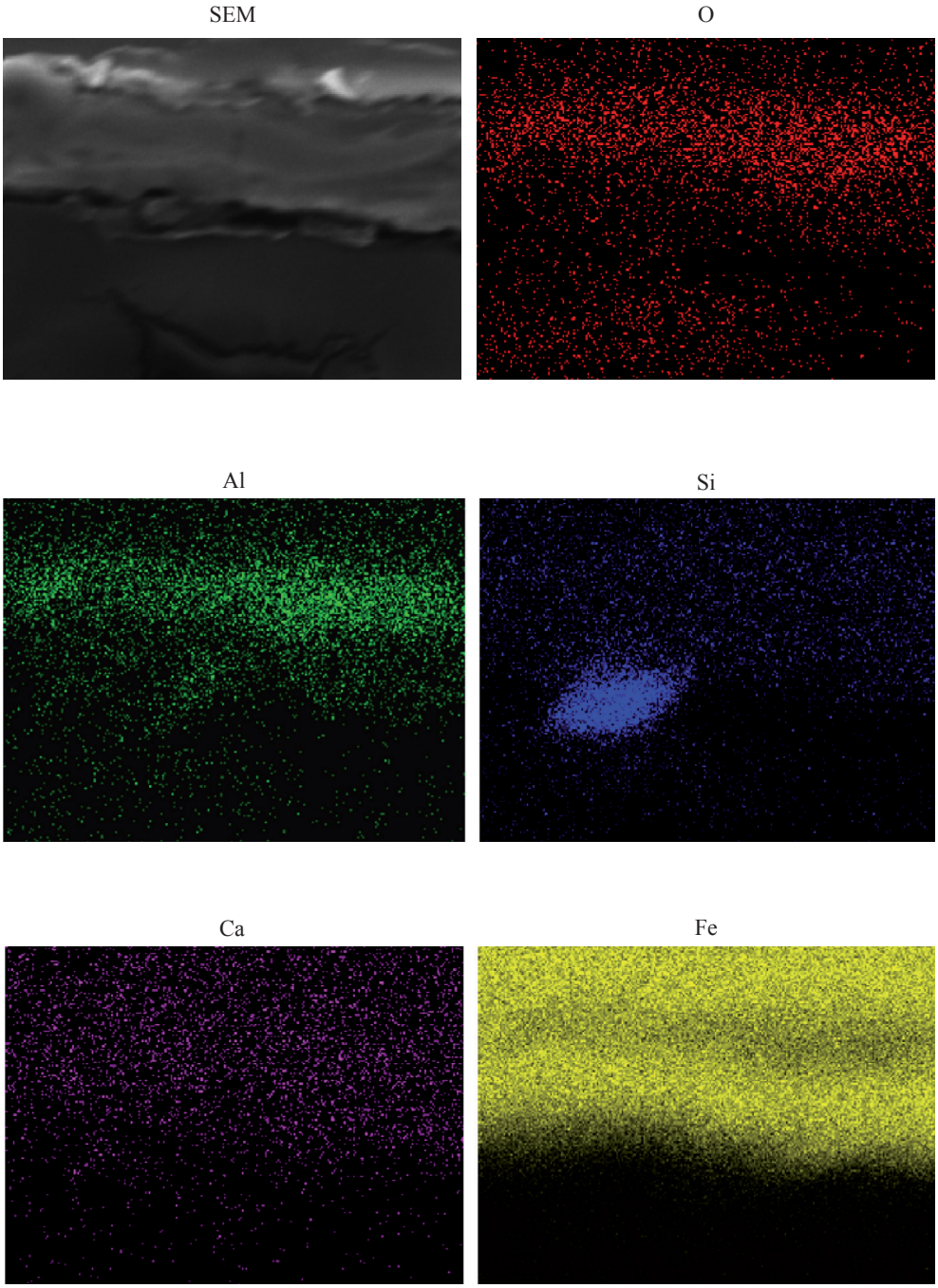

Fig. 22. The cross section of water + tuff sample (after 60 days) – the distribution of elements: O, Al., Si, Ca, Fe

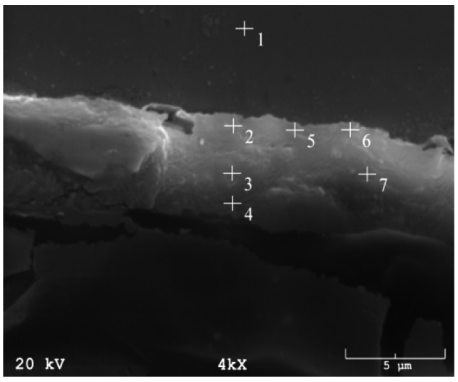

Analysis Report: Image 23–1

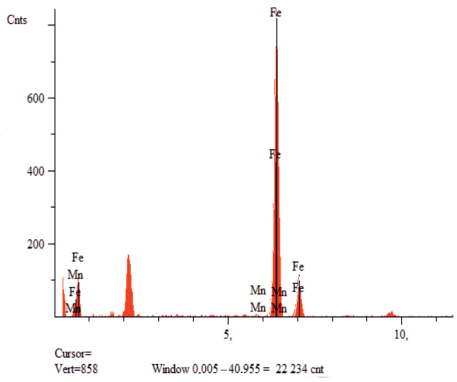

Analysis Report: Image 23–2

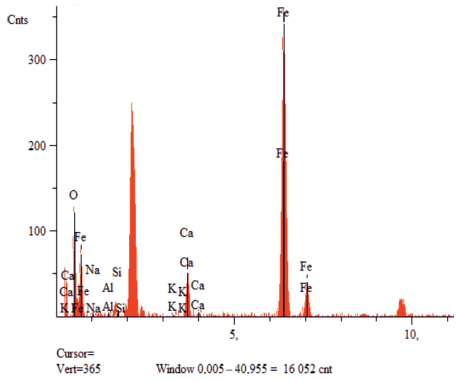

Analysis Report: Image 23–3

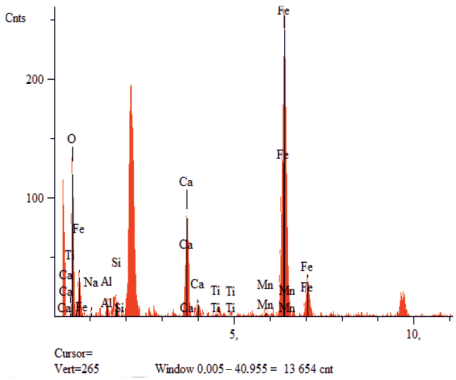

Analysis Report: Image 23–4

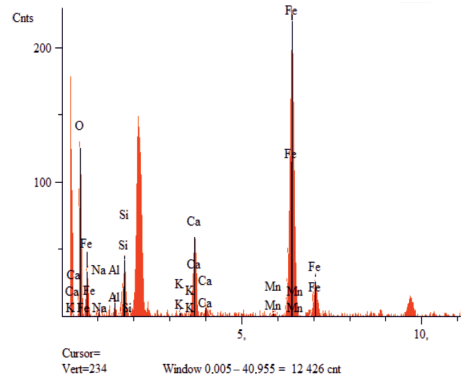

Fig. 23. Steel sheet – 3% solution of NaCl + tuff (after 14 days), the transverse metallographic section. EDS analysis

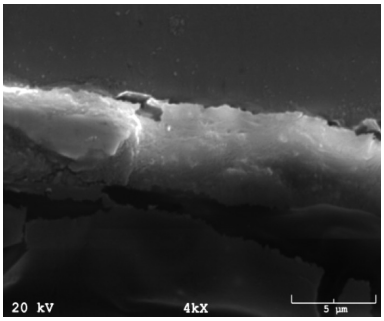

Fig. 24. Steel sheet –3% solution of NaCl + tuff (after 14 days), the transverse metallographic section

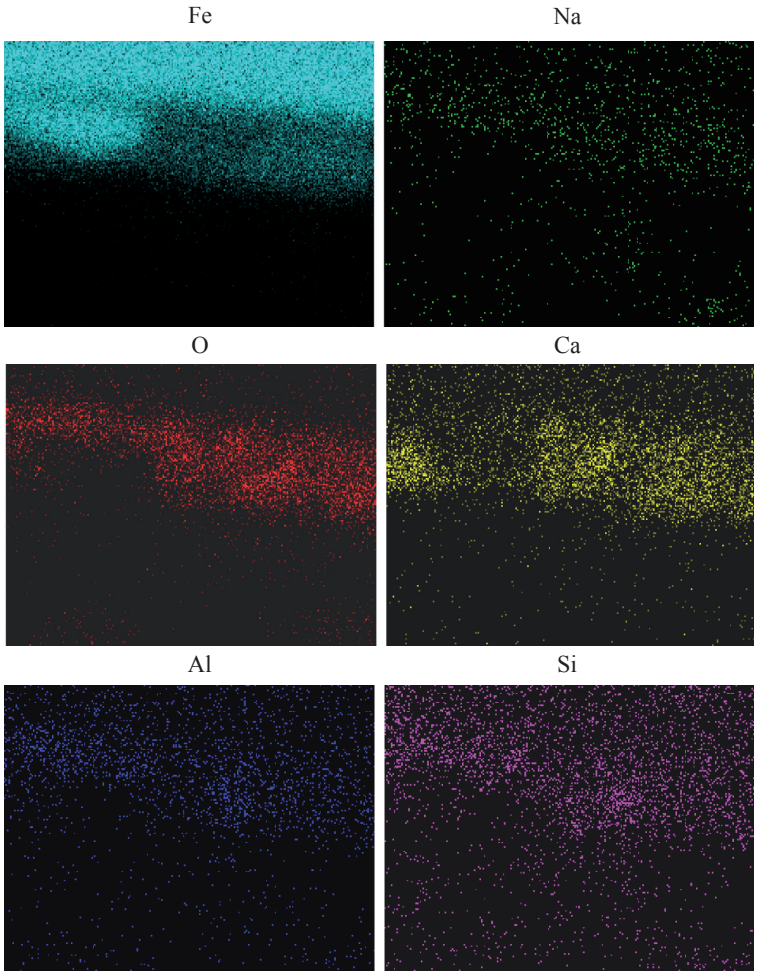

Fig. 25. The cross section of sample immersed in 3% solution of NaCl + tuff (after 14 days) – the distribution of elements: Fe, Na, O, Ca, Al, Si

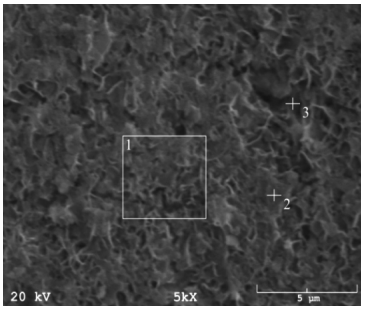

Analysis Report: Image 26–1 **Analysis Report: Image 26–2**

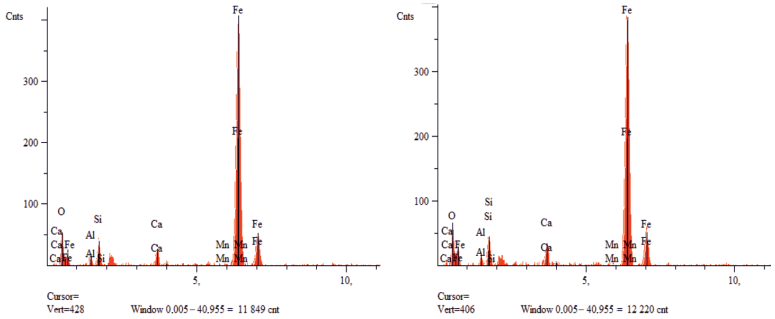

Fig. 26. Steel sheet surface – 3% solution of NaCl + tuff (after 60 days). EDS analysis

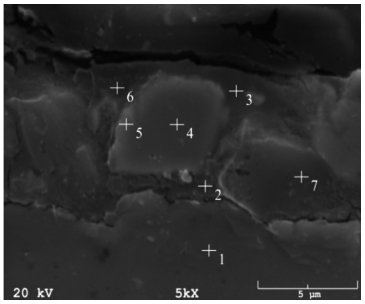

Analysis Report: Image 27–1 **Analysis Report: Image 27–2**

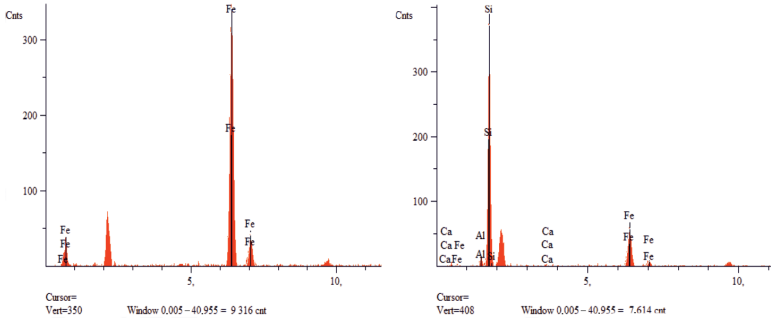

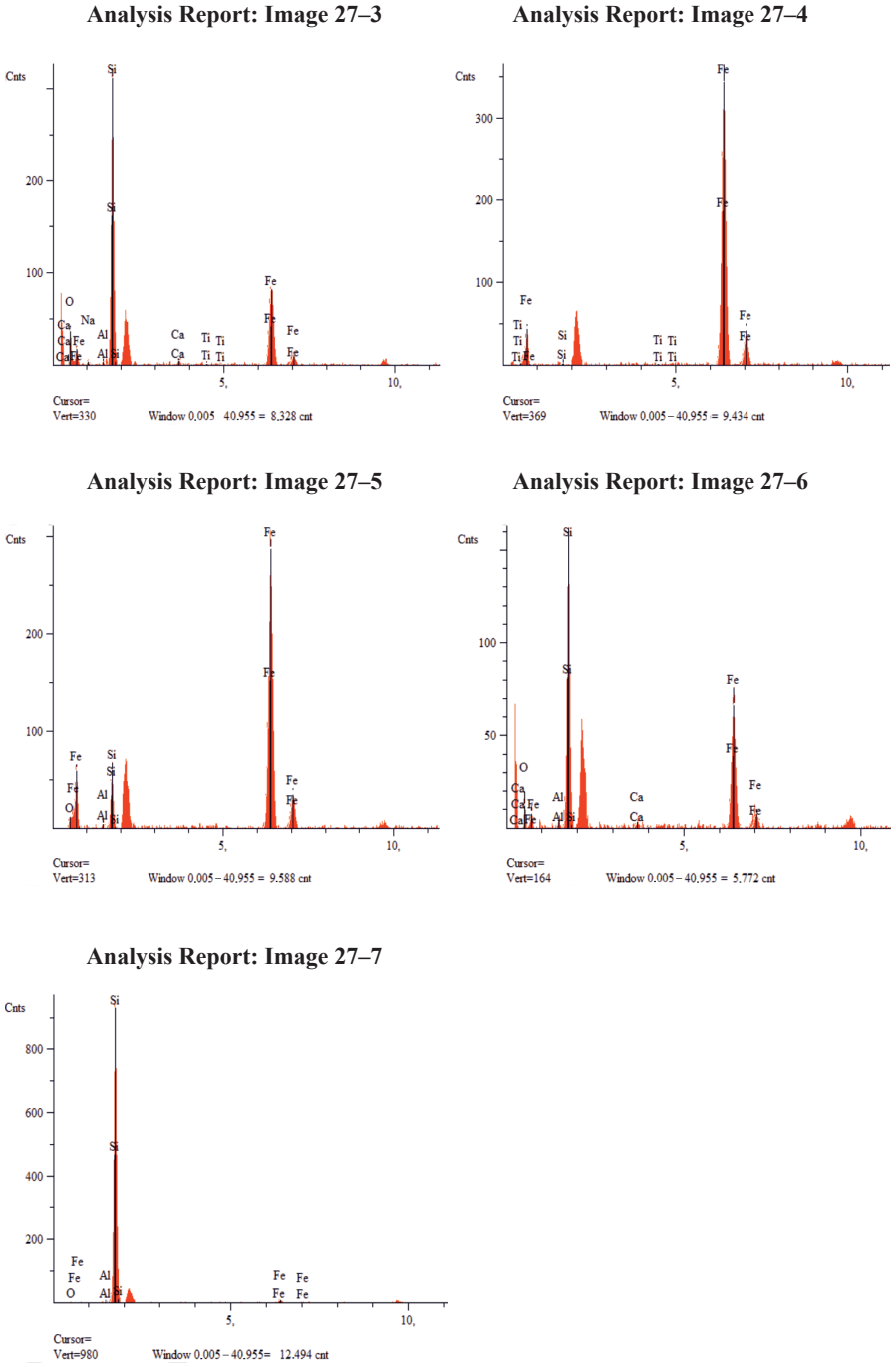

Fig. 27. Steel sheet –3% solution of NaCl + tuff (after 60 days), the transverse metallographic section. EDS analysis

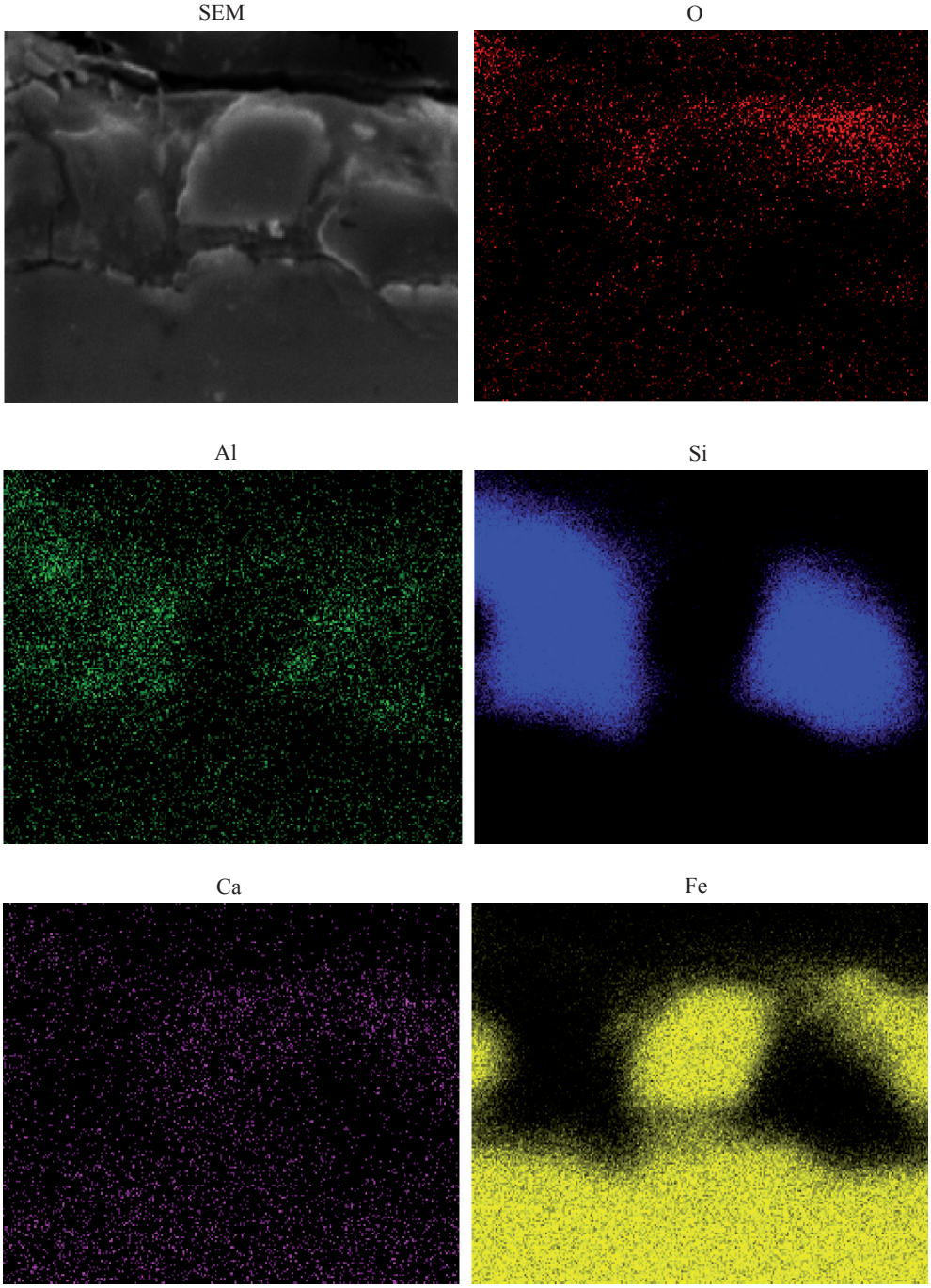

Fig. 28. The cross section of sample – 3% solution of NaCl + tuff (after 60 days) – the distribution of elements: O, Na, Al, Si, Ca, Fe

Studies carried out by SEM and EDS showed that in the case of steel samples immersed in water with the addition of tuff, after 14 days of exposure in the solution (Fig. 20), the protective coating 2 to 5 μm thick was formed. The protective coating had a laminated structure. In the coating area directly contacting the steel surface, the presence of a layer comprising Fe, Al, Si and O was observed. The upper part of this layer contained Al, Ca, Fe, Si and O.

In the case of samples immersed for 60 days in water with the addition of tuff (Fig. 21, 22), the thickness of protective coating was approximately 6 to 7 μm. The coating had an obviously layered structure. Near the steel surface, there was a layer containing Fe, Al and O, the next layer contained Fe, and again there was a layer containing Fe, Al and O. The concentration of Ca and Si was uniform across the entire thickness of the coating. The results of EDS test have indicated that oxygen concentration in individual layers of the film was correlated with the concentration of Al. Elemental distribution analysis has confirmed that high oxygen concentrations were present in areas with the high concentration of aluminum, while in areas with the high concentration of Fe, virtually no oxygen was present.

In samples immersed for 14 days in 3% NaCl solution with the addition of tuff (Fig. 23–25), the thickness of protective coating amounted to about 55 μm. Also in these coatings, similar as in coatings exposed to water, a layered structure was observed. The coatings contained Fe, O, Na, Ca, Al and Si. In areas with the high concentration of Fe, a marked reduction in the oxygen concentration was noticed. In areas with the low concentration of Fe, high concentrations of Ca, Si and O, and increased concentrations of Al and Na occurred.

In samples immersed for 60 days in 3% NaCl solution with the addition of tuff (Fig. 26–28), the thickness of protective coating was 7 to 8 μm. The structure of these coatings was observed to differ from the structure of coatings exposed to the effect of water with the addition of tuff. It consisted of two types of complexes (areas) – the first type of complex with high concentration of Fe and very low concentration of oxygen, and the second type of complex with high concentration of Si, high concentration of Al and very low concentration of oxygen. The complexes were embedded in the matrix composed mainly of Si, Fe and O, with low concentration of Al and Ca.

5. Conclusions

1. Tuff in aqueous solutions inhibits steel corrosion by forming a protective film (coating) composed of the steel corrosion products and products of the volcanic tuff hydrolysis.
2. The formation of protective layer on the steel surface is a multi-step process and consists of the process of tuff hydrolysis (preparation of the sol solution), the deposition of coating in the form of sol on the steel, the formation of cross-linked gel by polymerization of the sol particles, the formation of amorphous or crystalline coating during drying.
3. Tuff particles introduced to an aqueous environment are undergoing the processes of hydration and hydrolysis. As a result of these processes, the most easily soluble mineral components are dissolved and washed out. Ions of Si^{2+} and Al^{3+} Ca^{2+} are the most mobile cations, while in the grains of tuff remain the less mobile components. The decomposition products are transported as suspensions, colloidal solutions and real

solutions. The synthesis of sols of hydroxides of Al, Si, Ca, Fe and of other components to which the tuff is decomposed takes place. Under certain conditions, hydroxides mutually coagulate and precipitate in the form of gel.

4. The transition between the state of sol and complete gel is running continuously as a result of advancing parallel processes of hydrolysis and condensation, which are highly beneficial for the coating adhesion.
5. Gel is formed when, in a colloidal system, the number of colloidal particles is so high that they contact or communicate with each other at many points, forming a space lattice system. During drying, the excess water is removed. The end result of this process is the amorphous or crystalline material.
6. The complex composition of the resulting layer formed on the steel surface is most likely due to the sorption by gels, from which it arises, of additional elements from the aqueous solution. As a result of this process, on the steel surface, a protective layer is formed, and it consists of the steel corrosion products and tuff hydrolysis products.
7. Introducing properly prepared tuff formulations to protective coatings (including protective paints) is expected to improve the corrosion resistance while maintaining the sufficiently high mechanical strength properties of the coating.

References

[1] Szklarska-Śmiałowska Z., *Inhibitory korozji metali*, Wydawnictwo Naukowo-Techniczne, Warszawa 1971.

[2] Svoboda M., Mleziva J., *Properties of coatings determined by anti-corrosive pigments*, Prog. Org. Coat. 12, 1984, 1–297.

[3] Fletcher T., *Inhibitowanie korozji w farbach antykorozyjnych i rola pigmentu inhibitującego*, Ochrona przed korozją, 7/2006, 213–221.

[4] Cohen M., *Korozja*, pod redakcją L.L. Shreira, Tom 2, *Ochrona przed korozją*, WNT, Warszawa 1966, 525, 733.

[5] Bielski W., *Zabezpieczenie antykorozyjne i przeciwosadowe instalacji c.o. przy użyciu inhibitorów FERNOX*, Czasopismo INSTAL 06/2003, 34–37.

[6] Polakow K.A., *Chemicznie odporne materiały niemetalowe*, Państwowe Wydawnictwa Techniczne, Warszawa 1955.

[7] Kuczyńska H., *Badania silanowych promotorów adhezji w wodorozcieńczalnych farbach epoksydowych*, Ochrona przed korozją 5/2005, Wydawnictwo SIGMA-NOT, 156.

[8] Koźlak W., *Studia nad niektórymi właściwościami i strukturą wodnych roztworów krzemianów technicznych*, Praca doktorska, Politechnika Warszawska, 1980.

[9] Salensky G., *Corrosion inhibitors in Handbook of Coating Additives*, ed. Calbo L.J; Marcel Dekker, inc. 1987; Chapter 12.

[10] Sredenicki J., Gulaj O., *Termoutwardzalne krzemoorganiczne powłoki na rurociągi*, Ochrona przed korozją, 3/2001, Wydawnictwo SIGMA-NOT Sp. Z o.o., Warszawa 2001, 3–8.

[11] Kwiatkowski J., *Wyroby lakierowe do malowania podłoży metalowych*, Ochrona przed korozją 1/2001, Wydawnictwo SIGMA-NOT Sp. z o.o., Warszawa 2001, 16–17.
[12] Blicharski M., *Inżynieria powierzchni*, WNT, Warszawa 2012.
[13] Beving D.E., McDonnell A.P., Yang W., Yan Y., *Corrosion Resistant High-Silica-Zeolite MFI Coating*, Journal of The electrochemical Society, nr 153 (8) B325–B329, 2006.
[14] Bereś B., *Zarys mineralogii i petrografii*, olitechnika Wrocławska, Wrocław 1992.
[15] Godimchuk A.Yu., Ilin A.P., *Badanie procesów sorpcyjnych na naturalnych składnikach mineralnych oraz ich form termomodyfikowanych*, Chem. i techn. wody, t. 26, No. 4, 2004, 287–298.
[16] Kobasa I., Mikuła J., Woloschuk A., Tsymbaliuk W., *Influence of Thermal Treatment on The Physical, Mechanical And Sorption Characteristics Of Basalt Tufa*, Czasopismo Techniczne 5-M/2011, Wydawnictwo Politechniki Krakowskiej, 3–9.
[17] Mikuła J., Łach M., *Potencjalne zastosowania glinokrzemianów pochodzenia wulkanicznego*; Czasopismo Techniczne 8-M/2012, 111–124.
[18] Mikuła J., Łach M., *Wytwarzanie i właściwości geopolimerów na bazie tufu wulkanicznego*, Inżynieria Materiałowa – 2014, R. 35, Nr 3 (199), 270–276 (A).
[19] Ramachandran V.S., *Concrete Admixtures Handbook*, William Andrew Publishing, 1995.

TECHNICAL TRANSACTIONS | CZASOPISMO TECHNICZNE
MECHANICS | MECHANIKA
5-M/2016

DOI: 10.4467/2353737XCT.16.284.6116

TOMASZ HUŚCIO, ROMAN TROCHIMCZUK*

ROPE-FREE MULTI-CABIN ELEVATOR SYSTEM FOR VERTICAL AND HORIZONTAL TRANSPORT AND SIMULTANEOUS INTEGRATION OF MOVEMENT IN TWO DIRECTIONS

SYSTEM WIELOKABINOWEJ BEZLINOWEJ WINDY DO TRANSPORTU PIONOWEGO I POZIOMEGO ORAZ W DWÓCH KIERUNKACH JEDNOCZEŚNIE

Abstract

This article presents a novel rope-free multi-cabin elevator system for vertical and horizontal transport and simultaneous integration of movement in two directions. Using the patent applications to the Patent Office of the Republic of Poland, the structure and the principle of operation of the rope-free elevator is presented. The advantages of using the mechatronic rope-free multi-cabin elevator in novel, multi-area high rise buildings are presented. The directions of further studies are outlined.

Keywords: elevator, rope-free elevator, vertical and horizontal elevator, multi-cabin elevator

Streszczenie

W artykule przedstawiono nowatorskie rozwiązanie systemu wielokabinowej bezlinowej windy do transportu pionowego i poziomego oraz w dwóch kierunkach jednocześnie. W oparciu o dokonane autorskie zgłoszenia patentowe do Urzędu Patentowego Rzeczypospolitej Polskiej opisano budowę i zasadę działania bezlinowej windy. Wskazano zalety zastosowania proponowanego rozwiązania w nowoczesnych, wielkopowierzchniowych, wielokondygnacyjnych budynkach. W podsumowaniu wskazano kierunki dalszych badań nad prototypowym rozwiązaniem.

Słowa kluczowe: winda, bezlinowa winda, winda do transportu pionowego i poziomego, system windy wielokabinowej

* Ph.D. Eng. Tomasz Huścio, Ph.D. Eng. Roman Trochimczuk, Department of Automatic Control and Robotics, Faculty of Mechanical Engineering, Bialystok University of Technology.

1. Introduction

In large urban agglomerations, due to limited areas of construction lots, developers are investing into the construction of very tall, multi-storey buildings intended as residential, office, or commercial buildings. Solutions of this type pose a very big engineering and logistical challenge. The materials and techniques of raising such buildings require the application of technologically advanced methods and construction techniques as well as modern, strong, and light materials from designing teams. Modern skyscraper designs account for factors, such as: increased action of atmospheric factors (e.g. wind, rain, snow, variable temperature dependent on height), disrupted equilibrium of the building due to tectonic movements, or even a potential terrorist attack, which is being taken very seriously after the events at the World Trade Center in 2001.

The only element of skyscraper design and construction that has remained practically unchanged since its inception is the elevator. Of course, modern elevators differ in terms of appearance, applied structural materials, drives, equipment, speed, and noise level during movement compared to the first designs invented and used in the 19th century. However, the principle of their operation remains essentially unchanged. This principle is the movement of cabins between storeys of buildings on the vertical plane (in a shaft) with the application of load-bearing tension members (lines, chains) [1, 2].

To increase transportation capabilities in high-rises, complexes of multiple shafts are usually built, in which even several cabins may move simultaneously in more recent solutions. In the case of very tall, multi-storey, large-area buildings, the systems available on the market may prove insufficient. In particular, this may pertain to the situation of elevator operation during hours of increased operation (morning or afternoon load arising from the beginning or end of the workday, holiday, etc.) or emergency situations (e.g. fire on a given storey of a building).

In relation to the above, it seems purposeful to develop modern elevator designs that simultaneously serve for vertical and horizontal transport, with cabins, and whose movement within the building is not limited by the design of individual shafts.

This article presents an innovative solution of an elevator for transportation of persons and objects in the vertical and horizontal direction as well as in both directions simultaneously, with the capability of moving cabins over a track of arbitrary shape. Depending on the actual needs, surface area, and number of storeys of the building, as well as the number of rooms to which cabins may travel, an elevator can have a single cabin or multiple cabins.

2. Selected modern elevator solution

The main engineering problem facing designers of modern tower blocks is the distribution and number of communication routes, transportation channels, and potential evacuation routes. Arrival at a given storey of a building must be as fast as possible. Currently applied elevator solutions with an engine room and traditional vertical shaft are becoming increasingly inefficient and insufficient, particularly with regard to high-rises.

By analyzing selected works in the scope of de-signing new multi-cabin solutions for elevator systems [3–10], the primary sources of problems that may appear during elevator operation can be defined. Such problems include, among others: types and lengths of ropes used, vibrations during movement, the problem of cabin rocking during movement at high speeds, the types of drives used in the design, as well as very important issues related to safety of elevator use. These problems can be eliminated by applying rope-free elevator systems.

In most studies, the authors mainly focus on researching new algorithms for controlling elevator systems currently applied in multi-storey buildings. However, in the presented innovative solutions, direct drive linear motors are used as the drive source. Published results of studies confirm the hypothesis that drives of this type may contribute to solving problems arising from application of a rope as the tension member drawing the elevator cabin. However, cabin movement remains restricted by the shaft walls, and it can only be horizontal or vertical.

Information concerning an innovative elevator design by the ThyssenKrupp company from Germany appeared in the media at the end of 2014. Its trade name is MULTI [11, 12]. In the proposed solution, the cabin moves on both the horizontal and the vertical plane. The solution is based on linear motors and utilizes the phenomenon of magnetic levitation. According to reports, the proposed solution may revolutionize the elevator system used until now. The same company also developed an innovative solution based on placing two cabins in a single shaft [13], which is intended to increase transportation capabilities.

Neither of these solutions provides a single cabin with the capability of simultaneous movement in two directions. Moreover, it is not possible to arbitrarily shape the form of the shaft in which cabins travel. This may be of great importance when designing multi-storey buildings with imaginative shapes.

3. Design and principle of operation of the original rope-free elevator

Fig. 1 presents the general concept of the rope-free elevator with cabins moving vertically, horizontally and in two directions at once. The elevator consists of cabins (1) moving over the wall of a shaft (2) situated inside of a building (3). Cabins (1) may be: single-door – with one entrance; double-door – with two opposite entrances; angular – with two entrances at an angle of 90° relative to one another; three-sided – with three entrances on neighboring walls; four-sided – with four entrances – one on each wall. Cabins may move in a closed or partially open shaft.

The elevator's drive utilizes a planar positioning system with Hall sensors. A detailed description of the design and principle of operation of planar positioners can be found in works [14–22], among others.

Fig. 2 presents components of the rope-free elevator for transport in the vertical and horizontal direction as well as in both directions simultaneously in the example configuration with one cabin and two opposite entrances.

The main components of the cabin's planar positioning system are immobile planar stators (4) installed on the shaft surface (2) and mobile planar forcers (6) installed on the

exterior side surfaces of the cabin (1). Electromagnetic drive modules installed on the bearing surfaces of planar forcers (6) are responsible for moving the cabin (1) over the track comprising planar stators (4) and for attraction of the cabin (1) to the stators (4). Planar stators (4) serving for movement of the cabin (1) can form a track of any shape or can be distributed over the entire surface of the shaft's (2) walls. This solution allows for movement of the cabin (1) in the horizontal and vertical direction as well as in both directions at the same time, enabling travel to any door (7) of a room or door leading to a corridor.

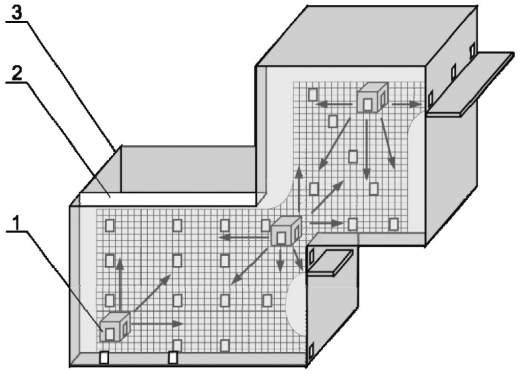

Fig. 1. Rope-free multi-cabin elevator system for vertical and horizontal transport and simultaneous integration of movement in two directions [23]

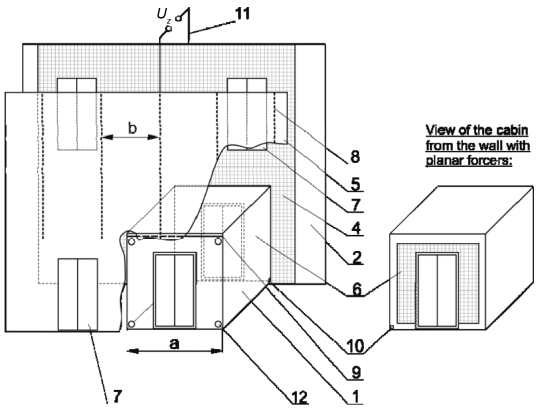

Fig. 2. The main elements of rope-free elevator system [23]

The cabin (1) moves over the shaft (2) without coming into contact with it thanks to the application of aerostatic bearings. A layer of air with pressure greater than atmospheric pressure is generated between forcers (6) and stators (4), forming an air cushion that balances the forces of electromagnetic attraction of forcers (6) to stators (4), among others. The above necessitates equipping every cabin with its own source of compressed air, which is indispensable for generating the air cushion between the planar stators (4) and the planar forcers (6). A compressor with a pressure vessel or a pressure vessel by itself can be installed

on the elevator cabin. Another option is to install a station generating compressed air in the shaft, to which the cabin (1) would have to travel and connect to (dock) in order to replenish air in the pressure vessel.

In order to ensure a constant height of the air gap over the entire area of stator/forcer inter-operation, a system of supporting elements (12) made up of kinematic pairs with three degrees of freedom, all rotating.

Electrical supply to the cabin (1) is carried out by means of a contact system (Fig. 2). A contact system (8) for power supply is distributed on the wall (5). Electricity flows from power supply cables (8) through the current collector (9) to the cabin's (1) electrical system powering individual forcers (6), the compressor, which is required for generating the air cushion, and the control system along with the operator's panel and cabin lighting. From receivers in the cabin (1), electrical current flows through the return current collector (10), stators (4) and the cables connected to them (11). Electrical power supply to the cabin necessitates the distribution of individual power supply cables (8) at *a* distance *b* less than distance *a* of the current collector (9) placed on the cabin's wall (1). This solution ensures uninterrupted contact of current collectors (9) with the network of power supply cables (8) during movement of the cabin (1) over a track of any shape made up of stators (4).

4. Advantages of application of the innovative solution

The rope-free elevator can be applied in multi-storey buildings in which the distribution and number of rooms to which the cabin is to travel necessitates the application of an arbitrary shape of transportation routes in the shaft. The proposed system has indisputable advantages that may bring new quality to intra-building transport of persons and objects. Among them, the following deserve special attention [23–25]:

- the elevator is rope-free – there is no need to install a machine room or lines on which cabins would be suspended in shafts,
- transport can take place vertically and horizontally as well as in two directions of movement simultaneously,
- a track of any shape can be formed over the entire surface of the shaft's walls for movement of cabins in the vertical and horizontal directions as well as in both directions at once,
- the ability to arbitrarily shape the track on the surface of the shaft allows for the application of the proposed solution in buildings with imaginative shapes,
- the application of aerostatic bearings in the drive system eliminates wear between inter-operating surfaces of stators and forcers; there is no need for periodical lubrication of guides, which translates to limitation of activities related to maintenance of the transportation system and reduction of operating costs,
- in the case of an emergency situation related to e.g. loss of electrical power or pneumatic supply required for generation of the air cushion, because electromagnetic drive modules contain strong rare earth magnets, the cabin will not fall, but rather be drawn to the shaft wall, where it will remain safely until the problem is solved by technical teams or the emergency power supply system is activated,

- the multi-cabin system enables optimal configuration of the number of cabins moving in the shaft over a track of arbitrary shape, which allows for rapid and flexible reaction to actual transportation needs within a given large-area building,
- capability of achieving greater cabin movement speeds compared to typical solutions due to the lack of the air cushion effect, resulting in resistance during vertical movement of a cabin in a standard shaft.

5. Summary

The original solution of a rope-free elevator with cabins moving vertically, horizontally and in two directions at once was presented in this article. Single- or multi-cabin passenger, freight, passenger and freight, car, etc. elevators can be installed in newly built or existing buildings based on the proposed solution.

The drive of the rope-free elevator, made on the basis of planar positioner units with Hall sensors, allows for designing of an elevator with a shaft of any shape as well as a multi-walled shaft enabling movement of cabins from one wall to a neighboring wall of the shaft. In the basic configuration, such a shaft can consist of two walls sharing an edge, positioned at a right angle relative to one another. Based on this solution, elevator shafts consisting of multiple walls over which cabins can travel can be built.

Within the framework of further work on the design of the rope-free elevator, expansion of the research laboratory station to an extent enabling testing of the programs responsible for collision-free control of the system, studying the behavior of cabins under varying loads in dynamic conditions, and assessment of vibration damping by the air cushion separating stators from inductors, is planned. The results will be used to elaborate the rope-free multi-cabin elevator system and for quick and flexible reaction to actual transport needs within a given large-area building, as well as for fast and safe arrival of passengers to individual rooms of the building. The development algorithms will be implemented in the laboratory station and used in the mechatronic rope-free multi-car elevator system after being verified.

This research has been done as a part of a statutory research of Department of Automatic Control and Robotics, Faculty of Mechanical Engineering which is funded by Bialystok's University of Technology, Poland.

References

[1] McCain Z., *Elevators 101*, Elevator Word, 2004.
[2] Strakosch G.R. (Editor), *The Vertical Transportation Handbook*, Wiley Online Library, 2007.
[3] Ishii T., *Elevators for skyscrapers*, IEEE Spectrum, 31 (9), September 1994, 42–46.
[4] Hong Sun Lim, Krishnan R., *Ropeless elevator with linear switched reluctance motor drive actuation systems*, IEEE Transactions on Industrial Electronics – IEEE Trans Ind Electron, vol. 54, no. 4, 2007, 2209–2218.

[5] Sakamoto T., Noma Y., *Guidelines for VSS Controller Design of LSM-Driven Ropeless Elevator*, IEEE International Symposium on Industrial Electronics, Seoul, 5–8 July 2009, 1564–1568.
[6] Schmulling B., Effing O., Hameyer K., *State Control of an Electromagnetic Guiding System for Ropeless Elevators*, European Conference on Power Electronics and Applications, Aalborg, 2–5 September 2007, 1–10.
[7] Toida K., Honda T., Houng-Joong K., Watada M., Torii S., Ebihara D., *The positioning control with velocity feed-forward for the rope-less elevator using linear synchronous motor*, Conference: Electric Machines and Drives IEEE International Conference – IEMDC, 1997.
[8] Yamaguchi H., Osawa H., Watanabe T., Yamada H., *Brake control characteristics of a linear synchronous motor for ropeless elevator*, Advanced Motion Control, 1996. AMC '96-MIE. Proceedings, 1996 4th International Workshop on, Vol. 2, 1996, 441–446.
[9] http://www.elevatorword.com (access: 20.12.2015).
[10] Liu J., Wu Y., Dai J., Liu M., Wu Ch., Gao E., *Overstep Control Analysis for Multi-car Elevator*, Proceedings of 2012 International Conference on Modelling, Identification and Control, ICMIC, IEEE, Wuhan, Hubei, China 2012, 24–26 June, 254–259.
[11] www.designboom.com/technology/worlds-first-rope-free-elevator-multi-12-05-2014 (access: 20.12.2015).
[12] www.dezeen.com/2014/12/01/thyssenkrupp-multi-elevator-uses-magnets-to-move-vertically-and-horizontally (access: 20.12.2015).
[13] ThyssenKrupp Elevator 2015, *Two elevator cabs have always meant two shafts. Until now. TWIN – A singular revolution in elevator design*, www.thyssenkruppelevator.com/downloads/TWIN.pdf. (access: 20.12.2015).
[14] Huścio T., *Modelowanie płaskich podpór pneumatycznych z napędem elektromagnetycznych*, Doctoral thesis, Politechnika Białostocka, Białystok 2009.
[15] Trochimczuk R., *Mechatroniczne pozycjonowanie wiązki lasera impulsowego w urządzeniach do formowania obiektów trójwymiarowych w szkle*, Doctoral thesis, Kraków, Akademia Górniczo-Hutnicza, 2009.
[16] Kuźmierowski T., Trochimczuk R., *Application of planar positioning system in selected mechatronic structure*, International Journal of Applied Mechanics and Engineering, Vol. 17, No. 4, 2012, 1377–1384.
[17] Kallenbach E., Kireev V., Volkert R., Zentner J., Bertram T., *Configuration and Control Aspects of High-Precision Planar Multi-Coordinate Drive Systems*, ASPE 19th Annual Meeting, Orlando, Florida 2004, 185–188.
[18] Huścio T., Trochimczuk R., *Mechatroniczne urządzenie rehabilitacyjne zbudowane na bazie pozycjonera planarnego*, Mechanik Nr 10/2015, DOI: 10.17814/mechanik.2015.10.519, 808–811.
[19] Quaid A.E., Hollis R.L., *Cooperative 2-DOF Robots for Precision Assembly*, International Conference on Robotics and Automation, Minneapolis, April 22–28, 1996.
[20] Lauwers T.B., Edmondson Z.K., Hollis R.L., *Progress in agile assembly: minifactory couriers based on free-roaming planar motors*, 4th Int'l. Workshop on Microfactories, Oct. 15–17, Shanghai, P. R. China 2004, 7–10.

[21] Hollis R.L., Gowdy J., *Miniature Factories for Precision Assembly*, Proc Int'l Workshop on Micro-Factories, December 7–8, Japan, Tsukuba 1998.
[22] Hollis R.L., Gowdy J., Rizzi A.A., *Design and Development of a Tabletop Precision Assembly System,* Mechatronics and Robotics, (MechRob'04), September 13–15, Germany, Aachen 2004, 1619–1623.
[23] Huścio T., Trochimczuk R., *Mechatroniczna bezlinowa winda do transportu pionowego i poziomego z możliwością przemieszczania kabin w zamkniętym lub w częściowo otwartym szybie*, Patent Application nr P.415251, Patent Office of the Republic of Poland.
[24] Trochimczuk R., Huścio T., *System przemieszczania kabiny do mechatronicznej bezlinowej windy do transportu pionowego i poziomego oraz w dwóch kierunkach jednocześnie w zamkniętym lub w częściowo otwartym szybie*, Patent Application nr P.415270, Patent Office of the Republic of Poland.
[25] Huścio T., Trochimczuk R., *System przemieszczania kabiny do mechatronicznej bezlinowej windy do transportu pionowego i poziomego oraz w dwóch kierunkach jednocześnie w zamkniętym lub w częściowo otwartym szybie*, Patent Application nr P.415269, Patent Office of the Republic of Poland.

TECHNICAL TRANSACTIONS | CZASOPISMO TECHNICZNE
MECHANICS | MECHANIKA
5-M/2016

DOI: 10.4467/2353737XCT.16.285.6117

MAREK S. KOZIEŃ, DARIUSZ SMOLARSKI*

APPLICATION OF THE DIRECT SPECTRAL METHOD TO CYCLE IDENTIFICATION FOR MULTIAXIAL STRESS IN FATIGUE ANALYSIS

ZASTOSOWANIE METODY SPEKTRALNEJ BEZPOŚREDNIEJ DO IDENTYFIKACJI CYKLI DLA WIELOOSIOWEGO STANU NAPRĘŻEŃ W ANALIZIE ZMĘCZENIOWEJ

Abstract

In the article, the means of application of the direct spectral method for the identification of the stress cycles for multiaxial stress is discussed. Two cases are analyzed. The first, when components of stress tensor are in phase, and the second, when they are shifted in phase. The second case is associated with the practical application for the crane wheel.

Keywords: fatigue analysis, cycle counting, spectral method, multiaxial stress

Streszczenie

W artykule przedstawiono sposób zastosowania metody spektralnej bezpośredniej do identyfikacji cykli naprężeń o charakterze wieloosiowym. Rozważane są dwa przypadki. Pierwszy, gdy składowe tensora naprężeń są zgodne w fazie i drugi, gdy są one przesunięte w fazie. Drugi przypadek jest związany z praktycznym zastosowaniem dla koła suwnicy.

Słowa kluczowe: analiza zmęczeniowa, zliczanie cykli naprężeń, metoda spektralna, naprężenia wieloosiowe

* Ph.D. D.Sc. Eng. Marek S. Kozień, Institute of Applied Mechanics, Faculty of Mechanical Engineering, Cracow University of Technology.

** M.Sc. Eng. Dariusz Smolarski (Ph.D. student), Faculty of Mechanical Engineering, Cracow University of Technology.

1. Introduction

In the fatigue analyses of engineering structures, it sometimes happens that vibrations of elements have the bi-modal type. Such types have been observed for one of the considered magnetic focusing machine for particles in CERN at the beginning of the 21st century or vibrations of vehicle suspension system analyzed by T.-T.Fu and D.Cebon [6]. Methods of fatigue analysis of the stress history of irregular (non-harmonic) type in time domain, which are known in literature, are in practice associated with one of the cycle counting methods (including the "rain-flow" attempt) [5, 10, 15, 16] or the spectral methods [23–25]. Due to the existence of the two harmonic components with different frequencies in the bi-modal type stress histories, there are limited numbers of articles in which the methods dedicated for this case are proposed [2, 3, 6].

Due to the geometry of the structure, during its vibrations, the generated deformations are reason of the case of multiaxial stress. Fatigue analysis of such cases have been considered for several years with the application of different theories. The authors present only the part of the important articles in this topic, not thinking about doing a review of the completely state-of the art. Reviews and comparisons of different multiaxial fatigue theories can be found e.g. in [7, 9, 26, 28, 32, 33]. The commonly used criterions are based on: empirical equivalent stress approach – Pollard [8], stress invariants – Sines [31], average stress approach – Papadopoulos et.al. [26], critical plane methods – Carpinteri and Spagnoli [4], Dang Van [1, 15], Matake [21], McDiarmid [22], Liu and Mahadevan [17], Papadopoulos [27], energy – Łagoda [18]. The simplest way for fatigue analysis of the multiaxial type stress history is the determination of the equivalent mean stress, equivalent stress amplitude and the equivalent completely reversed stress [1, 5]. In Polish literature, the fatigue analyses of the cases of stress multiaxial are discussed e.g. in [16, 18–20, 25, 28, 29, 30].

The authors proposed an original method of the fatigue analysis for the bi-modal stress history, based on the idea of reconstruction of the histories in the time domain, called the direct spectral method [13, 14]. The preliminary ideas of application of the method for multiaxial stress histories were presented in [11, 12].

The aim of the paper is to present the possibility of application of the direct spectral method for cycle counting of the bi-axial stress in-phase history (simulation) and the multiaxial stress history out-of phase associated with the realistic case of the rail wheel.

2. Basis of the spectral direct method for multiaxial stress

The bi-modal stress history can be theoretically defined in the form:

$$\begin{cases} \sigma_x(t) = A_{x,1}\sin(\omega_1 t + \varphi_{x.1}) + A_{x,2}\sin(\omega_2 t + \varphi_{x,2}) \\ \sigma_y(t) = A_{y,1}\sin(\omega_1 t + \varphi_{y,1}) + A_{y,2}\sin(\omega_2 t + \varphi_{y,2}) \\ \sigma_z(t) = A_{z,1}\sin(\omega_1 t + \varphi_{z,1}) + A_{z,2}\sin(\omega_2 t + \varphi_{z,2}) \\ \tau_{xy}(t) = A_{xy,1}\sin(\omega_1 t + \varphi_{xy,1}) + A_{xy,2}\sin(\omega_2 t + \varphi_{xy,2}) \\ \tau_{xz}(t) = A_{xz,1}\sin(\omega_1 t + \varphi_{xz,1}) + A_{xz,2}\sin(\omega_2 t + \varphi_{xz,2}) \\ \tau_{yz}(t) = A_{yz,1}\sin(\omega_1 t + \varphi_{yz,1}) + A_{yz,2}\sin(\omega_2 t + \varphi_{yz,2}) \end{cases} \tag{1}$$

where:

$A_{x,1}$, $A_{x,2}$, $A_{y,1}$, $A_{y,2}$, $A_{z,1}$, $A_{z,2}$, $A_{xy,1}$, $A_{xy,2}$, $A_{xz,1}$, $A_{xz,2}$, $A_{yz,1}$, $A_{yz,2}$ – stress amplitudes of the harmonic components for the stress tensor components,

ω_1, ω_2 – angular frequencies of the harmonic components,

$\varphi_{x,1}$, $\varphi_{x,2}$, $\varphi_{y,1}$, $\varphi_{y,2}$, $\varphi_{z,1}$, $\varphi_{z,2}$, $\varphi_{xy,1}$, $\varphi_{xy,2}$, $\varphi_{xz,1}$, $\varphi_{xz,2}$, $\varphi_{yz,1}$, $\varphi_{yz,2}$ – phases of the harmonic components for the stress tensor components.

With such a formulation, the component frequencies f_1 and f_2 and corresponding periods T_1 and T_2 can be obtained using the equations (2) and (3).

$$f_1 = \frac{\omega_1}{2\pi}, \quad f_2 = \frac{\omega_2}{2\pi} \tag{2}$$

$$T_1 = \frac{1}{f_1} = \frac{2\pi}{\omega_1}, \quad T_2 = \frac{1}{f_2} = \frac{2\pi}{\omega_2} \tag{3}$$

The basic assumptions and form of the application of the direct spectral method for bimodal waveforms for multiaxial stress can be described as follows:

- Based on the values of periods T_1 and T_2, the so-called block of stress is determined, of which length (time range) T_B depends on the ratio T_1/T_2. It is the smallest integer number of period T_1, for which the ratio T_B/T_2 is an integer. In practical applications, this condition is satisfied approximately, hence assuming the value of T_B, is an arbitrary decision. It depends on the precision of determination of T_1 and T_2, usually by the identification of frequencies f_1 and f_2.
- The primary stress cycle – only one present within the block – has the stress amplitude equal to $A_{k,1} + A_{k,2}$ for each stress component (where $k = x, y, z, xy, xz, yz$), and if not stated otherwise (e.g. constant value present in FFT function of stress' signals, static assembly stress or thermal stress), the average stress value is equal to zero. This assumption is the basis for calculating the equivalent stress amplitude e.g. by the application of the Huber-Mises-Hencky (von Mises) formula (5) [3] and then the equivalent complety reversed stress, e.g. Morrow's type (6) [5].
- The amplitudes of secondary stress cycles vary depending on the value $A_{k,2}$ and the leading waveform of frequency f_1 for each component of stress tensor. Some of the identified cycles are not taken into account, when they do not have the full stress-cycle form. For the slow-changing waveforms of frequency f_1 when comparing to frequency f_2, the amplitudes of the secondary cycles are approximately equal to $A_{k,2}$. The acquired values are the basis to obtain the equivalent amplitude, e.g. by the application of the Huber-Mises-Hencky (von Mises) formula (5) [3], equivalent mean stress value, e.g. in the form of Sines stress (4) [3] and then to obtain the equivalent a completely reversed stress e.g. of Morrow type (6) [3].
- The obtained data, which describes the identified stress cycles for a given waveform, are the basis for fatigue analysis using the chosen stress cumulative hypothesis, e.g. Palmgreen-Miner's (7) [5].

In the analysis, the following parameters are used: equivalent mean stress value (Sines stress) (4), equivalent stress amplitude (according to the von Mises equivalent stress) (5), equivalent completely reversed stress (Morrow stress) (6).

$$\bar{\sigma}_m = \sigma_{1,m} + \sigma_{2,m} + \sigma_{3,m} \tag{4}$$

$$\bar{\sigma}_a = \frac{1}{\sqrt{2}} \sqrt{\left[\sigma_{x,a} - \sigma_{y,a}\right]^2 + \left[\sigma_{x,a} - \sigma_{z,a}\right]^2 + \left[\sigma_{y,a} - \sigma_{z,a}\right]^2 + 6\left[\tau_{xy,a}^2 + \tau_{xz,a}^2 + \tau_{yz,a}^2\right]} \tag{5}$$

$$\sigma_{\mathrm{EQV}} = \begin{cases} \dfrac{\bar{\sigma}_a}{1 - \dfrac{\bar{\sigma}_m}{\sigma_u}} & \text{for } \bar{\sigma}_m > 0 \\ \bar{\sigma}_a & \text{for } \bar{\sigma}_m \le 0 \end{cases} \tag{6}$$

$$B \cdot \sum_{i=1}^{N} \frac{N_i}{\left(N_f\right)_i} = 1 \tag{7}$$

$$T = B \cdot T_B \tag{8}$$

where:

$\bar{\sigma}_m$ – equivalent mean stress,
$\sigma_{1,m}, \sigma_{2,m}, \sigma_{3,m}$ – main values of mean stress,
$\bar{\sigma}_a$ – equivalent stress amplitude,
$\sigma_{x,a}, \sigma_{y,a}, \sigma_{z,a}, \tau_{xy,a}, \tau_{xz,a}, \tau_{yz,a}$ – amplitude stress components,
σ_{ar} – equivalent completely reversed stress,
σ_u – ultimate stress,
N – total number of cycles identified in a block,
N_i – number of cycles with amplitude σ_i identified in a block,
$(N_f)_i$ – number of cycles to damage for stress with amplitude σ_i (S-N curve),
B – number of blocks,
T_B – time length of block,
T – estimated lifetime.

3. Examples of cycle identification by the direct spectral method

3.1. Simulation of the bi-axial in-phase stress history

Let us consider the case when the bi-axial stress' components $\sigma_x(t)$ and $\tau_{xy}(t)$ are of the bi-modal type (9). The time histories are shown in Fig. 1. There are two active frequencies f_1 = 10 Hz and f_2 = 50 Hz. Hence the block length is equal to $T_B = T_1 = 0.1$ s. The amplitudes of normal stress are equal to $A_{x,1}$ = 310 MPa and $A_{x,2}$ = 155 MPa. The amplitudes of shear stress are 10% of the suitable normal ones, hence $A_{xy,1}$ = 31 MPa and $A_{xy,2}$ = 15.5 MPa. It is assumed that material has ultimate stress equal to σ_u=625 MPa. The identified equivalent completely reversed stress cycles after application of the spectral direct method are given in Table 1.

$$\begin{cases} \sigma_x(t) = 310\sin\left(2\pi 10t\right) + 155\sin(2\pi 50t) \\ \tau_{xy}(t) = 31\sin\left(2\pi 10t\right) + 15.5\sin(2\pi 50t) \end{cases} \tag{9}$$

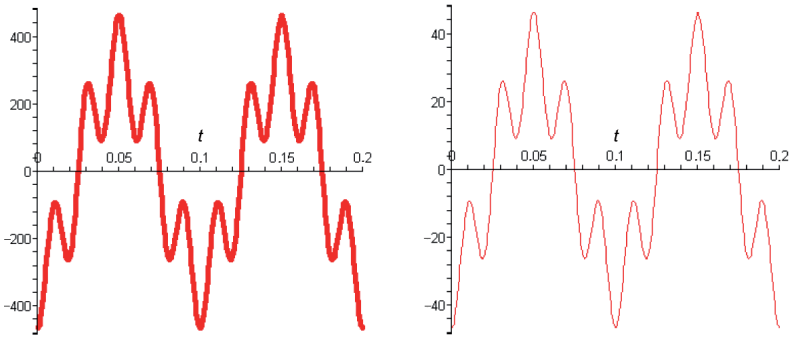

Fig. 1. Time histories of normal stress $\sigma_x(t)$ – left and shear stress $\tau_{xy}(t)$ – right

Table 1

Identified cycles for one block of the analyzed bi-axial and bi-modal stress histories

Number of cycles	Normal stress		Shear stress		Equivalent mean stress	Equivalent stress amplitude	Equivalent completely reversed uniaxial stress
	Mean	Amplitude	Mean	Amplitude			
1	0	465	0	46.5	0	471.9	471.9
1	176.5	85.3	17.7	8.5	176.5	86.6	120.7
1	278.1	186.9	27.8	18.7	278.1	189.7	341.7
1	–176.5	85.3	–17.7	8.5	–176.5	86.6	86.6
1	–278.1	186.9	–27.8	18.7	–278.1	189.7	189.7

3.2. Analysis of the multiaxial out-of-phase stress history

After P. Romanowicz and B. Szybiński [30], let us consider the interesting case when stress existing in a crane wheel, which is in contact with a rail, is of the multiaxial type, and the stress components are shifted in phase during contact. The shear stress $\tau_{yz}(t)$ are shifted in phase in comparison with the normal stress components $\sigma_x(t)$, $\sigma_y(t)$ and $\sigma_z(t)$ – see Fig. 2. The same effect can be observed for the ball bearings [29]. The direct spectral method can be applied for finding the equivalent completely reversed stress for the one stress block. By one stress block, the variation of stresses during one rotation of wheel is understood (Fig. 2). For one stress block, two cycles are identified:

– for maximal values of normal stresses ($x/a = 0$) – zero-to-tension;
– for maximal values of shear stresses ($x/a = 1$) – completely reversed.

The detailed values of stress components used for the identification of completely reversed stress by the direct spectral method are given in Table 2.

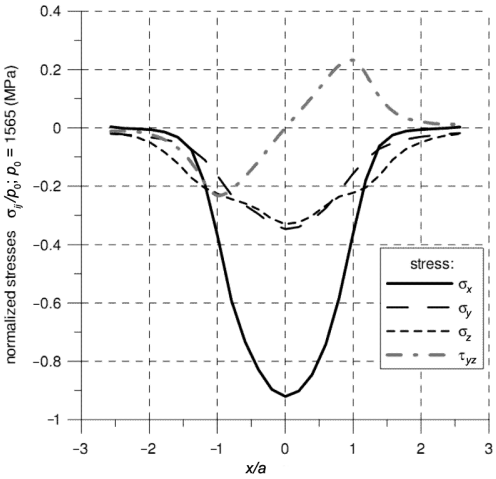

Fig. 2. Subsurface stress distribution on radius of Palmgren-Lundberg points for crane wheel; a – semi-axis of contact ellipse [30]

Table 2

Identified cycles for a crane wheel

Number of cycles	Normal stress [MPa]			Shear stress [MPa]			Equivalent mean stress [MPa]	Equivalent stress amplitude [MPa]	Equivalent completely reversed stress [MPa]
	Comp.	Mean	Ampl.	Comp.	Mean	Ampl.			
1	σ_x	–360	360	τ_{xy}	0	0	–618	231	231
	σ_y	–133	133	τ_{yz}	0	0			
	σ_z	–125	125	τ_{xz}	0	0			
1	σ_x	–579	0	τ_{xy}	0	0	–1158	651	651
	σ_y	–235	0	τ_{yz}	0	376			
	σ_z	–344	0	τ_{xz}	0	0			

The application of the other theories for the determination of the equivalent completely reversed stress leads to the values of equivalent completely reversed shear stress given in Tab. 3. After application of the von Mises relationship, the equivalent completely reversed normal stress given in Tab. 3 is estimated. The values estimated by the proposed direct spectral method are not far from those obtained by Papadopoulos 2, Crossland and energy methods, assuming that the ultimate stress for the material is equal to σ_u = 1250 MPa, and elasticity limit is equal to R_e = 1050 MPa.

Table 3

Comparison of equivalent completely reversed stress

Theory	Equivalent completely reversed shear stress [MPa]	Equivalent completely reversed (normal) stress [MPa]
Papadopoulos 1 [30]	471	816
Papadopoulos 2 [30]	373	646
Crossland [30]	386	669
energy [30]	376	651
direct spectral	–	651/231

4. Conclusions

Fatigue analysis of engineering problems, when stresses are of the multiaxial type, is not easy and there is no representative fatigue hypothesis to estimate it. Moreover, the results of analyses are different for the application some of theories.

The cases that were analyzed in this article make it possible to formulate the following conclusions:

- The direct spectral method seems to be an alternative approach for counting the stress cycles of the multiaxial type.
- The direct spectral method can be formulated for the cases when components of the stresses are in-phase or out-of phase.
- The natural applications of the direct spectral method in fatigue analysis are the cases of the single-modal (harmonic) and the bi-modal stress process in the frequency domain.

References

[1] Bathias C., Pineau A (Eds.), *Fatigue of materials and structures. Application to design and damage*, Wiley, Hoboken 2011.

[2] Benasciutti D., Tovo R., *On fatigue damage assessment in bimodal random process*, International Journal of Fatigue, Vol. 29, 2007, 232–244.

[3] Braccesi C., Cianetti F., Lori G., Pioli D., *Fatigue behaviour analysis of mechanical component subject to random bimodal stress process: frequency domain approach*, International Journal of Fatigue, Vol. 27, 2005, 335–345.

[4] Carpinteri D., Spagnoli A., *Multiaxial high-cycle fatigue criterion for hard metals*, International Journal of Fatigue, Vol. 23, 2001, 135–145.

[5] Dowling N.E., *Mechanical behaviour of materials. Engineering methods for deformations, fracture and fatigue*, Prentice-Hall International Editors Inc., Englewood Cliffs, 1993.

[6] Fu T.-T., Cebon D., *Predicting fatigue lifes for bi-modal stress spectral density*, International Journal of Fatigue 22, 2000, 11–21.
[7] Garud Y.S., *A multiaxial fatigue: a survey of the state-of-the-art*, Journal of Test Evaluation, Vol. 9, No. 3, 1981, 165–178.
[8] Gough H.J., Pollard H.V., *The strength of metals under combined alternating stress*, Proc. Inst. Mech. Eng., No. 131, 1935, 3–18.
[9] Kenmeugne B., Soh Fotsing B.D., Anago G.F., Fogue M., Robert J.-L., Kenne J.-P., *On the evolution and comparison of multiaxial fatigue criteria*, International Journal of Engineering and Technology, Vol. 4, No. 1, 2012, 37–46.
[10] Kocańda S., Szala J., *Podstawy obliczeń zmęczeniowych*, PWN, Warszawa 1997.
[11] Kozień M.S., Smolarski D., *Analytical simulation of application of FFT based spectral method of fatigue cycle counting for multiaxial stress on example of pulse excited beam*, Engineering Mechanics 19(5), 2012, 1–7.
[12] Kozień M.S., Smolarski D., *Formulation of the spectral direct method for cycle counting of bimodal multiaxial stress*, Book of Abstracts, 39th Solid Mechanics Conference SolMech (Eds. Kowalewski Z.L., Ranachowski Z., Widłaszewski J.), Warszawa–Zakopane 2014, 305–306.
[13] Kozień M.S., Smolarski D., *Formulation of a direct spectral method for counting of cycles for bi-modal stress history*, Solid State Phenomena, Vol. 224, 2015, 69–74, DOI: 10.4028/www.scientific.net/SSP.224.69.
[14] Kozień M.S., Szybiński B., *Method of estimation of life time for vibrating engineering structures with irregular time history response*, Proceedings of the 5th International Conference on Very High Cycle Fatigue, Berlin 2012, 539–544.
[15] Lee Y.-L., Barkey M.E., Kang H.-T., *Metal fatigue analysis handbook. Practical problem-solving techniques for computer-aided engineering*, Butterworth-Heinemann, Elsevier, Waltham, Oxford 2012.
[16] Ligaj B., *An analysis of the influence of cycle counting methods on fatigue life calculations of steel*, Scientific Problems of Machines Operation and Maintenance, Vol. 4 (168), 2011, 25–43.
[17] Liu Y., Mahadevan S., *Multiaxial high-cycle fatigue criterion and life prediction for metals*, International Journal of Fatigue, Vol. 27, 2005, 790–800.
[18] Łagoda T., *Energetyczne modele oceny trwałości zmęczeniowej materiałów konstrukcyjnych w warunkach jednoosiowych i wieloosiowych obciążeń losowych*, Studia i Monografie z. 76, Wyższa Szkoła Inżynierska w Opolu, Opole 1995.
[19] Łagoda T., Macha E., *Wieloosiowe zmęczenie losowe elementów maszyn i konstrukcji*, Studia i Monografie z. 121, Politechnika Opolska, Opole 2001.
[20] Macha E., *Modele matematyczne trwałości zmęczeniowej materiałów w warunkach losowego złożonego stanu naprężenia*, Prace Naukowe Instytutu Materiałoznawstwa i Mechaniki Technicznej Politechniki Wrocławskiej nr 41, Seria Monografie nr 13, Politechnika Wrocławska, Wrocław 1979.
[21] Matake T., *An explanation on fatigue limit under combined stress*, Bulletin of the Japan Society of Mechanical Engineering, Vol. 20, 1977, 257–263.
[22] McDiarmid D.L., *Fatigue under out-of-phase bending and torsion*, Fatigue Eng Mater Struct, Vol. 9, No. 6, 1987, 457–475.

[23] Niesłony A., *Wyznaczanie warstwic uszkodzeń zmęczeniowych metodą spektralną*, Studia i Monografie z.233, Politechnika Opolska, Opole 2008.
[24] Niesłony A., Macha E., *Wieloosiowe zmęczenie losowe elementów maszyn i konstrukcji Część V: Metoda spektralna,* Studia i Monografie z. 160, Politechnika Opolska, Opole 2004.
[25] Niesłony A., Macha E., *Spectral method in multiaxial random fatigue*, Springer, Berlin–Heidelberg, 2007.
[26] Papadopoulos I.V., Avoli P., Gorla C., Filippini M., Bernasconi A.A., *A comparitive study of multiaxial high-cycle fatigue criteria for metals*, International Journal of Fatigue, Vol. 19, No. 3, 1997, 219–235.
[27] Papadopoulos I.V., *Long life fatigue under multiaxial loading*, International Journal of Fatigue, Vol. 23, No. 10, 2001, 839–849.
[28] Romanowicz P., *Analiza zmęczeniowa wybranych elementów maszyn pracujących w warunkach kontaktu tocznego*, praca doktorska, Politechnika Krakowska, Kraków 2009.
[29] Romanowicz P., *Estimation of maximum fatigue loads and bearing life in ball bearings using multi-axial high-cycle fatigue criterion*, Applied Mechanics and Materials, Vol. 621, 2013, 157–170.
[30] Romanowicz P., Szybiński B., *Application of selected multiaxial high-cycle fatigue criteria to rolling contact problems*, Advanced Materials in Machine Design, Vol. 542, 2014, 95–100.
[31] Sines G., *Behaviour of metals under complex stresses*, [in:] Sines G., Waisman J.L. (Eds.), *Metal fatigue*, Mc-Graw-Hill, New York 1959, 145–169.
[32] Wang Y.Y., Yao W.X., *Evaluation and comparison of several multiaxial fatigue criteria*, International Journal of Fatigue, Vol. 26, No. 1, 2004, 17–25.
[33] You B.R., Lee S.B., *A critical review on multiaxial fatigue assessments of metals*, International Journal of Fatigue, Vol. 18, No. 4, 1996, 235–244.

TECHNICAL TRANSACTIONS | CZASOPISMO TECHNICZNE
MECHANICS | MECHANIKA
5-M/2016

DOI: 10.4467/2353737XCT.16.286.6118

STANISŁAW KRENICH*

CALCULATING GEOMETRIC PARAMETERS FOR INDUSTRIAL ROBOT GRIPPER MECHANISM ACCORDING TO THE ASSUMED FUNCTIONAL CHARACTERISTICS

WYZNACZANIE PARAMETRÓW GEOMETRYCZNYCH MECHANIZMU CHWYTAKA ROBOTA PRZEMYSŁOWEGO DLA ZAŁOŻONYCH CHARAKTERYSTYK FUNKCJONALNYCH

Abstract

The paper presents an approach to optimal synthesis of robot gripper mechanism. There are two different patterns of force and displacement functional characteristics applied. The first one deals with the assumed linear or nonlinear displacement of the gripper ends, whereas the second one takes under consideration the constant value or nonlinear chart of the gripping force. In order to generate the optimal solutions a gradient based method, a random search method and an evolutionary algorithm are used. The obtained results show relatively good effectiveness of the proposed optimization approach in comparison to conventional methods of synthesis of linkage mechanisms. The best solutions were generated by the evolutionary algorithm based method; worse by the random search algorithm. Gradient based method fails during optimization process and should not be used for such type of problems, especially described by trigonometric functions.

Keywords: industrial robots, linkage mechanism synthesis, design optimization, evolutionary algorithms

Streszczenie

W artykule przedstawiono metodę wyznaczania parametrów geometrycznych mechanizmu chwytaka dźwigniowego robota przemysłowego. Zastosowano syntezę mechanizmu dla założonych charakterystyk funkcjonalnych mechanizmu. Założono przebiegi liniowe i nieliniowe charakterystyki siłowej i przemieszczeniowej. W obliczeniach wykorzystano trzy algorytmy, gradientowy, losowy i ewolucyjny. Otrzymane wyniki wskazują, że proponowane podejście optymalizacyjne jest możliwe do zastosowania i stosunkowo efektywne w porównaniu z tradycyjnymi metodami syntezy mechanizmów, przy czym możliwe okazało się zastosowanie wyłącznie algorytmu ewolucyjnego generującego najlepsze rozwiązania w każdym przypadku oraz znacznie gorszego algorytmu losowego. Nie udało się w ogóle wygenerować rozwiązań algorytmem gradientowym, co wskazuje, że dla zadań optymalizacyjnych opisywanych funkcjami trygonometrycznymi tego typu algorytmy są zawodne i nie powinny być stosowane.

Słowa kluczowe: roboty przemysłowe, synteza mechanizmu dźwigniowego, optymalizacja konstrukcji, algorytmy ewolucyjne

* Ph.D. Eng. Stanisław Krenich, Institute of Production Engineering, Faculty of Mechanical Engineering, Cracow University of Technology.

1. Introduction

The design of many linkage mechanisms consist of two main steps. The first one is choosing a structure of the mechanism and the second one is calculating geometric parameters [3, 12–14]. These parameters are mainly linear or angular dimensions of mechanism, work ranges of movable parts, etc. The generation of geometric dimensions is implemented in order to obtain assumed motion parameters according to their functions and purposes, including kinematical and dynamical analysis. For kinematic analysis, there are graphical, analytical and numerical approaches used so far [15]. In fact, currently, these methods come down to numerical calculations of nonlinear equation systems. Numerical methods can be based on an iterative process of solving nonlinear equations, for example by Newton–Raphson algorithm [2]. This algorithm uses analytical or graphical dependences for position calculations of mechanism parts or their joints, and then uses the method of finite increments to generate their velocity and acceleration. The numerical approach may also include a method based on the use of an expansion of the function into the trigonometric Fourier series. Other approaches, quite often used for geometric synthesis, are optimization based methods. The problem of optimum design of different mechanisms has a quite long history. Most of these problems are modeled by means of nonlinear programming [1, 2, 5–7]. In many cases, calculation of these models by means of conventional optimization methods might give worse solutions or be difficult, or even impossible. Thus, in the last two decades, evolutionary algorithms (EAs) have become an effective tool to solve difficult optimization tasks, including continuous, discrete and mixed ones. Searching for optimal geometric parameters of gripper linkage mechanisms is an example of such a complicated task. Moreover, the optimization problem can have a multicriteria character in which several criteria are to be considered, so the EAs can also be used to obtain the full set of Pareto optimal solutions (non-dominated solutions) while single run of the EA. According to the advantages of EAs mentioned above, there is the possibility of using EAs firstly for parametrical optimization of different mechanism structures and then for finding the best structure of robot gripper mechanism. The problem of finding the best structure of mechanism is not considered in the paper. During the parametrical optimization, different traditional and heuristic algorithms are compared in order to find the best method for the described problem. In general, the optimization problem of robot gripper mechanism can be formulated as follows:
find:

$$\mathbf{x}^* = [x_1^*, x_2^*, ..., x_1^*] \tag{1}$$

which will satisfy the K inequality constraints and J equality constraints

$$g_k(\mathbf{x}^*) \geq 0, \text{ for } k = 1, 2, \ldots, K \tag{2}$$

$$h_j(\mathbf{x}^*) = 0, \text{ for } j = 1, 2, \ldots, J \tag{3}$$

and optimize the vector function:

$$\mathbf{f}(\mathbf{x}^*) = \min [f_1(\mathbf{x}), f_2(\mathbf{x}), ..., f_N(\mathbf{x})] \tag{4}$$

where: $\mathbf{x} = [x_1, x_2, ..., x_1]$ is the vector of decision variables, $\mathbf{f}(\mathbf{x}) = [f_1(\mathbf{x}), f_2(\mathbf{x}), ..., f_N(\mathbf{x})]$ is the vector of objective functions. Elements of vector $\mathbf{x}$ represent the dimensions of robot gripper elements, whereas the elements of vector $\mathbf{f}(\mathbf{x})$ represent the optimization criteria.

2. Problem formulation

The optimization problem is formulated as searching geometrical dimensions of the mechanism for the single criteria minimization of pattern deviation for the given force and displacement functional characteristics. The linkage mechanism is considered as an ideal one, with stiff elements and without friction forces in the joints.

2.1. Force and displacement dependences

Let us consider a gripper mechanism with the given kinematical structure as in Fig. 1. Force dependences are worked out for a static equilibrium for the whole range of mechanism movement.

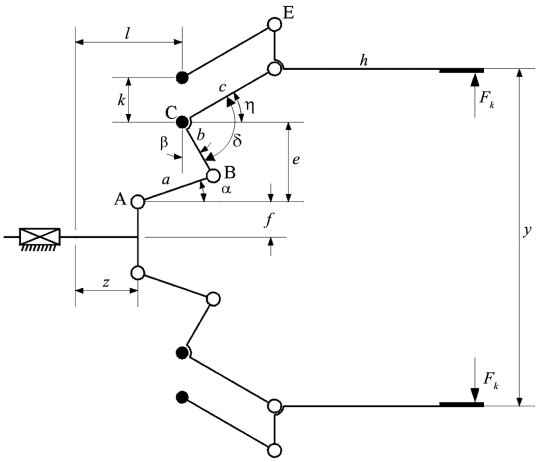

Fig. 1. Scheme of a robot gripper mechanism

The geometrical dependencies of the gripper mechanism are presented in Fig. 2 and evaluated as follows:

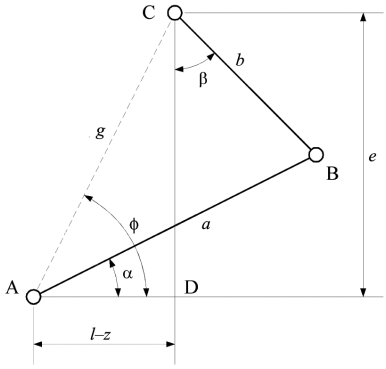

Fig. 2. Geometrical dependencies of the gripper mechanism

$$g = \sqrt{(l-z)^2 + e^2} \tag{5}$$

$$b^2 = a^2 + g^2 - 2 \cdot a \cdot g \cdot \cos(\phi - \alpha) \tag{6}$$

$$\alpha = \phi - \arccos\left(\frac{a^2 + g^2 - b^2}{2 \cdot a \cdot g}\right) \tag{7}$$

$$a^2 = b^2 + g^2 - 2 \cdot b \cdot g \cdot \cos\left(\beta + \frac{\pi}{2} - \phi\right) \tag{8}$$

$$\beta = \arccos\left(\frac{b^2 + g^2 - a^2}{2 \cdot b \cdot g}\right) + \phi - \frac{\pi}{2} \tag{9}$$

$$\phi = \arctan\left(\frac{e}{l-z}\right) \tag{10}$$

$$\eta = \beta + \delta - \frac{\pi}{2} \tag{11}$$

$$y(\mathbf{x}, z) = 2 \cdot (e + f + c \cdot \sin(\eta)) \tag{12}$$

The gripping force is calculated as follows:

$$F_k(P, \mathbf{x}, z) = \frac{P \cdot b \cdot \sin(\alpha + \beta) \cdot \cos(\eta)}{2 \cdot c \cdot \cos(\alpha)} \tag{13}$$

2.2. Optimization model of the gripper mechanism

For the given dependences the optimization model is presented below. The vector of decision variables is: $\mathbf{x} = [a, b, c, e, f, l, \delta]^T$, where a, b, c, e, f, l, are dimensions of the gripper and δ is the angle between the elements b and c.

The objective functions can be evaluated in general form as follows:

$$f_1(\mathbf{x}, z) = \int_z \left[y^{\text{assumed}}(z) - y(\mathbf{x}, z) \right]^2 \cdot dz \tag{14}$$

$$f_2(P, \mathbf{x}, y) = \int_y \left[F_k^{\text{assumed}}(y) - F_k(P, \mathbf{x}, y) \right]^2 \cdot dy \tag{15}$$

where:

- the functions $y^{\text{assumed}}(z)$ and $F_k^{\text{assumed}}(y)$ are respectively assumed displacement and force patterns of functional characteristics,
- $Z_{\min} \le z \le Z_{\max}$, $Y_{\min} \le y \le Y_{\max}$ are respectively lower and upper bounds of displacements z and y.

All the objective functions are to be minimized.

Note that objective functions depend on the vector of decision variables and on the displacement z. Thus, for the given vector x, the values of the functions have to be evaluated for different values of z, which makes the objective functions computationally expensive and the problem becomes more complicated than a general nonlinear programming problem. From the geometry of the gripper and based on the mechanism movement, the following constraints can be derived:

$$g_1(\mathbf{x}) = y(\mathbf{x}, z) \ge 0 \text{ for each } z, \text{ were } Z_{\min} \le z \le Z_{\max}, \tag{16}$$

$$g_2(\mathbf{x}) = \alpha + \frac{\pi}{2} \geq 0 \text{ for each } z, \text{ were } Z_{\min} \leq z \leq Z_{\max} \tag{17}$$

$$g_3(\mathbf{x}) = \frac{\pi}{2} - \alpha \geq 0 \text{ for each } z, \text{ were } Z_{\min} \leq z \leq Z_{\max} \tag{18}$$

$$g_4(\mathbf{x}) = \eta + \frac{\pi}{2} \geq 0 \text{ for each } z, \text{ were } Z_{\min} \leq z \leq Z_{\max} \tag{19}$$

$$g_5(\mathbf{x}) = \frac{\pi}{2} - \eta \geq 0 \text{ for each } z, \text{ were } Z_{\min} \leq z \leq Z_{\max} \tag{20}$$

$$h_1(\mathbf{x}) = z + a \cdot \cos(\alpha) - b \cdot \sin(\beta) - l = 0 \text{ for each } z, \text{ were } Z_{\min} \leq z \leq Z_{\max} \tag{21}$$

$$h_2(\mathbf{x}) = a \cdot \sin(\alpha) + b \cdot \cos(\beta) - e = 0 \text{ for each } z, \text{ were } Z_{\min} \leq z \leq Z_{\max} \tag{22}$$

3. Applied Methods of Solution

The problem was considered as continuous nonlinear programming problem. In order to generate optimal solutions, the following three different algorithms were applied:

- conjugate gradient algorithm (CGA) [6, 10],
- random search method (RSM) [6],
- evolutionary algorithm (EA) [7, 9].

The gradient based method is used with the very well known rules:

$$x^{t+1} = x^t + \alpha^t \nabla\phi(x^t) \tag{23}$$

where: α^t is the step length, $\nabla\phi(x^t)$ is the gradient of $\phi(x^t)$ at the point x^t and is given using the formula:

$$\phi(\mathbf{x}, r) = f(\mathbf{x}) + r\sum_{m=1}^{M}\left[h_m(\mathbf{x})\right]^2 + r\sum_{k=1}^{K} G_k\left[g_k(\mathbf{x})\right]^2 \tag{24}$$

where: G_k is the Heaviside operator such that $G_k = 0$ for $g_k(\mathbf{x}) \geq 0$ and $G_k = 1$ for $g_k(\mathbf{x}) < 0$, r is a positive multiplier, which controls the magnitude of the penalty terms.

The calculations for each run were carried out using several different starting points x^0, the step α^t and number of iterations were assumed automatically in order to achieve assumed accuracy equal to 0.000001, multiplier r =10 000.

As the random search method, the most common exploratory algorithm called Monte Carlo is used. In the method, a certain number of points is picked at random over the estimated range of all variables. This may be done formally by obtaining the randomly selected value x_i from the following formula:

$$x_i = x_i^l + \rho_i\left(x_i^u - x_i^l\right) \tag{25}$$

where:

x_i^l – the estimated lower bound of x_i,
x_i^u – the estimated upper bound of x_i,
ρ_i – a random number between zero and one.

For the above formula, there were 40 000 points generated and compared.

As the evolutionary algorithm, the tournament selection based one is used [7, 9]. It does not require calculation of the criterion and constraints functions in any situation, so calculations can significantly speed up. The principle of operation is as follows:

– If both solutions are outside of the feasible region, the one which is closer to this region is selected for the next generation. The values of the objective function are not calculated for either of the solutions.
– If one of the solutions is in the feasible region and another one is out of this region, the one which is in the feasible region is selected for the next generation. The values of the objective function are not calculated for either of the solutions.
– If both solutions are in the feasible region, the one with the better value of the fitness function is selected for the next generation.

Parameters for the evolutionary algorithm: crossover rate $R_C = 0.6$, mutation rate $R_M = 0.01$, population size $J = 100$, number of generations $T = 400$.

4. Results of optimization process

The optimization process was run using the following data:

– Side constraints:
  $0 \le a \le 100$, $0 \le b \le 100$, $10 \le c \le 100$, $0 \le e \le 100$, $0 \le f \le 100$, $0 \le l \le 100$, $0 \le \delta \le 3.14$.
– Additional parameters:
  actuator movement ranges $Z_{min} = 0$ mm, $Z_{max} = 50$ mm, actuator force $P = 100$ N.

The aim of the optimization was to find linear and angular dimensions of the linkage mechanism for the assumed force and displacement functional characteristics. The obtained results are presented in Table 1 to 4. The comparison between the assumed patterns of functional characteristics and charts given from generated optimal solutions are shown in Fig. 3 to 10. The comparison shows that there is a possibility to improve the parameters of the gripper mechanism using a suitable optimization procedure. Note that sequential methods failed during calculation, so they cannot be used for finding optimal gripper mechanisms. Random search method and evolutionary algorithm were used for the same number of function calls. For both methods, calculations took a few minutes.

Table 1

Generated optimal solutions for the assumed linear pattern of the ends displacement

Method	$f_1(\mathbf{x}, z)$	**a** [mm]	**b** [mm]	**c** [mm]	**e** [mm]	**f** [mm]	**l** [mm]	δ [rad]	**Constraints**
EA	53.68	36.49	46.82	65.01	65.16	0.02	51.91	0.80	satisfied
RSM	733.57	76.27	69.45	56.38	45.31	8.01	53.30	0.25	satisfied
CGA	–	–	–	–	–	–	–	–	failed

Table 2

Generated optimal solutions for the assumed nonlinear pattern of the ends displacement

Method	$f_1(\mathbf{x}, z)$	**a** [mm]	**b** [mm]	**c** [mm]	**e** [mm]	**f** [mm]	**l** [mm]	δ [rad]	**Constraints**
EA	1712.43	36.94	59.93	72.07	82.34	0.02	51.02	0.76	satisfied
RSM	4053.38	42.72	50.46	70.45	64.45	22.82	64.40	0.57	satisfied
CGA	–	–	–	–	–	–	–	–	failed

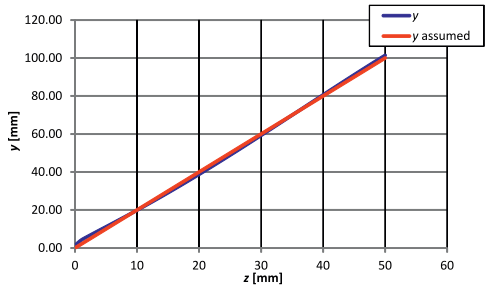

Fig. 3. Comparison of the displacement characteristics for the assumed linear pattern of the ends displacement (generated by EA)

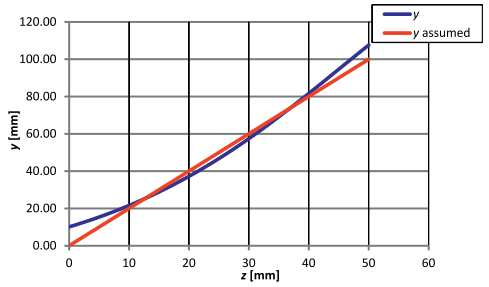

Fig. 4. Comparison of the displacement characteristics for the assumed linear pattern of the ends displacement (generated by RSM)

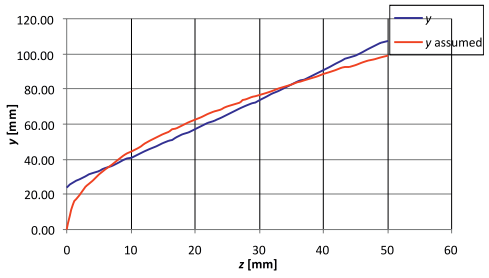

Fig. 5. Comparison of the displacement characteristics for the assumed nonlinear pattern of the ends displacement (generated by EA)

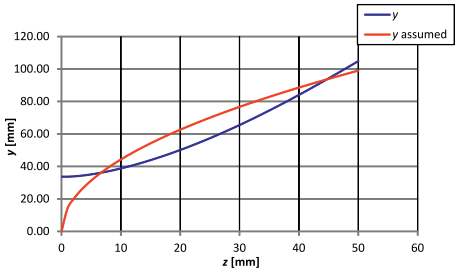

Fig. 6. Comparison of the displacement characteristics for the assumed nonlinear pattern of the ends displacement (generated by RSM)

Table 3

Generated optimal solutions for the assumed constant value of the gripping force

Method	$f_2(\mathbf{x}, z)$	**a** [mm]	**b** [mm]	**c** [mm]	**e** [mm]	**f** [mm]	**l** [mm]	δ [rad]	**Constraints**
EA	711.61	89.00	45.00	29.20	100.00	62.90	50.00	1.30	satisfied
RSM	7092.21	84.40	67.60	34.10	82.4	25.40	50.60	1.10	satisfied
CGA	–	–	–	–	–	–	–	–	failed

Table 4

Generated optimal solutions for the assumed nonlinear pattern of the gripping force

Method	$f_2(\mathbf{x}, z)$	**a** [mm]	**b** [mm]	**c** [mm]	**e** [mm]	**f** [mm]	**l** [mm]	δ [rad]	**Constraints**
EA	1928.61	89.60	100.00	10.00	65.80	57.10	50.70	0.50	satisfied
RSM	270690.01	53.90	52.70	10.60	74.50	48.50	50.50	0.80	satisfied
CGA	–	–	–	–	–	–	–	–	failed

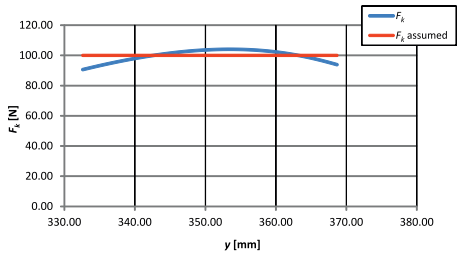

Fig. 7. Comparison of the force characteristics for the assumed constant value of the gripping force (generated by EA)

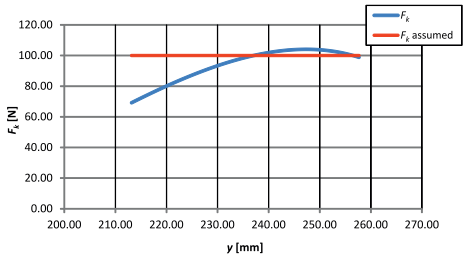

Fig. 8. Comparison of the force characteristics for the assumed constant value of the gripping force (generated by RSM)

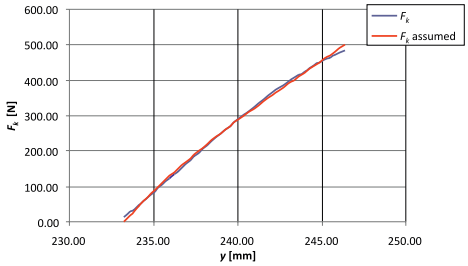

Fig. 9. Comparison of the force characteristics for the assumed nonlinear pattern of the gripping force (generated by EA)

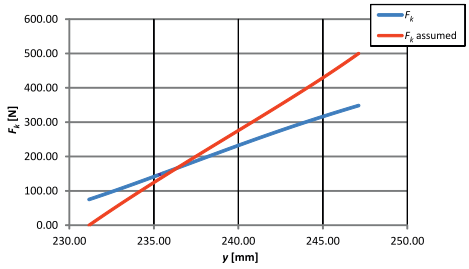

Fig. 10. Comparison of the force characteristics for the assumed nonlinear pattern of the gripping force (generated by RSM)

5. Summary

The experiments presented above indicate that the proposed optimization procedure can significantly improve functional parameters during the synthesis of the griper mechanism, especially the force and displacement characteristics. This approach has a universal character and can be used for different mechanisms. The obtained results show that conventional methods fail or give worse solutions. The conjugate gradient algorithm (CGA) was not able to generate any solution during all runs of the optimization procedure for several different starting points. The reason was a discontinuous type of the optimization model for fairly wide ranges of geometrical parameters. So, it yields that for parametrical

optimization of linkage mechanisms, the use of gradient based methods is very riskful or impossible. The random search method gave feasible solutions, but they were far from the best. It seems the most suitable method to solve such problems is an evolutionary algorithm. In addition, evolutionary algorithms allow considering a multicriteria parametrical optimization. Note that, for the given kinematical structure of the linkage mechanism, the applied optimization algorithms were not able to find the solution, which has got the ideal mapped patterns of functional characteristics. It means that for generating solutions with the functional characteristics similar to the patterns, different kinematical structures of the mechanism have to be considered.

References

[1] Chiara L., Ceccarelli M., *An Optimization Problem Algorithm for Kinematic Design of Mechanisms for Two-Finger Grippers*, The Open Mechanical Engineering Journal, Vol. 3, 19, 2009, 49–62.

[2] Kakatsios J.A, Tricamo S.J., *Integrated Kinematic and Dynamic Optimal Design of Flexible Planar Mechanisms*, Journal of Mechanisms, Transmissions and Automation in Design, Vol. 109, 1987, 338–347.

[3] Krenich S., Osyczka A., *Structural optimization of robot grippers using genetic algorithms*, The 20-th International Congress of Theoretical and Applied Mechanics-ICTAM, Paper CE3, Chicago 2000.

[4] Krenich S., *Optimal Design of Robot Gripper Mechanism Using Force and Displacement Transmission Ratio*, Applied Mechanics and Materials, Vol. 613, 2014, 117–125.

[5] Krenich S., *Multicriteria Design Optimization of Robot Gripper Mechanisms*, IUTAM Symposium on Evolutionary Methods in Mechanics, Kluwer Academic Publishers, Dordrecht–Boston–London 2004, 207–218.

[6] Osyczka A. *Evolutionary Algorithms for Single and Multicriteria Design Optimization*, Springer Physica-Verlag, Heilderberg, Berlin 2002.

[7] Osyczka A., Krenich S., *Evolutionary Algorithms for Global Optimization*, Chapter [in:] J. Pinter (Ed.), *Global Optimization – Selected Case Studies*, Kluwer Academic Publishers, 2007.

[8] Osyczka A., Krenich S., Karaś J., *Optimum design of robot gripers using Genetic Algorithms*, 3rd World Congress on Structural and Multidiscipilinary Optimization WCSMO, 17–22 May, Buffalo 1999, 241–243.

[9] Osyczka A., Krenich S., *A New Constraint Tournament Selection Method for Multicriteria Optimization Using Genetic Algorithm*, Proceedings of the Congress of Evolutionary Computing, San Diego 2000, 501–509.

[10] Pugh J.T., *Synthesis of Pareto Optimal Four-Bar Function Generators With Optimum Structural Error and Optimum Transmission Angles*, Journal of Mechanisms, Transmissions, and Automation in Design, Vol. 106, December 1984, 437–443.

[11] Rao S.S., *Multicriteria Optimization in Mechanisms*, Journal of Mechanical Design, Transaction of ASME, Vol. 101, 1984, 398–406.
[12] Rohatynski R., Klekiel T., *Some Application of Genetic Algorithm for Optimization of Four-bar Linkages*, Proceedings of Conference on Methods of Artificial Intelligence in Mechanics and Mechanical Engineering, Gliwice 2000, 285–290.
[13] Saravanan N., Ramabalan S., Ebenezer N.G.R., Dharmaraja C., *Evolutionary multicriteria design optimization of robot grippers*, Applied Soft Computing, Vol. 9, Issue 1, 2008, 159–172.
[14] Wang J.W., *Evolutionary algorithm based optimum design of mechanical gripper*, Coal Mine Machinery, Vol. 27, No. 10, China 2006.
[15] Xuyang C., Cleghorn W.L., *Parametric Optimization of Eight-bar an Mechanism of a Wheel Loader Based on Simulation*, Information Technology Journal 10 (9), 2011, 1801–1808.

TECHNICAL TRANSACTIONS | **CZASOPISMO TECHNICZNE**
MECHANICS | MECHANIKA
5-M/2016

DOI: 10.4467/2353737XCT.16.287.6119

JUSTYNA MIODOWSKA*, MAGDALENA KROMKA-SZYDEK*, JAN BIELSKI*,
MAGDALENA JĘDRUSIK-PAWŁOWSKA**

NUMERICAL ANALYSIS OF THE MANDIBULAR RECONSTRUCTION WITH THE USE OF AUTOGENOUS BONE GRAFT AND DENTAL IMPLANTS

ANALIZA NUMERYCZNA REKONSTRUKCJI ŻUCHWY PRZESZCZEPEM AUTOGENNYM Z WPROWADZONYMI IMPLANTAMI STOMATOLOGICZNYMI

Abstract

The article refers to some issues of the mandible reconstruction in the region of chin with the method involving dental implants introduced for teeth restoration. 12 models are created, which take into account three different graft materials (iliac crest, fibula and rib) and two various implant lengths (13 and 18 mm). The authors try to answer the question how the parameters of the introduced implants affect the distribution of the strain intensity in the mandible, both in the implantation area and at its border with autogenous graft. Also, the distribution of equivalent stress in the reconstruction plate and dental implants is analyzed.

Keywords: mandibular reconstruction, autogenous grafts, dental implants, FEA

Streszczenie

Praca dotyczy problematyki rekonstrukcji żuchwy w rejonie bródki z wykorzystaniem metody polegającej na wprowadzeniu implantów stomatologicznych pod odbudowę uzębienia. W artykule stworzono 12 modeli uwzględniających zastosowanie trzech różnych materiałów na przeszczep (kości biodrowej, strzałkowej i żebra) oraz dwie różne długości umieszczonych implantów (13 i 18 mm). Autorzy podjęli próbę odpowiedzi na pytanie, w jaki sposób parametry wprowadzonych implantów wpływają na rozkład intensywności odkształcenia w kości żuchwy w obszarze implantacji oraz na granicy z przeszczepem autogennym. Analizie poddano również rozkład naprężenia zredukowanego w płycie rekonstrukcyjnej oraz implantach stomatologicznych.

Słowa kluczowe: rekonstrukcja żuchwy, przeszczepy autogenne, implanty stomatologiczne, analiza MES

* M.Sc. Eng. Justyna Miodowska, Ph.D. Eng. Magdalena Kromka-Szydek, D.Sc. Ph.D. Eng. Jan Bielski, Institute of Applied Mechanics, Faculty of Mechanical Engineering, Cracow University of Technology.
** DDS Ph.D. Magdalena Jędrusik-Pawłowska, Medical University of Silesia.

1. Introduction

Partial resection of the mandible becomes a necessary surgery in the case of extensive cancerous changes or severe traumatic lesions. The lack of bone continuity results in the move of mandibular parts upwards and paracentrically due to the action of stomatognathic system muscles. This causes significant defects, both functional (speaking and chewing problems) and aesthetic (face deformation). Therefore, reconstruction using bone graft must be performed [8].

The reconstruction of the mandible is an extremely difficult task, and despite the existence of many surgical techniques, none of them have been described as the perfect clinical method [11]. Slooffa's studies on the graft healing process enabled the identification of factors affecting its quality and duration time. These are: stabilization of the recipient's bone graft, a vast contact area between the graft and the bone tissue of the recipient, regular blood supply around the transplant and mechanical strength of the graft enabling load transmission [28].

One of the most important clinical problems is the size of the removed part of the mandible together with its location. The worst condition for the reconstruction of mandibular defects are caused by cavities in a part of the chin, because excision of a fragment with the mouth front part and muscles causes displacement of the other parts of the mandible [15]. Filling the cavity in this part involves the reconstruction of both the continuity and the curvature of a bone [20]. At the same time, reconstruction of the large fragments of mandible reduces the possibility for subsequent full rehabilitation of the stomatognathic system. Therefore, the aim of the restorative surgery should be rebuilding the prosthetic base and intraosseous dental implants introduced for subsequent full teeth restoration. Bone graft must ensure sufficient width and height for the introduced implants of length appropriate in order to maintain the designed prosthesis during functional loading for a long time [6, 21, 24].

In present-day maxillofacial surgery, as the treatment of choice, autogenous grafts from the iliac crest stabilized with titanium, reconstructive plates are predominantly used. In the case of reconstruction of the chin part, free tibia graft is mostly preferred due to the possible extensive osteotomies, which ensure accurate formation and curvature of the graft [20]. The most common types of implants for restoration are intraosseous, either rotationally-symmetric or cylindrical, or various threads that are screw-shaped, directly connected with a bone subjected to functional load [13].

FEM analysis of stresses and strains distribution in the mandible and around implants placed in it is an important issue in dental engineering. In most published papers, only models of small bone sections with implants placed in it are analyzed [1, 14, 18, 22, 23, 29–32, 34, 35]. It does not allow for the assessment of stresses and strains in the mandible after the surgical removal of the bone part. The authors of those papers tried to evaluate the stress in implants and compare the values of selected strength indicators in the mandible with teeth and introduced dental implants. There are also numerical simulations, in which the entire (not reconstructed) mandible with implants was analyzed [2, 3, 5, 7, 10, 19, 33] and also models, which analyzed only the reconstructed mandible with the bone graft [12, 26, 27]. The inspiration for the creation of this paper was the lack of simulations for simultaneous mandibular reconstruction and implant dentistry.

2. Aim of the work

The aim of this paper is to evaluate how the parameters of the embedded dental implants affect the distribution of the strain intensity in bone and graft. A model of the mandible with autogenous graft and dental implants introduced for teeth restoration is created. The authors try to evaluate the conditions for possible bone union on the mandible-graft border under physiological load in the area of front teeth based on selected strength parameters. FEM analysis is applied to determine the necessary conditions in order to begin the bone remodeling process. The aim is achieved based on analysis of strain intensity distribution in the bone and the von Mises stress distribution in the dental implants.

3. Material and method

The numerical model of the mandible with the graft is created using FEMAP software and based on the clinical case in which the osteotomy lines were carried out in the region of the mental foramen, between the canine and the first molar. The finite element model of the mandible is created based on a specimen obtained post mortem. The mandible geometry is modeled with points which coordinates are measured in a coordinate system. The asymmetry of the removed bone is taken into account. Four cases of the mandible continuity restoration with three various autogenous grafts, as a block of bone taken from fibula, iliac crest and rib, are considered. The following cases relate to various dimensions of the implant (Tab. 1). A 13-hole 2,4 Synthes reconstruction plate and 10 UniLock screws are modeled.

Callus, formed in the process of healing, is modeled as a body with a thickness of 0.1 mm. Four titanium implants are introduced into the graft. The created spatial configuration corresponds to the restored incisors – ones and twos (31, 32, 41, 42[1]). The designed implant models are based on the shape and dimensions of a typical dental implant and simplified to truncated cones as shown in Fig. 1. Additionally, at the top of each implant, a ceramic element is created for a prosthetic superstructure. Fully bonded interfaces are assumed between the bone and implant, simulating complete osseointegration. The dimensions of the dental implant are given in Table 1.

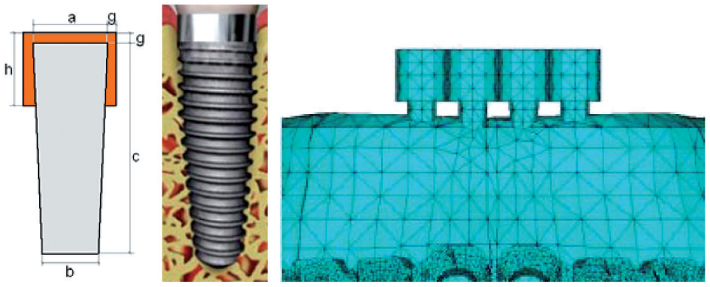

Fig. 1. Shape and dimensions of the implant and its FE model

[1] Viohl's dental notation.

The model is meshed using 10-node solid tetrahedral elements in Ansys. The final model, depending on the case, comprises approximately 64 000 elements (DOF 120 000).

Table 1

Dimensions of the implants

Case	Dimensions [mm]				
	a	b	c	g	h
I	3.0	2.5	18	1	5
II			13		
III	4.5	4.0	18		
IV			13		

The load scheme assuming the muscles action is adopted as the closest to the physiological conditions of stomatognathic system work. The load scheme is modeled on the following assumptions:

– the actions of four muscles are considered, i.e., the temporal (T), masseter (M), medial (MP) and lateral pterygoid (LP) muscles (Fig. 2);
– forces are applied at the site of muscle insertion, consistently with the size of the respective insertion area; directions of forces are based on literature data [27];
– the load model includes typical, physiological bite forces;
– simplified temporomandibular joint, composed of the articular disc and temporal bone fragment, is modeled.

As a result of the adopted scheme load (biting on the front teeth), the applied constraints involve the blockage of translational movements in all directions. The constraints are applied on the upper surfaces of the modeled, simplified temporomandibular joints and titanium implants placed into the bone graft (Fig. 2).

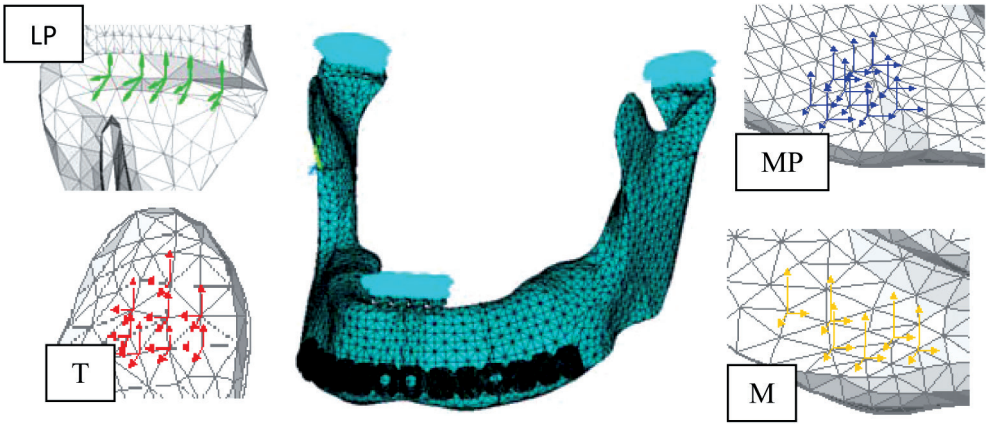

Fig. 2. The model of the mandible with forces and constraints applied

The total value of force applied by the muscles is assumed as 100 N, which is in the range adopted by other authors: 50÷150 N [2, 3, 19, 27]. The use of different bone materials is modeled by changing the material constants as shown in Tab. 2. The mandible is assumed to be a homogenous, isotropic and linearly elastic material. Such an approximation is based on the fact that strain-stress analysis not only takes into account the bone structure, but also the mandible-plate reconstruction-dental implant scheme (the latter two ar isotropic materials). Also, in the case of the mandible, the orthotropy ratio is smaller than that for the long bones, which approaches mandible structure to isotropic material [25]. The trabecular structure of the bone is not included. This approach is motivated by the fact that the mandible is composed mostly of a cortical structure, which, according to literature [9], may account for up to 79–89% of the entire bone. It is assumed that the bone strength corresponds to the compact bone tissue (cortical bone). Hence, it is assumed that the model of the mandible is made entirely of isotropic material (cortical bone), and the resulting stress distribution depends on the geometry of the mandible. At the same time, used for further analysis, H-M-H hypothesis refers to isotropic materials. The simulations are performed for the Young modulus of the callus equal to 200 MPa, which corresponds to the final stage of the bone healing process (after approx. 6–8 weeks). Changes in the tissue of the mandible, graft, reconstructive plate and implants induced by physiological load are evaluated on the basis of selected strength parameters, i.e. strain intensity and equivalent stress.

Table 2

Material constants used in analyses

Material	Young modulus E [MPa]	Poisson ratio ν	References
mandible	18000	0.32	[17]
graft			[16]
iliac crest	8000	0.35	[16]
rib	11500	0.30	[16]
fibula	21100	0.30	[16]
callus	200	0.40	[17]
articular disc	50	0.45	[5]
temporal bone	15000	0.32	[5]
reconstruction plate (Ti-6Al-7Nb)	108000	0.30	[25]
screws (Ti-6Al-7Nb)	108000	0.30	[25]
dental implants (Ti-6Al-4V)	110000	0.30	[25]
ceramic (ZrO_2)	210000	0.19	[25]

4. Results

The results of the analyses are presented in the form of a bar graph and stress/strain maps. The exertion of the reconstruction plate is described by the values of reduced stress calculated according to the Huber-Mises-Hencky hypothesis σ_{HMH} MPa. Stress analysis enables the assessment of the relationship between the occlusal load and stress distribution in the implants. The exertion of mandibular hard tissues and autogenous grafts is determined based on the values of the strain intensity ε_{int}. Changes in strain values are the most important factors, which stimulate adaptive responses of the bone tissue, associated with mechanical deformation field [25]. The interaction between the implant and the graft is evaluated. The implant thread is not modelled because of the lack of the trabecular structure. Also, the analysis is carried out for complete osseointegration when the movement between the bone and the implant can be neglected. The authors try to determine the extent to which physiological load affects the response of bone tissue at various geometrical parameters of implants. The more detailed model of the thread would be significant if the process of the osseointegration was the main aim of the analysis. Here, it is assumed that the osseointegration is completed.

The analyses are carried out for left (LOL) and right (ROL) osteotomy lines between the mandible and graft and in the region of titanium implants' contact with the transplant because these are the areas where processes of failure or overloading of bone tissue are observed.

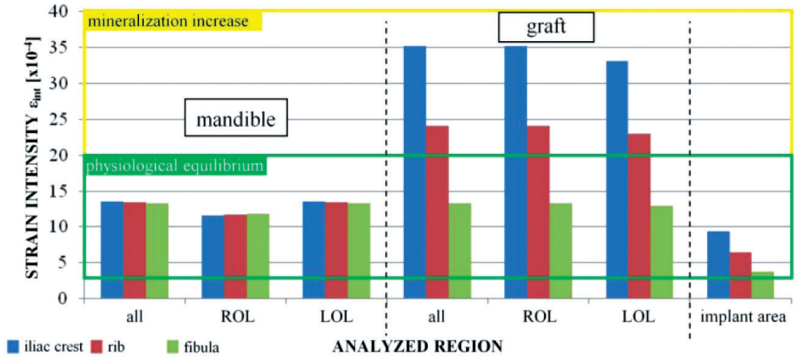

Fig. 3. The maximum value of the strain intensity in the mandible, graft and around implants depending on the type of autogenous graft in the case I

In all four cases, both for the entire mandible and on the border with the graft (left and right osteotomy line), the maximum strain intensity values in the mandible are observed in the range of physiological equilibrium ($2 \div 20 \times 10^{-4}$). Depending on the particular case (Table 1) and the material used for reconstruction, the ε_{int} differences are approx. 8%. For case I, the region of highest exertion of the mandible is located in the left osteotomy line (Fig. 3), while in other cases, it is met in the area of the right line osteotomy. However, the values of the strain intensity remain on a similar level in all regions. The strain intensity values are

within the range of physiological equilibrium only in the case of using transplant material obtained from the fibula. For the other bone materials, ε_{int} reaches the values corresponding to the mineralization increase ($20 \div 40 \times 10^{-4}$). The region of the greatest exertion in the graft is located in the area near the right osteotomy line in case I, independently of the bone graft material, and in cases II, III and IV in which the material obtained from the fibula is used for reconstruction. In contrary, in other cases, the maximum value of ε_{int} is located in the region of the hole closer to the LOL, where the fixing screw is placed (Fig. 4).

The region of the greatest exertion in the graft-implant area is located near tooth 31 or 41, regardless of the geometry of the used implant and graft material. Thus, these parameters have no effect on the ε_{int} maximum values and the exertion region in the bone.

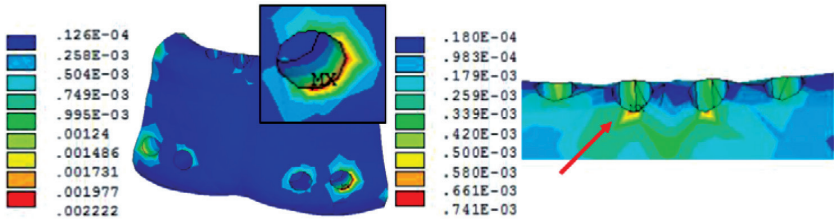

Fig. 4. ε_{int} distribution in graft tissue and at the bone-implant border for the case II with a bone material obtained from the rib

The stress concentration in the reconstruction plate is located near the border between the mandible and graft (LLO) at the point of contact with the screw. In the cases when implants with top diameter of 3.0 mm are used, the region of greatest exertion in the reconstruction plate is located on the side of the mandible (Fig. 5), whereas for implants with top diameter of 4.5 mm – on the side of the graft. The maximum values of the equivalent stress are in the range of 138–175.8 MPa. Such values remain below the yield strength for the titanium alloy and do not cause destruction of the plate.

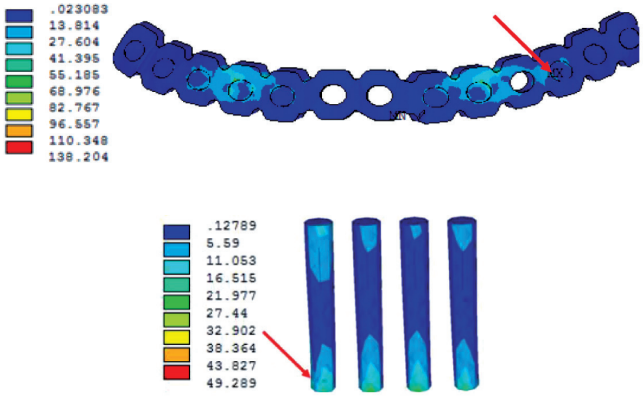

Fig. 5. Equivalent stress distribution in the reconstruction plate and dental implants in case I with iliac crest graft used for transplantation (front view)

The maximum stress value in implants occurs in the same place (area of the tooth 42 in the lower part of the tongue side) for all cases, regardless of the geometry of the implant and the type of bone material used for transplantation. Introduction of implants with top diameter of 4.5 mm (case III and IV) results in an almost double increase of the maximum stress value in the implant in relation to case I and II (Tab. 3). Although, it does not affect the qualitative distribution of the equivalent stress.

Table 3

The maximum equivalent stress σ_{HMH} in reconstruction plates and implants depending on the autogenous graft type

	Case I	**Case II**	**Case III**	**Case IV**
	Reconstruction plate – maximum equivalent stress σ_{HMH} [MPa]			
iliac crest	138.2	138.8	148.8	153.7
fibula	142.1	138.0	170.0	175.8
rib	141.2	138.7	144.3	138.1
	Dental implants – maximum equivalent stress σ_{HMH} [MPa]			
iliac crest	49.3	40.2	81.2	104.4
fibula	48.3	38.2	72.1	92.3
rib	45.5	33.9	74.7	83.6

5. Conclusions

Biomechanical analysis of the mandible-graft-reconstructive plate allows for the assessment of the treatment in terms of the proper work of the reconstructed stomatognathic system. Based on numerical simulations, it is possible to determine the necessary conditions for the initiation of the healing process and to analyze the mandible remodeling during healing. The usage of free bone grafts allows dental implants' introduction for the purpose of prosthetic rehabilitation. It enables early dental implants' partial loading, which can cause perigraft bone structures targeted layering.

The analysis showed that the type of bone material used for the reconstruction has an impact on the strain observed at the border of the mandible-graft and in the area between dental implants and the graft. The highest values of the strain intensity (ε_{int}) are observed for material taken from the iliac crest.

The geometrical dimensions of the implants have no significant impact on the value of ε_{int} in the mandible – with a load of 100 N, it remains in the range of physiological equilibrium. According to the hypothesis of a mechanical stimulator of bone tissue remodeling process, the range of values for a physiological equilibrium is $2 \div 20$ [$\times 10^{-4}$] [25].

Increasing the implants' diameter does not significantly affect the equivalent stress distribution in the implant, although it causes almost double increase of its maximum value, but does not exceed the yield strength value for titanium alloy. The differences in the materials used as graft and implant dimensions have no significant impact on the value of the maximum stress in the reconstruction plate in cases I and II (the difference does not exceed 2%). In cases III and IV, where fibula graft is used for reconstruction, the obtained equivalent stress σ_{HMH} values are higher by approx. 12% for longer dental implants (18 mm) and 21% for the shorter (13 mm), compared to other graft materials. However, according to other authors, fibula graft creates favorable conditions for the maintenance of intraosseous dental implants and subsequent prosthetic rehabilitation based on implants' introduction [24].

References

[1] Baggi L., Cappelloni I., Maceri F., Vairo G., *Stress-based performance evaluation of osseointegrated dental implants by finite-element simulation*, Simulation Modelling Practice and Theory 16, 2008, 971–987.

[2] Barao V.A.R., Delben J.A., Lima J., Cabral T., Assuncao W.G., *Comparison of different designs of implant-retained overdentures and fixed full-arch implant-supported prosthesis on stress distribution in edentulous mandible – A computed tomography-based three-dimensional finite element analysis*, Journal of Biomechanics 46, 2013, 1312–1320.

[3] Bonnet A.S., Postaire M., Lipinski P., *Biomechanical study of mandible bone supporting a four-implant retained bridge. Finite element analysis of the influence of bone anisotropy and foodstuff position*, Medical Engineering & Physics 31, 2009, 806–815.

[4] Chladek W., Czerwnik I., Kosiewicz J., *Własności mechaniczne krążka stawowego stawu skroniowo-żuchwowego*, AnnalAcadMedSilesiensis , supl.46, Katowice 2002, str. 188–193.

[5] Correa S., Ivancik J., Isaza J.F., Naranjo M., *Evaluation of the structural behavior of three and four implant-supported fixed prosthetic restorations by finite element analysis*, Journal of Prosthodontic Research 56, 2012, 110–119.

[6] Curtis D.A., Plesh O., Miller A.J., Curtis T.A., Sharma A., Schweitser R., Hilsinger R.L., Shour L., Singer M., *A comparison of masticatory function in patients with or without reconstruction of the mandible*, Head&Neck 1997, 7, 287–296.

[7] Daas M., Dubois G., Bonnet A.S., Lipinski P., Rignon-Bret C., *A complete finite element model of a mandibular implant-retained overdenture with two implants: Comparison between rigid and resilient attachment configurations*, Medical Engineering & Physics 30, 2008, 218–225.

[8] Dąbrowski J., Przybysz J., Piętka T., Domański W., *Tytanowe płyty rekonstrukcyjne w odtwarzaniu ciągłości żuchwy*, Czasopismo Stomatologiczne, 2010, 63, 663–671.

[9] Drozdzowska B., Michno M., Michno A., *Związek masy kostnej żuchwy ze stanem mineralizacji szkieletu na podstawie piśmiennictwa*, Nowa Stomatologia, zeszyt 21 (3/2002).
[10] Ferreira M.B., et al. *Non-linear 3D finite element analysis of full-arch implant-supported fixed dentures*, Materials Science and Engineering C 38, 2014, 306–314.
[11] Hilger P.A., Adams G., *Mandibular Reconstruction with the A-O Plate*, Arch Otolaryngology, 111, 1985, 469–471.
[12] Jędrusik-Pawłowska M., Kromka-Szydek M., *Mandibular reconstruction – biomechanical strength analysis (FEM) based on a retrospective clinical analysis of selected patients*, Acta of Bioengineering and Biomechanics, Vol. 15, No. 2, 2013, 23–31.
[13] Koeck B., Wagner W., *Implantologia*, Wyd. Medyczne Urban & Partner, Wrocław 2004.
[14] Kong L., Zhao Y., *Selection of the implant thread pitch for optimal biomechanical properties: A three-dimensional finite element analysis*, Advances in Engin. Software 40, 2009, 474–478.
[15] Kowalczyk R., Kowalik S., *Rekonstrukcja żuchwy w materiale Kliniki Chirurgii Szczękowo-Twarzowej PAM w Szczecinie*, Czasopismo Stomatologiczne, 2002, LV, 3.
[16] Kromka M., *Analiza wytrzymałościowa osteosyntezy mini- i makropłytkowej urazów żuchwy*, Rozprawa doktorska, Kraków, 2005, 169–176.
[17] Kromka-Szydek M., Jędrusik-Pawłowska M., Milewski G., Lekston Z., Cieślik T., Drugacz J., *Numerical analysis of displacements of mandible bone parts using various elements for fixation of subcondylar fractures,* Acta of Bioeng. and Biomechanics, Vol. 12, No. 1, 2010, 11–18.
[18] Lin D., Li Q., Li W., Duckmanton N., Swain M., *Mandibular bone remodeling induced by dental implant*, Journal of Biomechanics 43, 2010, 287–293.
[19] Liu J. et al., *Influence of implant number on the biomechanical behavior of mandibular implant-retained/supported overdentures: A three-dimensional finite element analysis*, Journal of Dentistry 41, 2013, 241–249.
[20] Maciejewski A., Szymczyk C., Wierzgoń J., Półtorak S., *Techniki mikrochirurgiczne w rekonstrukcji poresekcyjnych ubytków żuchwy – propozycja algorytmu*, Czasopismo Stomatologiczne, LVIII, 7, 2005, 505–513.
[21] Marunick M.T. et al., *Functional criteria for mandibular implant placement post resection and reconstruction for cancer*, J. Prosthet. Dent., 1999, 82, 107–113.
[22] Merdji A., Bouiadjra B.B., Achour T., Serier B., Ould Chick B., Feng Z.O., *Stress analysis in dental prosthesis*, Computational Materials Science 49, 2010, 126–133.
[23] Meric G., Erkmen E., Kurt A., Tunc Y., Eser A., *Influence of prosthesis type and material on the stress distribution in bone around implants: A 3-dimensional finite element analysis*, Journal of Dental Sciences 6, 2011, 25–32.
[24] Mierzwińska-Nastalska E., Rolski D., Gładkowski J., Łomżyński Ł., Kostrzewa-Janicka J., Mateńsko D., Ciechowicz K., Starościak S., Jaworowski J. *Rehabilitacja implantoprotetyczna pacjentów po resekcji żuchwy i rekonstrukcji z zastosowaniem unaczynionych płatów z kości strzałki*, Protetyka Stomatologiczna, LX, 3, 2010, 182–193.

[25] Milewski G., Kromka-Szydek M., *Podstawy biomechaniki stomatologicznej*, Politechnika Krakowska, Kraków 2010.
[26] Milewski G., Tracz M., *Numerical strength simulation of mandibular osteosynthesis by means of autogenous bone graft*, Acta of Bioengineering and Biomechanics, Vol. 2, No. 2, 2000, 59–65.
[27] Nagasao T., Miyamoto J., Tamaki T., Kawana H., *A comparison of stresses in implantation for grafted and plate-andscrew mandible reconstruction*, Oral Surg. Oral Med. Oral Pathol. Oral Radiol. Endod., Vol. 109(3), 2010, 346–356.
[28] Płomiński J., Kwiatkowski K., *Przeszczepy kostne*. Pol. Merk. Lek., 2006, XXI (126), 507–510.
[29] Santiago J.F., Pellizzer E.P., Verri F.R., de Carvalho P.S., *Stress analysis in bone tissue around single implants with different diameters and veneering materials: A 3-D finite element study*, Materials Science and Engineering C 33, 2013, 4700–4714.
[30] Schwitalla A.D. et al., *Finite element analysis of the biomechanical effects of PEEK dental implants on the peri-implant bone*, Journal of Biomechanics 48, 2015, 1–7.
[31] Simsek B., Erkmen E., Yilmaz D., Eser A., *Effects of different inter-implant distances on the stress distribution around endosseous implants in posterior mandible: A 3D finite element analysis*, Medical Engineering & Physics 28, 2006, 199–213.
[32] Takahashi T., Shimamura I., Sakuraiu K., *Influence of number and inclination angle of implants on stress distribution in mandibular cortical bone with All-on-4 Concept*, Journal of Prosthodontic Research 54, 2010, 179–184.
[33] Topkaya T., Solmaz M.Y., *The effect of implant number and position on the stress behavior of mandibular implant retained overdentures: A three-dimensional finite element analysis*, Journal of Biomechanics 48, 2015, 2102–2109.
[34] Wang C., Fu G., Deng F., *Difference of natural teeth and implant-supported restoration: A comparison of bone remodeling simulations*, Journal of Dental Sciences 10, 2015, 190–200.
[35] Yang Y., Xiang H.-J., *A three-dimensional finite element study on the biomechanical behavior of an FGBM dental implant in surrounding bone*, J Biomech 40, 2007, 2377–2385.

TECHNICAL TRANSACTIONS | CZASOPISMO TECHNICZNE
MECHANICS | MECHANIKA
5-M/2016

DOI: 10.4467/2353737XCT.16.288.6120

ARTUR OLSZAK*, ELŻBIETA ZIĄBSKA**, KAROL OSOWSKI**
ANDRZEJ KĘSY**, ZBIGNIEW KĘSY**

DURABILITY OF HYDRAULIC CLUTCHES FILLED WITH ELECTRORHEOLOGICAL FLUIDS

TRWAŁOŚĆ SPRZĘGIEŁ HYDRAULICZNYCH Z CIECZAMI ELEKTROREOLOGICZNYMI

Abstract

The paper presents the results of experimental tests concerning the durability of two devices, using three different electrorheological fluids as working fluids. They were: a cylinder viscous brake and a dual clutch, consisting of a cylinder viscous clutch and a hydrokinetic clutch. The concept of the control of devices filled with electrorheological working fluids involves the impact of the electric field of variable intensity on the working fluid and thus causes changes of sheer stress in it. It also changes the transmitted torque. The studies show that the most important factors affecting the durability of a viscous brake and a dual clutch are: sealing of the workspace, including the electrorheological fluid, electrorheological fluid type, electrodes and electrical wire insulation, supplying high voltage from the power supply. Another essential factor is that the durability of the electrorheological fluid, defined by the rate of wear, is found within the ranges reported in the literature and does not differ significantly from the magnetorheological fluid durability.

Keywords: Durability, viscous clutches and brakes, hydrokinetic clutches, adaptive fluids

Streszczenie

W artykule przedstawiono wyniki badań eksperymentalnych trwałości dwóch urządzeń, w których zastosowano trzy różne ciecze elektroreologiczne jako ciecze robocze. Były to: wiskotyczny hamulec cylindryczny oraz sprzęgło zespolone, składające się z wiskotycznego sprzęgła cylindrycznego i sprzęgła hydrokinetycznego. Koncepcja sterowania urządzeń z elektroreologicznymi cieczami roboczymi polega na oddziaływaniu polem elektrycznym o zmiennym natężeniu na ciecz roboczą i wywoływaniu w ten sposób zmian naprężeń stycznych w cieczy roboczej, a tym samym zmian przenoszonego momentu obrotowego.Z przeprowadzonych badań wynika, że najistotniejszymi czynnikami wpływającymi na trwałość hamulca wiskotycznego i sprzęgła zespolonego są: uszczelnienie przestrzeni roboczej, w której znajduje się ciecz elektroreologiczna, rodzaj cieczy elektroreologicznej, izolacja elektrod i przewodów elektrycznych, doprowadzających wysokie napięcie z zasilacza oraz że trwałość cieczy elektroreologicznych, zdefiniowana za pomocą stopnia zużycia, mieści się w zakresach podawanych w literaturze. Ponadto nie odbiega znacznie od trwałości cieczy magnetoreologicznych.

Słowa kluczowe: trwałość, sprzęgła i hamulce wiskotyczne, sprzęgła hydrokinetyczne, ciecze adaptacyjne

* Ph.D. Eng. Artur Olszak, New Chemical Syntheses Institute, Puławy.
** M.Sc. Elżbieta Ziąbska, Ph.D. Karol Osowski, Prof. Ph.D. Eng. Andrzej Kęsy, Prof. Ph.D. Eng. Zbigniew Kęsy, Institute of Applied Mechanics and Energetics, Faculty of Mechanical Engineering, Kazimierz Pulaski University of Technology and Humanities in Radom.

1. Introduction

Currently, the main direction of research and development concerning machine drive systems is to improve the design of their components, such as clutches, brakes or gears. The application of new hydraulic fluids causes the progress of clutches and brakes. Due to the issue of increasing demands concerning drive units, which is connected with the increase of machine efficiency, new components must be very durable. The durability is defined as the machine's ability to preserve the functionality in the required conditions of its use. The device durability has an essential impact on its reliability.

Hydraulic clutches consist of a driving part, combined with an input shaft, a driven part, connected to the output shaft, and a working fluid. There are two basic types of clutches: viscous and hydrodynamic ones. In viscous clutches, driving and driven parts are connected together due to the friction caused by shear stresses τ in the working fluid, while in the hydrokinetic clutches, the torque is transmitted from the pump impeller to the turbine impeller, using the kinetic energy of the working fluid.

Due to the workspace shape, the following can be distinguished: viscous couplings – cylindrical and disc clutches and hydrodynamic ones, including or not including the inner ring. By immobilizing the driven part of the hydraulic clutch, it can be converted into a hydraulic brake.

Working fluids called adaptive fluids or smart fluids, in which the shear stress can be changed by means of an electric current [1, 2], are used in hydraulic clutches and brakes. They are: electrorheological fluids that are activated with the electric field and magnetorheological fluids activated with the magnetic field. The concept of hydraulic clutch control filled with these fluids is based on the interaction of the electric or magnetic field of variable intensity on the working fluid and thus inducing shear stress changes in the working fluid and consequently changes of the transmitted torque [3, 4].

Considering the composition, both electrorheological and magnetorheological fluids are divided into heterogeneous fluids, consisting of a solid phase and a liquid phase and a homogeneous fluids. Heterogeneous fluids are mostly used in hydraulic clutches. The solid phase in this type of fluid is present from 20% to 80%, and from 5% to 50% as far as volume is concerned. The increase in shear stress in heterogeneous fluids, when being influenced by electric or magnetic fields, is caused by the creation of spatial structures hindering the flow of the mixture.

Solid particles of heterogeneous adaptive fluids are about a few micrometers in diameter and are made (in case of electrorheological fluids) of materials that are polarized when influenced by an electric field. They can also be made of inorganic materials (metal oxides, zeolites, glass) or organic ones (starch, resins, rubber, polyaniline, polyphenylene). In the case of magnetorheological fluids, they are made of materials with ferromagnetic properties [5–8]. A non-conductive liquid, typically oil or silicone oil, is used as a liquid phase. These fluids also contain various types of additives modifying their properties (water, inorganic salts, acids, alcohols, esters). These additives prevent particle sedimentation and combination so that they can be used in a wide range of temperatures and with considerable accelerations.

In viscous clutches and brakes including electrorheological fluids, in order to generate an electric field, electrodes, which are also elements of driving and driven parts of the

clutch, are used. On the contrary, to induce a magnetic field in the clutches and brakes of magnetorheological fluids, it is necessary to use additional electromagnets. For these reasons, clutches and brakes including electrorheological fluids have a much simpler construction. The disadvantage of these clutches and brakes are their bigger dimensions in comparison with clutches and brakes including magnetorheological fluids, resulting from the fact that the maximum shear stress, possible to obtain during the activation, is several times greater in magnetorheological fluids than in electrorheological fluids. It is possible to obtain the range of shear stress changes, which can be influenced by means of an electric current through the formation of one of the physical fields. It allows for over one hundred times more precise and continuous variation of the torque transmitted by viscous clutches or brakes.

Up till now, a number of clutches and brakes using electrorheological or magnetorheological fluids as working fluids [9–13] have been developed and tested. However, in mass-produced machines, these clutches are rarely used [14]. For this reason, there are no experiments connected with the durability of such clutches and brakes.

2. Review of literature concerning the durability of equipment including adaptive fluids

Previous studies concerning the durability of devices filled with adaptive fluids have concentrated mainly on studying clutches and dampers, referring to the fluid durability, whole devices or their components.

The authors of the publication [15] suggest two reasons for the electrorheological fluid degradation: high operating temperature and the phenomenon of electrolysis, caused by the flow of the electric current through the liquid. During the process of electrolysis, chemical reactions may occur, resulting in the decomposition of water, and oxidation or reduction of the material, of which adaptive fluid particles are made. The corrosion of the electrode material might also occur. As it is seen from the example given in the publication, the water content of the electrorheological fluid sample may be reduced up to 1% when the current flow is 10 mA for 600 hours. The change of the electrorheological fluid property can also be caused by the degradation of inorganic salt particles added to electrorheological fluids in order to improve their electrical conductivity. In this case, a decrease of shear stress τ in the electrorheological fluid can be noticed. For the fluid consisting of polymer particles and silicone oil, the shear stress decrease may be τ approx. 40% when the current flow is 50 μA for 3 hours.

In the paper [16], the impact of the temperature on the shear stress τ in the newly developed electrorheological fluid, consisting of polyurethane particles and silicone oil, has been studied by means of reometer, which has a special construction. It was found that the detention of the liquid for 1000 hours at a temperature below 60°C does not change the shear stress value, but instead raises the temperature to:

– 100°C decreased the value of shear stress by 50% after 100 hours,
– 120°C decreased the value of shear stress by 40% after 4 hours.

On the basis of the durability of the linear damper including the magnetorheological fluid, it has been found that the first sign of the magnetorheological fluid wear is the value

increase of the coefficient of dynamic viscosity in time, due to the particle disintegration [17]. Moreover, it has been established that the destruction of even a small number of solid particles causes a significant increase in the coefficient of dynamic viscosity. The problem of the low durability of particles has been solved by changing the way they are received.

In the paper [18], a pin-on-disc wear apparatus has been used to carry out the tribological experiment for the magnetorheological liquid. It has been found that the sample wear rate with the magnetic field is higher than without it. The wear rate is in proportion to the rotating speed and rotating load.

In a similar manner, the magnetorheological fluid, intended for the use in a damper, has been tested [19]. Experimental studies consisted of the oscillating motion of the piston rod in a groove cut in a cube made of sealing material filled with magnetorheological fluid or a typical hydraulic oil. The load was 80 N, the amplitude was 7 mm, and the oscillation frequency was equal to 10 Hz. The test duration varied and ranged up to 48 hours. The piston rod wear was evaluated on the basis of measuring its surface roughness. After conducting the experiments, it was found that the measured wear of the piston rod is much greater when the magnetic fluid is used.

In [17, 20] papers, a method has been suggested for determining the durability of the magnetic fluid by means of S wear degree on the basis of the energy (converted into heat during the device operation) ratio, to the fluid volume, defined as:

$$S = \frac{1}{V}\int_0^t P dt \tag{1}$$

where:

P – the power converted to heat,
V – liquid volume,
t – time.

It has been assumed that the device works properly when the condition is fulfilled:

$$S > \mathrm{S_b} \tag{2}$$

where:

S_b – limit value of the wear degree for the magnetic liquid from 10^5 J/cm^3 to 10^7 J/m^3.

A new electrorheological fluid studied in the paper [16] has been investigated in a damper. During the tests, the damper piston travelled 40 km, and the damper filled with 200 ml of liquid 1.7×10^7 J scattered the energy, which means that the wear degree S defined in the papers [17, 20] was equal 0.85×10^5 J/cm^3. After the tests have been completed, no degradation of the electrorheological fluid, seal damage, or other elements of the damper have been found.

The publication [14] presents the results concerning the research on the durability of the clutch filled with magnetorheological fluid, destined for the drive of the cooling system fan used in a vehicle. The durability test has been based on the clutch work, operating on the test rig for 500 hours at various speeds of the input shaft (600, 1600, 2000, 2700 rev/min). The torque transmitted by the clutch is proportional to the square of the angular velocity of its input shaft. After the completion of the test, no changes in the clutch performance were noticed. The degree of the adaptive liquid S wear, defined in papers [17, 20], was equal to 7.3×10^7 J/cm^3.

According to the results of the studies, the most important factors affecting the durability devices filled with adaptive fluids are:

- electrorheological fluid (quantity, composition, particle construction),
- fluid working conditions (temperature, the amount of dissipated energy, ambient humidity),
- construction of the device (sealing, materials).

It should also be pointed that, currently, there is no uniform method for testing the durability of devices filled with adaptive fluids. The values of wear degree S calculated for the tested clutches and dampers exceed the value range of values from 10^5 J/cm^3 to cm^3 to 10^7 J/cm^3 suggested in the publication [17, 20]. It indicates the need for further research concerning ways of evaluation of durability of devices filled with adaptive fluids. Therefore, when implementing devices filled with new adaptive fluids, it is necessary to develop tailor-made durability tests.

3. Mathematical relationships used to assess the durability of clutches and brakes filled with adaptive fluids

In hydraulic clutches and brakes, both cylindrical and disc, the value of the transmitted torque M is proportional to the shear stress τ in the liquid and the value of angular velocity to sheer rate $\dot{\gamma}$. The following dependencies are practically used for clutches and cylindrical brakes [21]:

$$\tau = \frac{M}{2\pi r_1^2 b} \quad \dot{\gamma} = \frac{r_1 \omega}{r_2 - r_1} \tag{3}$$

or

$$\tau = \frac{M}{2\pi r_2^2 b} \qquad \dot{\gamma} = \frac{r_2 \omega}{r_2 - r_1} \tag{4}$$

where:

r_1 – the radius of the inner cylinder,
r_2 – the radius of the outer cylinder,
b – width of the cylinders,
ω – relative velocity of cylinders, Fig. 1.

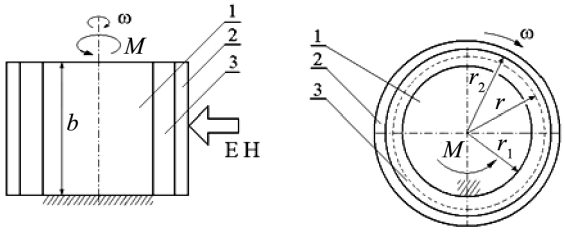

Fig. 1. Scheme diagram of the viscous clutch or brake: 1 – stationary cylinder, 2 – driven cylinder, 3 – gape filled with electrorheological fluid

Rheological properties of adaptive fluids are usually presented by means of dependencies of shear stress τ, occurring in the fluid, to shear rate $\dot{\gamma}$. The product of these two quantities determines the power P of the clutch or brake assuming constant working conditions, related to the volume V of the used fluid:

$$\tau\dot{\gamma} = \frac{P}{V} \tag{5}$$

During design calculations of hydraulic clutches and brakes filled with adaptive fluids, Bingham model is often used. There, the shear stress τ in the fluid, for the constant value of the electric or magnetic field strength, is defined as:

$$\tau = \mu_p \dot{\gamma} + \tau_0 \tag{6}$$

where:

μ_p – plastic viscosity,
$\dot{\gamma}$ – shear rate τ_0 – limit strength dependent respectively on electric E or magnetic B field strength, Fig. 2.

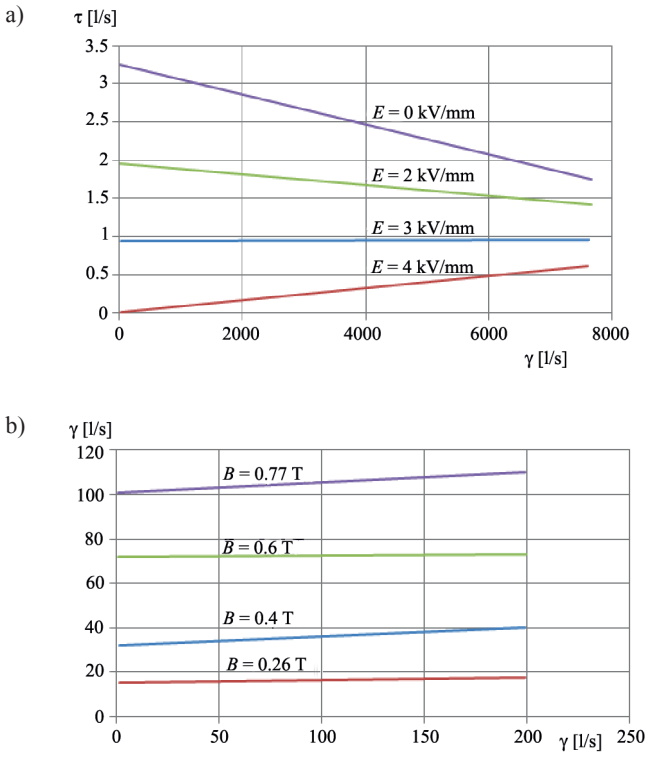

Fig. 2. Fluid rheological characteristics described by means of Bingham model: a) electrorheological fluid [22], b) magnetorheological fluid [23]

The formula (1), defining the wear degree S, in the case of hydraulic clutches and brakes filled with adaptive fluids and described with Bingham model, can be written in the following way:

$$S = \frac{P}{V} t = \tau \dot{\gamma} t = (\mu_p \dot{\gamma} + \tau_0) \dot{\gamma} t \tag{7}$$

As it is seen from Fig. 1, parameter value: μ_p and τ_0 in Bingham model, as well as the wear degree S, are significantly changed due to the electric field value. This change refers particularly to electrorheological fluids. The impact of the shear rate on the fuel wear degree is parabolic, and the impact of a device working time – linear. It should be noted that the plastic viscosity μ_p which is equal to the arc tangent of the angle of the straight varies due to the increase of the electric E and magnetic B field strength. Values differ from positive to negative ones. On the contrary, yield strength τ_0, determined for $\dot{\gamma} = 0$ always increases due to electric or magnetic field strength. Thus, it is possible that, depending on the parameter values μ_p and τ_0, the degree of the device wear will diminish together with the increase of angular velocity, which is not possible for typical hydraulic clutches.

For hydraulic clutches and brakes filled with adaptive fluids, in constant conditions, the wear degree S can be calculated on the basis of the formula (1) converted as follows:

$$S = \frac{P}{V} t = \frac{t}{V} \omega M \tag{8}$$

where:

P – power delivered to the clutch,
V – working fluid volume,
t – time job working fluid in the clutch,
ω – the relative angular velocity,
M – torque transmitted by the clutch.

The minimum volume V of the fluid ensuring the proper operation of viscous brake can be calculated from the dependence [24]:

$$V = \left(\frac{\mu_p}{\tau_0^2} \right) \left(\frac{M_\tau}{M_\mu} \right) \left(M_\tau \omega \right) \tag{9}$$

where:

M_μ – torque in case of adaptive fluid activation absence,
M_τ – torque in case of adaptive fuel activation,
ω – relative angular velocity.

In practice, the liquid volume used in prototype valves, linear dampers as well as clutches filled with the magnetorheological fluid, is much greater than the one calculated according to formula (9) and takes values from 25 V to 50 V [20].

4. Hydraulic clutches and brakes filled with adaptive fuels durability tests

The durability test was performed for a cylindrical viscous brake and a dual clutch, which consisted of a cylinder viscous clutch and a hydrodynamic clutch, filled with various electrorheological fluids. A cylindrical viscous brake was mounted directly on the axis of the electric motor engine. The bearings of the driving brake part were inside the brake, whereas driving and driven parts of the dual clutch were mounted outside the clutch.

A. Cylindrical viscous brake durability testing

A cylindrical viscous brake, as shown in Fig. 3, consists of two cylindrical parts with different diameters, forming electrodes, electrically isolated from each other, which are connected to the high voltage power supply through the commutator and electric wires [25, 26]. The cylinders are made of aluminum. The external diameter of the brake is 160 mm and its width 90 mm. The size of all construction joints, filled with the working fluid, is 1 mm.

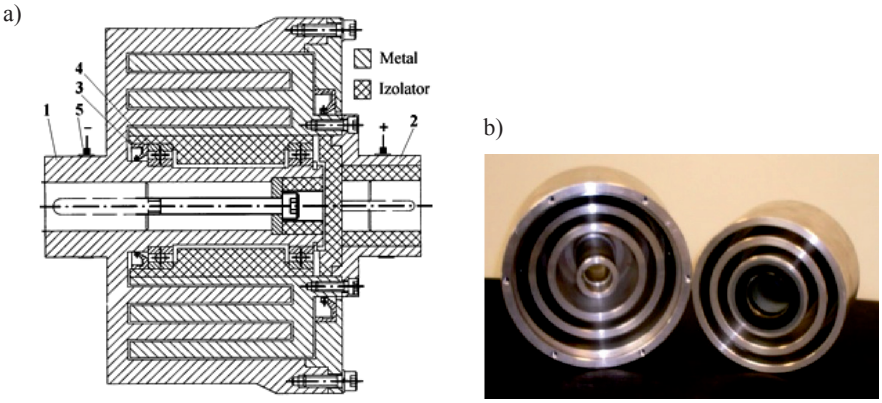

Fig. 3. Scheme of the cylinder viscous brake design; a) cross-section: 1 – driven element of the brake, 2 – a stationary brake part 3 – sealing ring 4 – ball bearing 5 – commutator rings; b) general view

The driven part of the brake is located on ball bearings installed on a sleeve connected to an external part of the brake, sealed with a typical sealing ring.

The brake was filled with two different electrorheological fluids. The data is presented in Table 1.

Table 1

The basic data of the tested ER [4]

Fluid symbol	Manufacturer	Density [kg/m^3]	Fluid volumetric composition	Volume [cm^3]
LID 3354S	Smart Technology Ltd, UK [22]	1460	37% polymer, silicone oil	140
CES35	Technical University in Radom, PL	95	35% soluble starch, transformer oil	140

A dual clutch mounted on the test rig, as shown in Fig. 4, enables the measurement of the angular velocity ω and the transmitted torque *M*. During the test, the voltage 1 kV was adjusted to the brake cylinders.

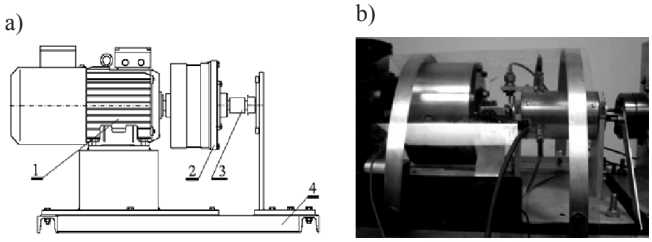

Fig. 4. Scheme of the test rig for testing the durability of cylindrical viscous brake; a) construction scheme: 1 – controlled electric motor, 2 – tested brake, 3 – torque meter, 4 – test rig frame; b) general view

After the test rig was started, for both liquid at time *t*, given in Table 2, a significant increase in the value of the transmitted torque showing the brake damage was noticed.

Table 2

Test conditions and results of cylinder viscous brake

Fluid symbol	w [rad/s]	M [N×m]	T [°C]	t [hour]	S [J/cm^3]
LID 3354S	50	1.9	40–50	70	1.7×10^5
CES35	50	0.9	40–50	55	0.6×10^5

After the brake has been disassembled, in both cases, the presence of solid particles in the electrorheological fluid, in the bearings and on the sealing ring inner surfaces has been noticed, Fig. 5.

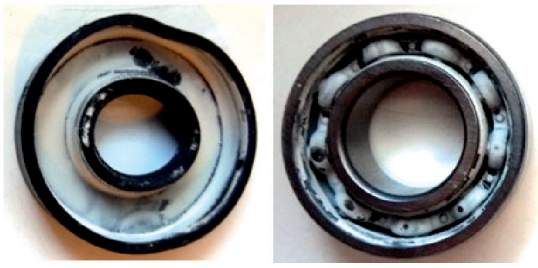

Fig. 5. View of solid particles in the electrorheological fluid in bearings and on the sealing ring inner surfaces

The reason of a significant increase of the brake torque values was rolling of solid particles included in the electrorheological fluid through ball bearings on bearing ring tracks and the formation of a layer, which obviates the clearance between bearing elements. It caused an increase of the resistance movement.

No adverse chemical impact of the fluid on the material of the sealing ring was observed. The cylinder surface became dull and there were no pits or scratches. Under the microscope, no significant changes in the size and shape of solid particles were noticed in the fluid taken from the brake. During the studies with rheometer, there were no significant changes noticed in the coefficient of dynamic viscosity of the two fluids.

B. Dual clutch durability test

A dual clutch consists of a hydrokinetic clutch and a viscous clutch cylinder located in a common housing [27]. The torque *M* transmitted by the dual clutch is the sum of moments carried by the hydrokinetic and viscous clutches. Rotors of the hydrokinetic clutch have flat radial blades. A viscous clutch is made of co-axial cylinders, isolated from each other. The driving and driven parts of the clutch as well as the housing are made from standard steel. The electric field acting on the electrorheological working fluid is produced in the gap between the cylinders with a width of 1 mm. The brake external diameter is 250 mm and its width is 110 mm. Fig. 6 shows a sectional view of the dual clutch.

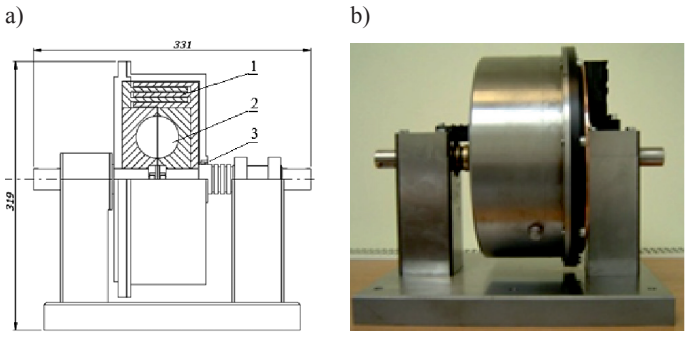

Fig. 6. Dual clutch: a) construction scheme, b) general view

The input and output shafts of the dual clutch are located outside the housing. The housing is sealed with the sealing ring mounted on the clutch output shaft. The voltage necessary to generate an electric field is applied to the cylinders through a copper-carbon brushes cooperating with the copper rings arranged on the output shaft of the clutch. Coupling complex was filled with the electrorheological fluid, whose data are shown in Table 3. The dual clutch was installed on the testy rig that enables the measurement of the angular velocity ω and the transmitted torque *M*, Fig. 7. During the research, the driving part of the clutch rotated with a speed of 100 rad/*s*, and the voltage of 1 kV was adjusted to the dual clutch cylinders.

Table 3

Basic data of the liquid used in the dual clutch [28]

Fluid symbol LID 3354S	Smart Technology Ltd, UK [22]	Density [kg/m^3]	Fluid volumetric composition	Volume [cm^3]
ERF #6	KCNiTCS Faculty of Chemistry, Warsaw University of Technology, PL	1074	35% sulfonated resin styrene – divinylbenzene resin, silicone oil	880

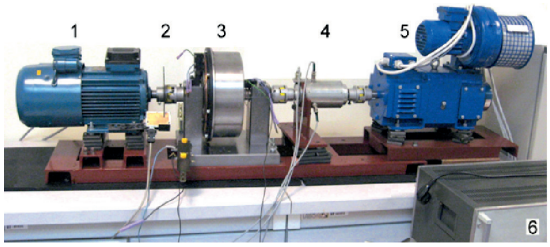

Fig. 7. View of the test bench with the installed dual clutch: 1 – electric motor, 2 – dual clutch, 3 – torque meter, 4 – electric brake, 5 – high voltage power supply

The electrorheological fluid ERF # 6 was working in the hydraulic dual clutch for 645 hours until the liquid leakage through the sealing ring was observed. After 600 hours, high voltage fluctuations were noticed. The fluctuations were caused by avalanche breakdowns. After the clutch was dismantled, the presence of solid particles of the electrorheological fluid on the inner surfaces of the sealing ring were observed as well as mechanical damage of the sealing surface, Fig. 8.

Fig. 8. The effects of the sealing ring wear

No adverse effects of the fluid chemical impact on the sealing ring material were observed. The cylinder surface was smooth, without pits or scratches; however, on the internal surfaces of the housing, corrosion was observed, Fig. 9.

As a result of observation under a scanning electron microscope, it was found consumption of solid spherical particles electrorheological fluid, such as flattening, damage the surface, adhesion of contaminants to the solid particles, Fig. 10.

Fig. 9. Corrosion spots inside the dual clutch housing

a) b) c)

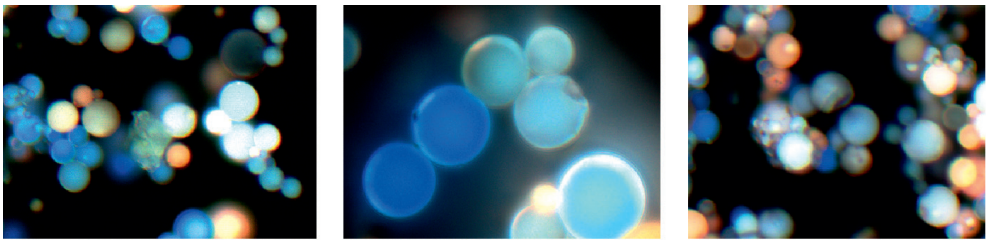

Fig. 10. Damage of the fluid solid particles ERF# 6 seen under UV light (365 nm), 400 times magnified: a) flattening of spherical solid particles, b) damage of the spherical particle surface damage, c) pollutants stuck to particles

However, the number of damaged particulates did not exceed a few percent, which indicates the beginning of the electrorheological fluid wear. Under the microscope, there was no evidence of silicone oil degradation, which is the electrorheological fluid liquid phase. During tests carried out on the rheometer, no significant changes in the coefficient of dynamic fluid viscosity ERF#6 were observed.

The value of the wear degree S of the electrorheological fluid working in the dual clutch, calculated on the basis of the formula (8) was 2.6×105 J/cm^3.

5. Evaluation of test results

As is clear from the research, the most important factor affecting the durability of viscous brake and dual clutch is the method of sealing the bearings and space with the electrorheological fluid. Also, the material of the electrorheological fluid particles is important. Particles made of a soft material are more easily deformed while rubbing against each other or against the cylinder walls, which is the reason of their easier passage through the seals. For this reason, the viscous brake filled with the fluid CES35, which consists of soft starch particles, crashed very quickly.

In order to increase the durability of devices filled with adaptive fuels, it is useful to put bearings outside of the housing. Although this design solution means the increase of the device size, it enables, according to the studies, the increase of the seal ring durability by nearly 10 times.

The observed degradation of solid particles of the fluid ERF# 6 are mainly associated with their movement inside the dual clutch housing. Particles moving between the viscous clutch cylinders and into the channel formed by the blades of the hydrodynamic clutch rub against the walls and against each other, and hit the blades during the flow of the electrorheological fluid from one hydrodynamic clutch rotor to another. The movement of solid particles is intensive, as it is apparent from the calculations for the angular speed of the clutch driving part, which is 100 rad/s, the flow velocity of the electrorheological fluid flow speed reach 5.5 m/s, and the maximum angles of impingement of the liquid stream on the blades reach the value of 55° [29]. The flatness of particles indicates the plastic properties of the material that they are made of. The reasons of pollution that has been observed in electrorheological fluids can be: corrosion and seal ring mechanical wear.

The type of used materials also influences the brake durability. As it is clear from the tests described in the paper, as well as the author's experience concerning devices filled with electrorheological fluid, aluminum is a better material for housing including adaptive fluids, because it does not corrode like a typical steel. The use of appropriate insulation materials ensures long and proper brake operation.

In order to achieve high durability of clutches and brakes filled with adaptive fluids, it is also necessary to provide adequate working conditions of devices. The most important factors are temperature and humidity. The device operating temperature results from the balance of heat supply and discharge. The amount of discharged heat into the environment is related to the brake size and the materials it was made of. The larger the brake and higher the thermal material conductivity, the lower is its working temperature. The temperature has a direct impact on electrorheological fluid properties and its destruction. In the case where the temperature increase causes shear stress τ increase, the power converted into heat in the device increases in the electrorheological fluid and consequently its durability decreases.

Ambient humidity has a significant impact on the durability because water percolating into the electrorheological fluid can cause degradation of fluid due to the electrolysis, as well as it can cause an increase in shear stress τ, and also be the reason of corrosion of clutch or brake parts.

6. Conclusions

So far, the studies concerning the durability of devices filled with adaptive fluids have been performed for a small number of selected devices in specific working conditions, so the results do not provide a complete answer to questions on wear mechanisms of both their parts and adaptive fluids. Therefore, further experimental studies related to the durability of devices filled with adaptive fluids are necessary.

The experimental studies of the dual clutch and viscous brake, including three electrorheological fluids, show that the most important factors affecting the durability are: sealing of rolling bearings as well as working space filled with adaptive fluid, the type of adaptive fluid as well as the isolation of electrodes and electrical wires, supplying high voltage from the power supply. Electrorheological fluid durability, defined by means of the wear degree S, is within the ranges reported in the literature and does not differ significantly from the magnetorheological fluid durability.

Due to the presence of solid particles in adaptive fluids, it is necessary to use sealing rings adapted to work with mixtures containing particles. While selecting sealing rings, the impact of chemical ingredients of the electrorheological fluid on the material the ring has been made of should also be taken into account.

The durability of the electrorheological fluid solid particles is less than the silicone oil durability. The basic forms of particle mechanical wear include both surface flattening and damage. However, crushing of solid particles included in the electrorheological fluid, characteristic for linear dampers, which causes the large increase of dynamic viscous coefficient for the inactive electrorheological fluid, has not been observed.

References

[1] Papadopoulos C.A., *Brakes and Clutches Using ER Fluids*, Mechatronics 8, 1998, 719–26.

[2] Li H.W, Du H., *Design and Experimental Evolution of a Magnetoreological Brake*, Int. J. Adv. Manuf. Technol, 21, 2003, 508–515.

[3] Stevens N., Sproston J., Stanway R., A*n Experimental Study of Electro–rheological Torque Transmission*, Transaction of the ASWE, Vol. 110, June 1988, 182–188.

[4] Kesy Z., *Prospects for the Control of a Torque Converter Using Magnetic Fluid*, International Colloquium – Innovative Actuators for Mechatronic Systems, Londyn 1995, 10.1–10.3 2.

[5] Conrad H., E*lectrorheological Fluids: Characteristics, Structure and Mechanisms*, FED–Vol. 164, Electro-Rheological Flow, ASME, 1993, 99–113.

[6] Stanway R., *Smart Fluids: Current and Future Developments*, Material Sciences and Technology, Vol. 20, 2004, 931–939.

[7] Weiss D. et al., *High Strength Magneto- and Electro-Rheological Fluids*, SAE Technical Paper 932451, 1993, 425–430.

[8] Fertman V.E., *Magnetic Fluids Guide Book: Properties and Applications*, Hemisphere Publishing Corporation, 1990.

[9] Nakamura T., Saga N., Nakazawa M., *Impedance Control of a One Shaft-Type Clutch Using Homogeneous Electrorheological Fluid*, Journal of Intelligent Material Systems and Structures, Vol. 13, No. 7–8, 2002, 465–469.

[10] Inoue A, Ryu U., Nishimura S., *Caster-walker with Intelligent Brakes Employing ER Fluid Composed of Liquid Crystalline Polysiloxane*, Proceedings of the Eighth International Conference on Electrorheological Fluids and Magnetorheological Suspensions, Nice, France 9–13 July 2001, World Scientific Publishing Co. 2002, 23–29.

[11] Kesy Z., Kesy A., Rudnicki J., *An Experimental Study of Controlled Breaker with Magneto-Rheological Working Fluid*, [in:] R.M. Parkin, A. Alhaibeh, M.R. Jackson (Ed.), International Conference on Mechatronics ICOM 2003, Professional Engineering Publishing Limited, London 2003, 321– 326.

[12] Kesy Z., Kesy A., Plocharski J., Jackson M., Parkin R., *An Example of Design – Embodiment for Electrorheological Fluid Based Mechatronic Transmission Components*, International Journal of Mechatronics 16 (1), 2006, 33–39.

[13] Park E.J., da Luz L.F. Suleman A., *Multidisciplinary Design Optimization of an Automotive Magnetoreological Brake Design*, Computers and Structures, 2007.
[14] Smith A.L., Ulicny J.C., Kennedy L.C., *Magnetorheological Fluid Fan Drive for Trucks*, Journal of Intelligent Material Systems and Structures, Vol. 18, No. 12/2007, 1131–1136.
[15] Sztompka P., Krzton-Maziopa, Plocharski J., *Electrochemical and Thermal Degradation of Electrorheological Fluids*, International Conference ERMR, Philadelphia 2010.
[16] Gurka M., Adams D., Johnston L., Petricevic R., *New Electrorheological Fluids – Characteristics and Implementation in Industrial and Mobile Applications*, 11th Conference on Electrorheological Fluids and Magnetorheological Suspensions, Journal of Physics: Conference Series 149, 2009.
[17] Carlson J.D., *What Makes a Good MR Fluid?*. 8th International Conference on Electrorheological Fluids and Magnetorheological Suspensions, July 9–13, Nice 2001.
[18] Juncheol Jeon, Sung Hoon Ha, Min-Sang Seong, Seung-Bok Choi,Young-Min Han, *Wear Characteristics of Electrorheological Fluids with Different Base Oil and Particle Concentration*, International Journal of Civil Engineering and Building Materials, Vol. 1, No. 1, 2011.
[19] Iyengar V.R., Alexandridis A.A., Tung S.C., Rule D.S., *Wear Testing of Seals in Magneto-Rheological Fluids*, Tribology Transactions, 47:1, 2004, 23–28.
[20] Carlson D.J., *MR Fluids and Devices in the Real World*, 9th International Conference on Electro-Rheological Fluids, Magneto-Rheological Suspensions and Associated Technology, Beijing 2004, 531–538.
[21] Whorlow R.W., *Rheological Techniques*, Second Edition, Ellis Horwood Limited, 1992.
[22] www.smarttec.co.uk.
[23] Gene S., Phule P., *Rheological Properties of Magnetorheological Fluids*, Smart Materials and Stuctures 11, 2002, 140–146.
[24] Carlson J.D., *Magnetorheological Fluid Actuators*, Chapter on Magnetorheological Fluid Actuators in Adaptronics and Smart Structures, Jendritza D.J., Janocha H., Springer Verlag, 1997.
[25] Kesy Z., Kesy A., Olszak A., Jackson M., Parkin R., *Modelling of Unsteady-state Motion of Transmission System with Electrically Controlled Viscotic Clutch*, Proc 5th Internation Workashop on Research and Education in Mechatronics, Kielce–Cedzyna 2004, 223–227.
[26] Kesy Z., Kesy A., Jackson M.R., Parkin R.M., *Investigation of Viscotic Clutch with Electrorheological Fluid*, International Review of Mechanical Engineering, Vol. 2, No. 4, 2008, 592 – 597, .
[27] Ziabska E., Musialek I., Olszak A., Kesy Z., *Durability Assessment of Elektroreological Fluids*, Hydraulics and Pneumatics 3/2013, 8–11 (in Polish).
[28] Plocharski J, Drabik H., Wycislik H., Ciach T., *Electrorheological Properties of Polyphenylene Suspensions*, Synthetic Metals 88, 1997, 139–145.
[29] Ziabska E., Olszak A., Kesy Z., *B-spline Application in Calculation of Hydrodynamic Torque Converters with Electrrheological Fluids*, Mechanic, No. 12, 2013, 43–50 (in Polish).

TECHNICAL TRANSACTIONS | CZASOPISMO TECHNICZNE
MECHANICS | MECHANIKA
5-M/2016

DOI: 10.4467/2353737XCT.16.289.6121

BOGDAN SŁODKI*

BUILD UP EDGE PHENOMENON AND CHIP FORMS IN INCONEL 625 ALLOY LONGITUDINAL TURNING – CASE STUDY

ZJAWISKO NAROSTU ORAZ FORMY WIÓRÓW UZYSKANE PRZY TOCZENIU WZDŁUŻNYM STOPU INCONEL 625 – STUDIUM PRZYPADKU

A b s t r a c t

The paper presents the wear process of a carbide insert in Inconel 625 longitudinal turning as well as examples of chip forms. Inconel 625 alloy belongs to the difficult-to-cut material group and causes many problems in machining operations in industry. A major one concerns chip forms produced in turning operations and quick wear of the cutting edge. The conveyed research also revealed the Build Up Edge (BUE) phenomenon, which took place in conveyed tests. A few examples have been presented and analyzed.

Keywords: machining, turning, tool wear, BUE

S t r e s z c z e n i e

W artykule przedstawiono proces zużycia płytki z węglików spiekanych oraz postacie wiórów uzyskanych podczas toczenia wzdłużnego stopu Inconel 625. Inconel 625 należy do grupy materiałów trudnoskrawalnych i sprawia sporo problemów w obróbce skrawaniem. Dotyczą one głównie trudności w uzyskiwaniu korzystnej postaci wiórów i bardzo szybkie zużycie ostrza. Przeprowadzone badania ujawniły także zjawisko powstawania narostu na krawędzi skrawającej. Zaprezentowano i przeanalizowano kilka przykładów.

Słowa kluczowe: obróbka wiórowa, toczenie, zużycie ostrza, narost

* D.Sc. Ph.D. Eng. Bogdan Słodki, Institute of Production Engineering, Faculty of Mechanical Engineering, Cracow University of Technology.

1. Introduction

When observing contemporary trends in machining, it can be noticed that the important thing is to pay attention to research concerning the variety of factors influencing the quality of processes. Such factors like the influence of cutting data on the surface roughness and cutting forces in machining extremely difficult-to-cut materials (e.g. sintered carbide) are the examples of such research activity [10, 11]. Additionally, cost effectiveness combined with cutting data selection process is a very important factor in any kind of machining [12].

One of the factors, which should be investigated, is chip form achieved in turning operations. The rake face of a carbide insert has a significant impact on this phenomenon.

The rake face of a modern insert is usually shaped in a chip breaker or chip former according to the terminology used by various manufacturers. Its task is to direct a chip towards the flank face of an insert or a raw surface of a workpiece. When a chip hits an obstacle, it breaks. The field of the chip breaker application is crucial for the final process of cutting data selection. This is particularly important when difficult-to-cut materials like HRSA (Heat Resistant Super Alloys) are machined. Chips are a waste product in every kind of machining and their unacceptable form (long and curly) can have a destructive impact on the quality of the machined surface. In the worst case, especially in automated manufacturing systems, they can cause catastrophic tool wear and even stop the production.

HRSA are generally resistant to temperature and corrosion. They can be divided into alloys based on nickel, cobalt and iron. In machining operation, these alloy components can cause quick wear of a tool, mainly due to chipping, deformation and work surface hardening [3]. The last one mentioned is the reason of depth-of-cut-line notching and can also compromise the fatigue strength and geometric accuracy of the part. Chips are usually difficult to control. High temperature in cutting zone and high cutting forces are also standard in machining operations. Low thermal conductivity of Inconel 625, (a representative of HRSA alloys), 9.8 W/(m · K), in contrary to steel C45 thermal conductivity, which is 50 W/(m · K), is the cause of very high temperature on the cutting edge, the main reason for fast tool wear process. These are important factors concerning tool life and chip forms.

Tool life depends on tool wear. The most popular are rake face tool wear (crater) and flank face tool wear. The latter is described by VB indicator in various form, the most popular and easy to measure is the average value of VB marked VB_B [5]. The interesting form of a tool wear is BUE (Build UP Edge). Theoretical background of BUE in turning is described in [4]. Generally, BUE consists of free particles of machined metal, which are not a part of a chip, but they are glued by the adhesion phenomenon to the cutting edge of a tool. BUE changes the geometry of a tool, especially a rage angle, leading to the changes of chip breaker geometry and deterioration of surface roughness.

Many problems concerning HRSA machining are described in details in application guides recommended by tool manufacturers, SANDVIK-Coromant, for example [1, 9]. It must be remembered that local operating features (machining system consisting of tool-machine tool-workpiece material) have significant influence on these recommendations [8]. For all the reasons described above, high temperature alloys deserve special machining techniques.

2. Research object

Inconel 625 was used as a work material [9]. It is a nickel-chromium-molybdenum based alloy widely used in aircraft engine constructions, chemical and shipbuilding industries.

As it was mentioned above, Inconel 625 belongs to super alloys (HRSA) so all problems concerning the machining of this group of alloys concern Inconel 625 machining.

In tests, ISCAR produced and recommended for HRSA turning, VCMT 160404 insert (Fig. 1) with SM type chip breaker geometry was used, grade IC 907 coated with TiAlN layer [2]. The insert was mounted to a tool holder SVJCR 2020K. Chip breaker recommended application area was a_p = 0.5–2.5 mm, f = 0.05–0.25 mm/rev. Fig. 2 shows a cutting edge of a new insert.

The cutting data used in tests are presented in Table 1. The value of feeds were determined by the feed system used in the lathe. Two values of feed were selected, the second approximately three times greater than the first one. Preliminary tests have demonstrated correct chip forms for a brand-new insert for each set of data [6].

The work piece used in tests (diameter Dc = 35 mm) was divided into 5 mm sections, so 15 tests took place. After turning each section, the insert wear was measured, the chip form was classified, the recordings of the turning process were analyzed and BUE removed.

Table 1

Cutting data used in tests

Chip breaker type	SM
Cutting speed, v_c [m/min]	65
Feed, f [mm/rev]	0.077, 0.211
Depth of cut, a_p [mm]	1.0

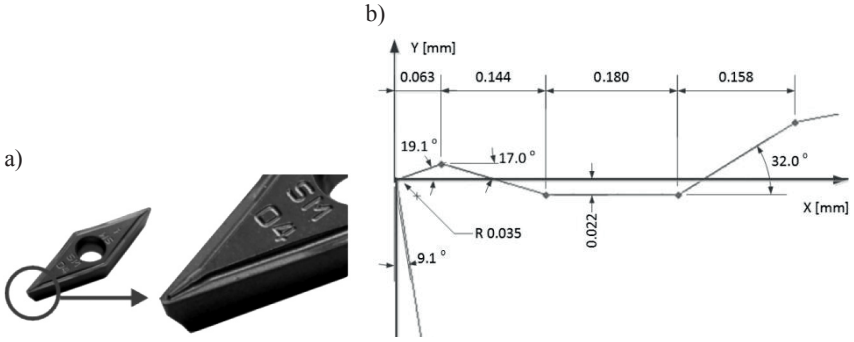

Fig. 1. Insert VCMT 160404-SM IC 90; a) general view, b) measured dimensions of chip breaker type SM [7]

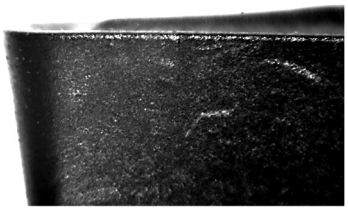

Fig. 2. The cutting edge of a new insert VCMT 160404-SM

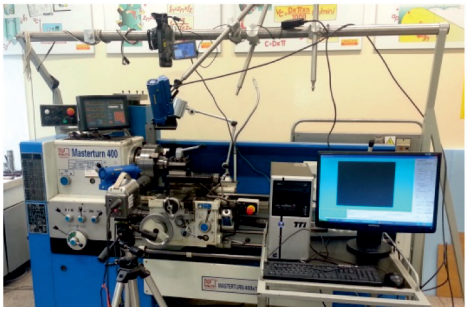

Fig. 3. Research stand for recording phenomena in the cutting zone in turning

The main components of research stand (Fig. 3) consisted of:

– Masterturn 400 lathe,
– high speed camera Phantom V5.2,
– spot illumination systems,
– 3-D Digital Kayence microscope,
– tool room microscope with MicroCamLab computer program.

There was no coolant used in machining tests in order to enable good quality chip photo acquisition. Additionally, coolant could affect chip forms. Acquisition parameters used for high speed camera were as follow: recording rate 1000 fps, resolution 1152 × 896 pixels.

3. Chip forms

Chips formed in machining were described and classified. Examples are presented in Tab. 2 and 3. Table 2 presents examples of chips for two tested feeds when the flank wear VB_B (e.g. average value of VB) was equal to 0.3 mm. All photos reveal correct chip forms. Chips were short and segmental. The second table (Tab. 3) exhibits chip photographs when unacceptable chips appeared.

Table 2

Chip forms achieved in Inconel 625 turning for VB_B = 0.3 mm [7]

	f = 0.077 mm/rev VB_B = 0.3 mm	f = 0.211 mm/rev VB_B = 0.3 mm
Correct chips, segmental, short helical, loose arc		

Table 3

Unacceptable chip forms achieved in Inconel 625 turning [7]

	f = 0.077 mm/rev VB_B > 0.45 mm	f = 0.211 mm/rev VB_B > 0.4 mm
Unacceptable long helical and tangled chips		

The flank wear indicator has different value for each feed. Chips were generally long, continuous and tangled. For the feed f = 0.077 mm/rev correct form of chips occurred up to VB_B = 0.45 mm. Respectively, for the feed f = 0.211 mm/rev, correct chips were present up to VB_B = 0.4 mm

4. Tool wear and BUE phenomenon analysis

Research revealed typical forms of insert wear, but abrasive wear on a flank face was dominant. The change of VB_B indicator value in consecutive tests, for two values of feed, is presented in Fig. 4.

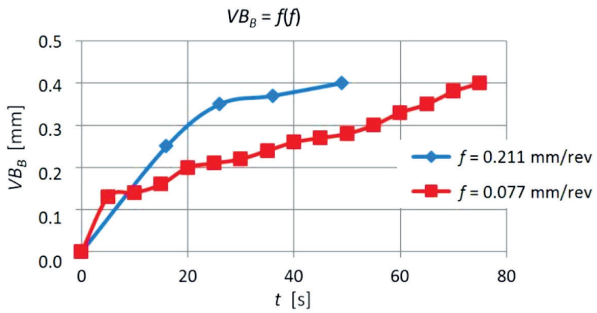

Fig. 4. Change of VB_B value in consecutive tests

The curve for f = 0.077 mm/rev shows almost a classic character of tool wear. If the value of feed increases, a tool wear curve is close to linear. When the time of cutting reached approximately $t \approx 100$ s, VB_B indicator exceeded 0.45 mm and then unacceptable form of chip was registered (Fig. 5).

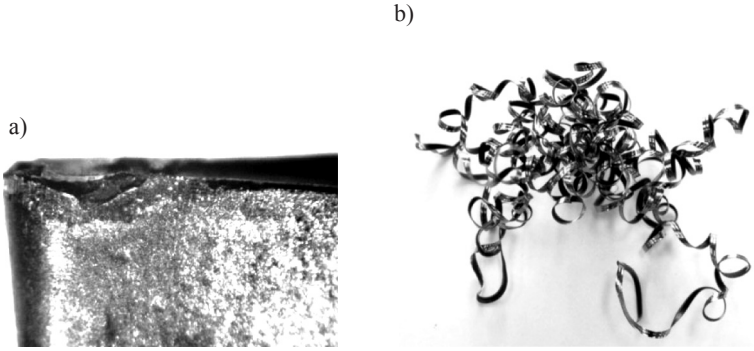

Fig. 5. Example of final stage insert wear: a) flank face wear photo, b) long tangled chips; f = 0.077 mm/rev, v_c = 65 m/min, a_p = 1.0 mm, $t \approx 100$ s [7]

Visual observation of the cutting edge of the wear insert showed many deformations, small grooves and crates caused mainly by abrasive wear. Since BUE (Build Up Edge) phenomenon was observed a few times during machining, adhesive wear must also have taken place.

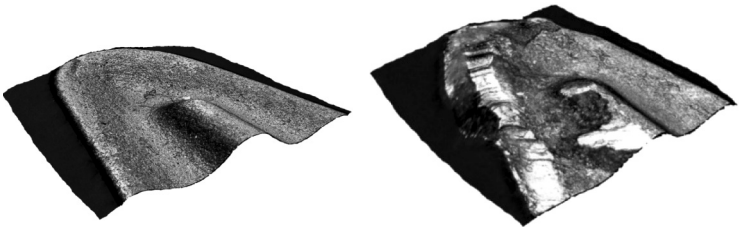

Fig. 6. 3-D view of a new insert rake face and after time of cutting $t \approx 100$ s, f = 0.077 mm/rev, v_c = 65 m/min, a_p = 1.0 mm

Fig. 6 presents views of the rake face of the worn insert. An extensive wear of a backwall of a chip – groove is noticeable. This is probably the cause of unacceptable chip forms in this stage of machining. A chip was not directed towards an obstacle (a flank face of an insert or raw surface of a workpiece) to be broken.

As it was mentioned above, in a few tests for cutting data f = 0.077 mm/rev, v_c = 65 m/min, a_p = 1.0 mm BUE phenomenon took place. This caused temporary direct change of chip form from correct to unacceptable.

Table 4 presents the test number (out of 15) in which this phenomenon was observed, along with the appearance of the cutting edge, the chip form achieved in particular test as well as VB_B value. Characteristic grooves are visible on the flank face. It is caused by abrasive interaction between cutting edge and the workpiece machined surface. Fig. 7 shows the basic dimensions of BUE which allow to define changes in cutting wedge geometry, while Table 5 presents dimensions of BUE in particular tests.

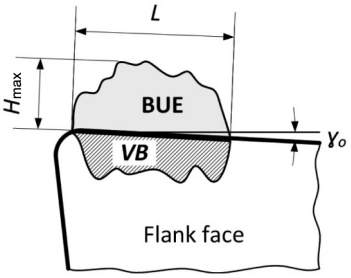

Fig. 7. Basic dimensions of BUE

Table 4

BUE phenomenon and chip form in selected tests

Test number	Flank face and cutting edge	Corresponding chip form	VB_B
3	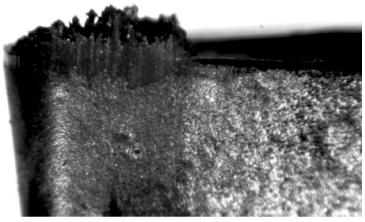		$VB_B = 0.16$ mm
4	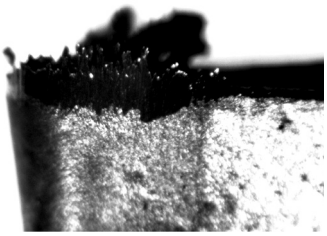		$VB_B = 0.2$ mm
5	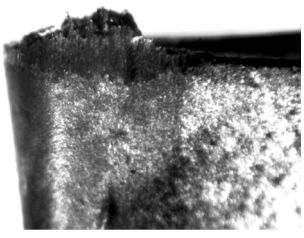		$VB_B = 0.21$ mm

7	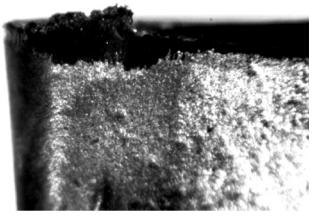	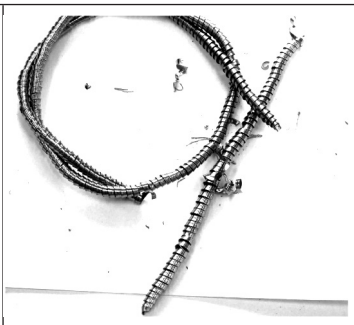	VB_B = 0.24 mm
13	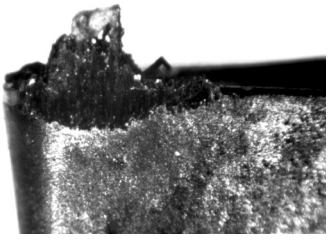		VB_B = 0.35 mm

Table 5

BUE dimensions in selected tests

Test number	Photographs of BUE phenomenon	BUE dimentions (H_{max}, L)
3	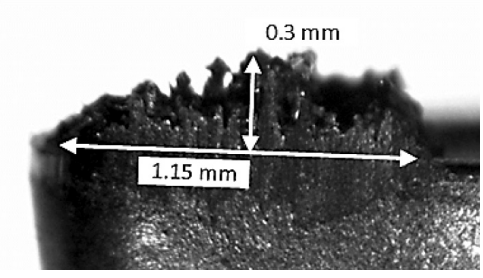	H_{max} = 0.3 mm L = 1.15 mm
4	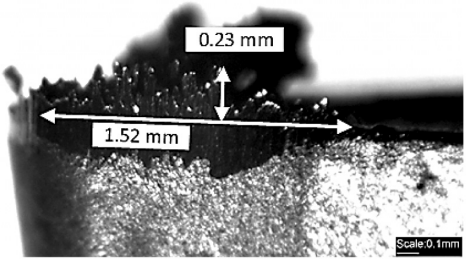	H_{max} = 0.23 mm L = 1.52 mm

5	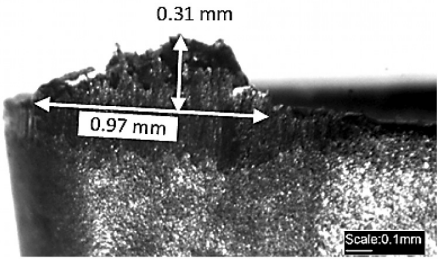	H_{max} = 0.31 mm L = 0.97 mm
7	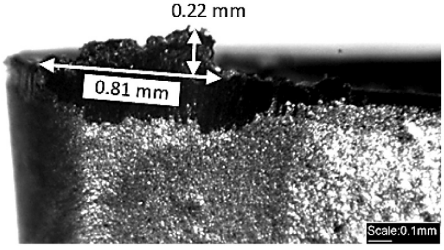	H_{max} = 0.22 mm L = 0.81 mm
13	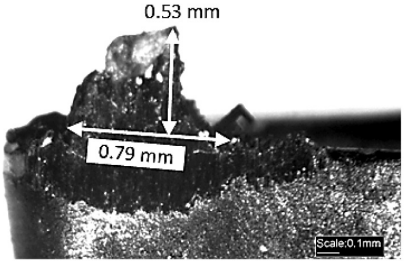	H_{max} = 0.53 mm L = 0.79 mm

5. Conclusions

The investigation of the tests led to the conclusion that the BUE phenomenon occurred more often than not in the first stages of tool wear. Especially up to VB_B = 0.26 mm. It created unacceptable chip form. After removing BUE, a return to the beneficial chip form took place. So it is obvious that the tested set of cutting data was disadvantageous; the technologist could be misled assigning the disadvantageous form of chips to excessive tool wear. The remedy would probably concern the increase of cutting speed, but that could have disadvantageous influence on tool life. Another way would be to use a different grade of carbide insert recommended by a tool manufacturer (verifying tests would be necessary in this case) or feed change (for the feed f = 0.211 mm/rev this phenomenon did not appeared). The change of feed leads to a different roughness of the machined surface – in this case – deteriorates it.

Generally, flank wear of VCMT 160404 – SM insert had no significant influence on chip forms for stable, correctly selected cutting data. For the majority of tool wear time, chip forms were correct or acceptable. Loose arc or bounded arc chips were dominant up to significant tool wear when long, continuous chips of various kinds appeared. The primary cause of unacceptable chip creation was the wear of the chip groove backwall (Fig. 6).

Short tool life in the tests was caused by the fact that machining was performed without coolant. Industrial practice shows that coolant with almost 17% of oil is convenient in the case of Inconel alloys machining.

References

[1] *Aerospace Engine – application guide*, Sandvik Coromant, 2004.

[2] Catalog ISCAR, *Turning tools*, 2008, H37.

[3] Ezugwu E.O., Wang Z.M., Machado A.R., *The machinability of nickel based alloys: a review*, Journal of Materials Processing Technology 86, 1999, 1–16.

[4] Józwik J., Domińczuk J., *Analiza doświadczalna zjawiska narostu podczas toczenia,* Eksploatacja i Niezawodność *nr* 5, 2001, 53–57.

[5] PN-ISO 3685:1996, Badanie trwałości noży tokarskich punktowych.

[6] Słodki B., *Chip forms in turning Inconel 625 with –SM ISCAR chipformer*, XXIV microCAD International Scientific Conference, 2010, 175–180.

[7] Słodki B., Struzikiewicz G., *Zmiana postaci wióra w procesie zużycia ostrza z węglików spiekanych w toczeniu wzdłużnym stopu Inconel 625*, [w:] *Obróbka skrawaniem, nauka a przemysł*, pod redakcją Wita Grzesika, Wydawnictwo Sutoris, Opole 2011, 158–167.

[8] Słodki B., Zębala W., *Efektywny zakres pracy łamacza wiórów a lokalne warunki obróbki w toczeniu materiałów trudnoskrawalnych*, Obróbka skrawaniem, Instytut Zaawansowanych Technologii Wytwarzania, Kraków 2008, 262–271.

[9] *Superstopy żaroodporne –poradnik*, Sandvik Polska S.p. z.o.o, 2007.

[10] Zebala W., Kowalczyk R., *Estimating the effect of cutting data on surface roughness and cutting force during WC-Co turning with PCD tool using Taguchi design and ANOVA analysis*, International Journal of Advanced Manufacturing Technology, vol. 77, Issue: 9-12, 2015, 2241–2256.

[11] Zebala W., Kowalczyk R., *Cutting Data Influence on Cutting Forces and Surface Finish During Sintered Carbide Turning*, Key Engineering Materials, vol. 581, 2014, 148–153.

[12] Zebala W., Plaza M., *Comparative study of 3-and 5-axis CNC centers for free-form machining of difficult-to-cut material*, International Journal of Production Economics, vol. 158, 2014, 345–358.

TECHNICAL TRANSACTIONS | **CZASOPISMO TECHNICZNE**
MECHANICS | MECHANIKA
5-M/2016

DOI: 10.4467/2353737XCT.16.290.6122

ŁUKASZ ŚLUSARCZYK, AGATA NOWAK*

INFRARED CAMERA APPLICATION IN CREATION OF THE DIAGNOSTIC METHOD FOR DEEP VEIN THROMBOSIS IN THE DISTAL PARTS OF THE BODY

OPRACOWANIE METODY DIAGNOSTYCZNEJ ZAKRZEPICY ŻYŁ GŁĘBOKICH W CZĘŚCIACH DYSTALNYCH CIAŁA Z WYKORZYSTANIEM KAMERY TERMOWIZYJNEJ

Abstract

The main purpose of this paper is to show major increases in the temperatures of the lower extremity limb in comparison to the latter. During the course of the study, it was found that a significant difference in the temperatures arises between the healthy left limb (subject to the conducted tests) and the sick right ('control') one, before and after performing an attempt to cool down. The examination consisted of a series of credible medical measurements with the application of professional thermal imagining equipment. The above-mentioned study acknowledged the potential of thermal imagining diagnostics in terms of assessing the state of health of the examined subject. In terms of thermal imagining methods usage, it is possible not only to locate the inflamed spots effectively, but also to monitor the course of the treatment of the inflammatory conditions.

Keywords: diagnostics, thermal imagining, thrombosis

Streszczenie

W artykule przedstawiono wykorzystanie termowizji do wykrywania zmian w naczyniach obwodowych, w kończynach dolnych. Jest to możliwe, gdyż na obrazach termowizyjnych zaobserwować można różnice w rozkładzie temperatury, co jest związane z zaburzeniami przepływu krwi. W trakcie badań stwierdzono istotną różnicę w temperaturach między zdrową lewą kończyną (w zależności od przeprowadzonych badań) i chorą prawą („kontrolną"), przed rozpoczęciem i po wykonaniu próby na oziębienie. Badanie składało się z szeregu wiarygodnych pomiarów medycznych z zastosowaniem profesjonalnego sprzętu do diagnostycznego obrazowania zmian temperatury. Wyżej wymienione badania potwierdziły potencjał diagnostyki obrazowania termicznego w zakresie oceny stanu zdrowia badanego pacjenta. Wykorzystanie metody obrazowania termicznego umożliwia, nie tylko skuteczne zlokalizowanie stanu zapalnego, ale również monitoring przebiegu leczenia stanów zapalnych.

Słowa kluczowe: diagnostyka, kamera termowizyjna, zakrzepica

* Ph.D. Eng. Łukasz Ślusarczyk, M.Sc. Eng. Agata Nowak, Institute of Production Engineering, Faculty of Mechanical Engineering, Cracow University of Technology.

1. Introduction

Thermography, also called the thermal imagining method, includes testing that relies on contactless and remote evaluation of the temperature distribution on the surface of the inspected body. This method is based on observing and recording the distribution of the radiation emitted by an infrared body temperature (higher than absolute zero) that is being converted into visible light [1].

Thermographic study enables visualization of the physiological changes in the human body. Through this visualization, it informs directly about the existence of irregularities in the body at an early stage of their occurrence, preventing permanent and irreversible changes from taking place.

Thermographic survey poses no threats to life and health of the test subject. It does not use a radius of X-rays (as in the case of a traditional X-ray imaging) and is to be considered as non-invasive and human-friendly method during the whole course of the examination [2]. The basis of the functioning of the infrared camera is the matrix that bears the possibility of detection (receiving) radiation in the infrared band. The received radiation signal is electronically processed and presented in the form of a graph of the temperature distribution. Temperature charts – being the result of the examination – of the specific areas of the entire body are presented as color images. Color spots displayed with intense shades of red determine the emission of higher temperatures and likewise – the greater the intensity of the blue tones, the more reduced the emission of the infrared radiation [3].

The application of thermography in medicine / medical sciences is based on the search mechanism and monitoring of the possible temperature changes caused by an inflammation of the tissues. The physiological basis for such exploitation is based on the fact that inflammation results in an increased blood supply in a part of the body. The above-mentioned inflammation also causes a localized increase in metabolism at the cellular level, connected to the activity in the body and regeneration process in the area of inflammation. [4, 5].

The more increased the cellular metabolism and the more blood that flows through the data spot, the more heat is produced (referred to as a 'radiation infrared'). This allows to conclude that such a place – clearly distinguished with the infrared image – can be a viable subject to the observations conducted with the infrared camera (rather than parts of the body not affected by an inflammation).

Nowadays, the research thermal imagining is applied while diagnosing Reynaud's phenomenon (accompanying disease for SLE – lupus erythematosus), monitoring and detecting inflammatory spots in the body (i.e. rheumatoid arthritis), detecting breast cancer, other breast diseases and venous circulation in the lower limbs or monitoring specific parts of the body [3, 6].

It should be clearly stated that thermography cannot be used as an independent diagnostic method, monitoring or treatment of any disease. It should rather be used as an optional one, back-up for traditional methods, until the quantitative and qualitative data to support the full value and the reliability of its results is obtained [7, 8].

Depending on the type of the thermal imaging camera, the measurement may be:– exact to indicate the temperature of a particular place – through the use of sensors measuring – or the measurement can rely on observation of changes in the distribution of infrared radiation on the whole surface – detector of observation.

2. Conducted research

The person tested/test subject (treated as a patient):

- Female; aged 26,
- Diagnosed with deep vein thrombosis in the distal-proximal section of the right lower limb. Hormonal drugs used in the treatment of other diseases were determined as a trigger factor for the deep vein thrombosis.
- Confirmation of the disease on the basis of:
  - A preliminary study conducted with the usage of Scale Wells clinical probability of deep vein thrombosis – 'The Scale of Wells' clinical probability of deep vein thrombosis – is used to qualify the patient to a group of small, medium or high probability of the presence of deep vein thrombosis. This scale is extremely useful in clinical practice. The probability of deep vein thrombosis: 0 points – small; 1–2 points – moderate; ≥ 3 – big. Here: 5 points,
  - Determination of D – Dimer – a score of 5 722.8–3958.8 ng/mL,
  - Research – capillaroscopy,
  - Ultrasound examination of venous leg (Doppler). Ultrasound of the right lower limb veins extremity visible: thrombus in the field of extended bays of the soleus muscle, veins posterior tibial and peroneal, heterogeneous thrombus completely fill the extended light popliteal veins, femoral veins, popliteal, femoral vein common initial section of the external iliac vein.

Radiation is divided into 3 ranges: near infrared (0.7–5 microns), medium infrared (5–30 microns), far infrared (30–1000 microns).

Keep in mind that the higher the temperature of a body, the greater the radiation emitted by it. For each body, temperature is a characteristic wavelength at which the radiated power is at its maximum. As temperature increases, the maximum radiation shifts towards shorter wavelengths. For example, for the Sun (reaches a surface temperature equal to 6,000 K), the maximum radiated power is in the wavelength range of 0.5 μm. For the human body (temperature 300 K), the maximum radiated power is in the wavelength range of 10 μm.

The infrared radiation can be presented as a blackbody absorbing all radiation that shines on it, regardless of the angle of incidence, wavelength or power radiation source. We can assume that emittance (the energy flux density emitted by a surface area of the body) of the source of emission is proportional to its temperature. This means that radiation from the infrared range emitted by a body with a temperature is greater than absolute zero. It is proportional to its temperature. From the point of view of the infrared mapping, emissivity of the measured object is really important. The emissivity value is introduced to the reference of blackbody radiation as an effective pattern [2].

Preparation of a subject and the test room

The patient must be present in the testing room for 30 minutes to stabilize the skin surface, as the condition for a stable measurement is to obtain a skin surface temperature – so that the test results could be considered reliable.

There are special requirements for the room where the test is to be carried out.

The guidelines [6, 9]

I. The room in which they are held, infrared measurements should:
- allow convenient placement of measuring devices,
- allow visualization of the entire study area,
- provide comfort for both the researcher and patient,
- the size of the room cannot be less than 6 m^2 (2 × 3 m) – as optimal 12 m^3 (3 × 4 m) or greater, to be considered,
- In practice, it happens that the minimum dimension of the test facility depends on the parameters of optical cameras, such as:
  – The minimum focal length, FOV (Field of View),
  – Spatial resolution IMFOV (Instantaneous Measurement Field of View),
  – Dimensions of the examined object.

The key element of the thermographic measurements is to maintain a constant temperature in the testing room – preferably in the range of 20–24°C. Studies show that the human body cools very quickly, and the next two to three quarters of an hour correspond to the temperature stabilization [1]. It is important that the ambient temperature should be comprised within the optimum range of 18–25°C (below 18°C too rapid cooling occurs, and above 25°C the patient begins to sweat). Proper temperature is extremely important, due to the fact that the measurement of active temperature fluctuations makes it difficult for the later analysis of the results and may contribute to the loss of important data.

Another important measurement parameter is the relative humidity of the air – it determines the heat exchange process. For studies of thermal imagining, it is recommended to maintain a humidity level of 45–55%. In addition, it is recommended to limit the flow of air, because air circulation can cause non-uniform temperature distribution. In the research room, no central heating devices should be placed – such as stoves or radiators. An extremely important issue is also to limit the amount and intensity of the light sources – the most reliable measurement results are those obtained in rooms that are poorly lit.

Before the thermal imaging test, each patient must be acclimatized to the ambient conditions. Acclimatization should take approx. 15–20 minutes.

II. During the acclimatization, the tested area (which will be recorded):
- must be bare – for the process of heat exchange with the environment to stabilize,
- tested area must not be touched, rubbed or leaned on.

III. Preparation of a patient:
- physical activity should be reduced to a minimum,
- it is recommended not to drink hot fluids or eat hot meals a few hours before taking measurements,
- vigorous exercises, drinking alcohol and smoking cigarettes are prohibited,
- usage of any drugs that could cause a change in body temperature,
- application of any cosmetics on the test surface,
- contraindications to the research are also to be indicated on the same day of the physiotherapy treatment, except when we want to assess their impact on changes in temperature.

Compliance with the rules for dealing with the test surface and the preparation of the subject is particularly important in medical research. It has been proven that all factors

mentioned above have an effect on the cardiovascular system, and hence, also the surface temperature distribution. Their effects can be seen on the thermal image, but can also persist on the screen for a period from a few dozen to a several minutes [6, 10, 11].

IV. Preparation of the test

During registration of the thermal images:

- patient should be in a fixed position and in the right distance from the camera,
- distance between the camera and the patient must not be less than 1–1.2 m,
- recorded area of the body must be in the perpendicular position to the lens of the infrared camera,
- during the registration sequence, the researcher should pay attention to the correct focus of the camera.

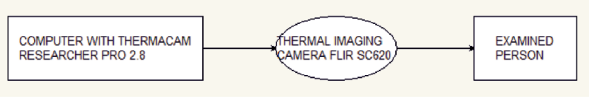

Fig. 1. Diagram of the research position

Fig. 2. Research position

After setting the position, the next stage is the calibration of measuring and control instruments.

The parameters of the thermal imaging camera: [12]

I. Emissivity = 0.98

The most important parameter of the thermal images (which must be correctly entered) is the emissivity. Object materials and their surfaces are characterized in terms of emissivity from 0.1 to 0.95. A highly polished (mirror) surfaces have an emissivity of less than 0.1, oil paint (whatever its color in visible light is) has an emissivity in the infrared region of more than 0.9, human skin exhibits an emissivity close to 1.

II. Ambient temperature

Temperature is a parameter that is used to compensate for the radiation reflected from the object and the radiation emitted by the atmosphere located between the camera and the subject. If the emissivity is low, the distance is large and the temperature of the object is nearly ambient, it is important to adequately compensate for this temperature.

In order to make an accurate temperature measurement, it is necessary to compensate for the effect of other sources of radiation. This is done automatically by the camera, after the introduction of the object parameters:

- emissivity of the object,
- ambient temperature,
- distance between the object and the camera,
- relative humidity.
- Measurements were performed in a separate room:

– constant temperature of 24°C.

III. Humidity 37%

Measuring position (Fig. 2)

- FLIR SC620 thermal imaging camera,
- PC with installed software – ThermaCAM Researcher Pro 2.9,
- thermometer for measuring the temperature in the room,
- hygrometer to measure the humidity in the room,
- camera to capture digital images [additional element].

Due to the need of ensuring proper working conditions for the infrared camera, it is vital for its first launch to take place about 30 minutes before the beginning of the study. During testing, the camera is faced at a fixed distance of 150 cm from the tested patient.

Research

Enter all values: temperature, humidity, distance. There are also other variables necessary to take into account during the research – set the focus of the lens, the position of the LCD display and an overview of the subject. All the factors indicated above allow an assessment of whether: the points of elevated temperature are visible, the measurement is conducted with a suitable distance, the image is proper and the object is in the camera view, whether the elementary angle of view (spatial resolution) is ensured.

By registering thermograms, it is important to make sure that the maximum temperatures do not exceed the upper limit of the measuring range, this would result in a loss of information of the actual value of the maximum temperature of the object. Depending on needs, the appropriate range should be chosen (in this case it is 30–38°C) [3, 7].

Registering a static image of the lower limbs

Thermal image of the temperature ranges from 25 to 40°C, which cannot directly determine the pathologically changed areas.

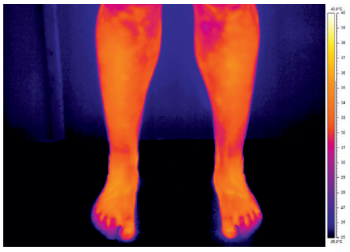

Fig. 3. Thermal image (temperature from 25 to 40°C)

ThermaCAM Researcher allows you to apply one of a number of infrared pallets, which find their application depending on the recorded image type, or effect you want to achieve.

The use of pallets of medical imaging allows for the distinction of pathologically altered areas.

For the temperature range from 25 to 40°C – clearly increased temperature for the right leg (diagnosed with deep vein thrombosis):

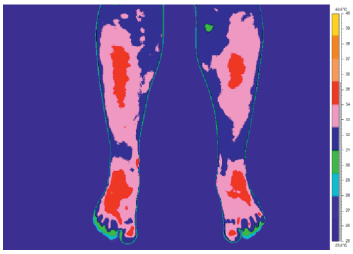

Temperature range from 30 to 36°C – allows better determination of the points (or area) for which the temperature is considerably higher (shown with red ellipses):

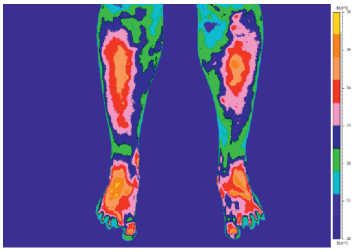

Iron pallet, including a scale in the range from 30 to 36°C and the indication of the area with red ellipse disorder of disease:

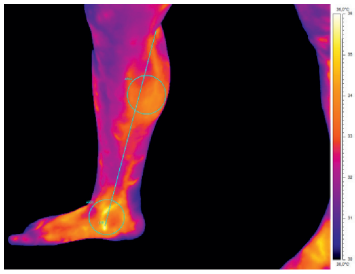

Medical pallet, including a scale in the range of 30 to 36°C:

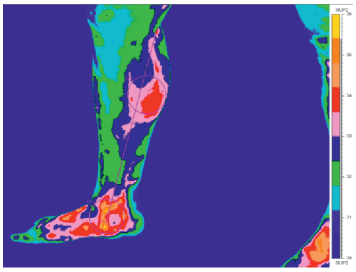

Medical pallet, including a scale in the range of 30 to 36°C

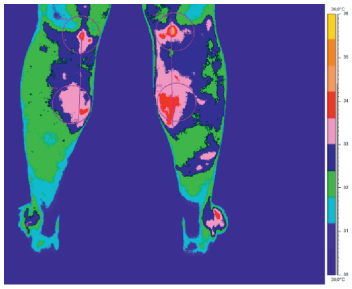

Rain pallet 900, including a scale in the range of 28 to 36°C – used in order to illustrate the lesions and the area rate of the disease more clearly.

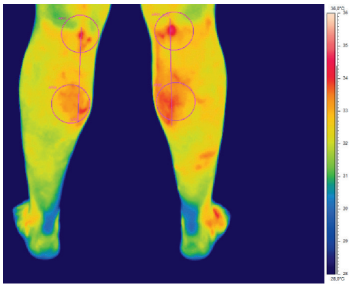

Fig. 4–9. Thermal images

The cooling attempt – applied due to the downward trend in exploration and temperature rise comparing both legs.

I. Registered images of the lower limbs before cooling

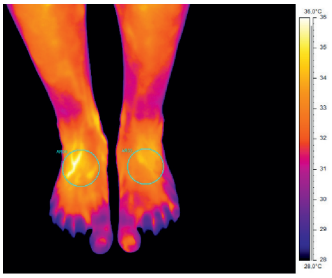

II. Immersion of the legs at time t_1 = 5 minutes in water at T = 20°C

III. Registered images of the lower limb immediately after withdrawing them from water

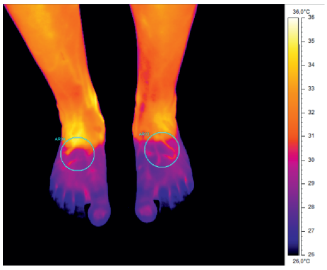

IV. Registered images of the lower limbs after the time t_2 = 5 minutes

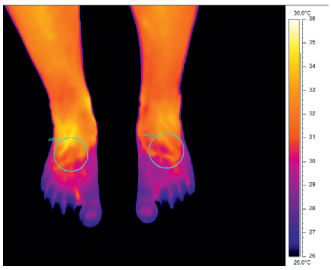

Fig. 10–12 Thermal images – cooling attempt

Findings

Findings obtained during the testing series of thermal images allow to determine the minimum, maximum and average temperature in the analyzed areas of the limbs.

– The maximum and minimum temperature for the sick limbs is 36.1°C and 31.6°C.
– The maximum and minimum temperature for the healthy limb is 34.8°C and 31.1°C.

1.3 ° C is the difference between the maximum temperature values of both legs.

The measured points show abnormalities in blood flow in the vascular system, increased difficulties in the flow and pressure. Studies show that there are significant differences in the average temperature between the healthy and the sick limb.

The differences were shown both before and after an attempt to cool down. Before attempting to cool down, the registered average temperature of the healthy limb was higher than the temperature of the "sick" one by 1.6°C. After cooling the limbs in water at 20°C, average temperature for the patient's limb was higher by 1.2°C. This indicates a faster rise in temperature for the diseased limb, rather than the healthy one.

During the study, significant differences in the occurrence of the higher temperature values were also observed. This is due to the degree of blood circulation in the assessed limbs, both before and after the load of the patient's attempt to cool down (Fig. 10–12).

Infrared thermography as a non-invasive, painless and safe method that helps to specify the physiological state of the examined tissue due to the emission of thermal radiation can reflect the rate of occurrence for these metabolic changes associated with local blood supply. The difference in temperatures is associated with impaired blood supply in comparison to the observed areas of the body, indicating impaired blood flow in the studied area [1, 2].

The thermal images of the lower limbs received during the tests unequivocally illustrate the differences in the temperature distribution within the studied area. Comparing the average value of the temperature before and after cooling down, the sample in the area of the healthy limb and the limb with the deep venous thrombosis has been demonstrated with a higher temperature of the diseased limb [2, 13].

The effectiveness of the ongoing process of the deep vein thrombosis could assist with the thermal imaging diagnostics, directly visualizing the progress of the treatment and rehabilitation. The results of research obtained this way could therefore form the basis for determining the intensity and level of effectiveness of treatment and rehabilitation in the rehabilitation of the patients with a history of disease states of deep vein thrombosis. This is a prerequisite for any further research focused on the application of thermal imaging diagnostics imaging of cardiovascular diseases.

3. Conclusions

In the course of the study, significant increases in the temperature of the right lower limb (in comparison to the left) were found. The study showed the presence of the substantial temperature difference between the left and right lower limb, before and after the performance of the cooling test.

Presumably, research done on a larger group of patients could increase the statistical possibility of testing thermal imaging as a credible medical research.

The above-described thermal imaging studies point to the possibility of using thermal imaging diagnostics in assessing the state of health of the examined person. Finding and monitoring the treatment of the areas affected by the inflammation are possible thanks to the application of thermal imaging methods. Comparing thermal images of the same area, at certain intervals, could help to observe diversification of the production and heat loss to the environment.

The use of thermal imaging makes it possible to detect changes in peripheral vessels in the legs and arms. It is possible due to the fact that, in the images of thermal imaging, the differences in the temperature distribution can be observed, which is associated with impaired blood flow.

An additional benefit of using a thermography test as a method of diagnosis in medicine is the economic problem. Full-size studies can directly show anomalies in the human body due to the detection of inflammations, being indicative of poor health. This would not

save only time, both patient's and physician's, but it also can reduce the cost of medical diagnostics, the whole or a specific area of the body.

Based on the writer's own research, the convergence of methods of thermal imaging by Doppler ultrasound, and others described in the theoretical part of the MSc work [14], was demonstrated. Results of the Doppler ultrasound examination indicate the existence in the right limb of a disease state – deep vein thrombosis. Registration of temperature with the application of infrared camera confirms the presence of areas of elevated temperature – which is indicated by the blood flow disturbances. Thermal imaging method could thus be complementary to conventional methods of diagnosing cardiovascular diseases.

Infrared thermography as a diagnostic method has a high potential in research or diagnostics. It already has a considerable interest in both the scientific and medical communities. Its development potential also provides the ability to determine – at the first contact with the patient – the existence of irregularities in the body, which are visible in the paintings of thermal inflammations characterized by increased temperature values.

Thermal imaging is not yet considered a fully reliable method. While using thermal imaging on humans or animals in particular, only reliable and accurate results must be presented. Please be sure to remember that incorrect measurements lead to erroneous conclusions.

But certainly, summing up the above conclusions, it should be clearly stated that the establishment of a uniform methodology for research thermal imaging as a method of diagnosis has a development potential and needs further study.

References

[1] Jung A., Żuber J., Ring F., *Możliwość zastosowania termografii w diagnostyce medycznej*, Acta Bio-Optica et Informatica Medica Inżynieria Biomedyczna, vol. 14(1), 2008.

[2] Rudowski G., *Termowizja i jej zastosowanie*, WKiŁ, Warszawa 1978.

[3] Bagvathiappan S., Saravanan T., Philip J., Jayakumar T., Ray B., Karunanithi R., Panicker T.M.R., Korath M.P., Jagadeesan K., I*nfrared thermal imaging for detection of peripheral vascular disorders*, Journal of Medical Physics, 34(1), Jan–Mar 2009.

[4] Skrzek A., Anwajler J., Dudek K., Dębiec-Bąk A., Pilch U., *Rozkład temperatury na powierzchni ciała po kriostymulacji ogólnoustrojowej w badaniach termowizyjnych*, Acta Bio-Optica et Informatica Medica Inżynieria Biomedyczna, vol. 13(2), 2007.

[5] Website – Department of Biomedical Engineering PG: http://www.med.eti.pg.gda.pl

[6] Szentkuti A., Kavanagh H.S., Grazio S., *Infrared thermography and image analysis for biomedical use*, Periodicum Biologorum, vol. 113(4), 2011.

[7] Prasał M., Sawicka M.K., Wysokiński A., *Termowizja jako metoda diagnostyczna stosowana w kardiologii*, Kardiologia Polska, vol. 68(9), 2010.

[8] De Mey G., *A model for infrared emissivity*, Materiały konferencji „Termografia i termometria w podczerwieni", Warszawa 1996.

[9] Madura H., *Pomiary termowizyjne w praktyce*, praca zbiorowa, 2004.

[10] Vavilov V.P., *Najnowsze techniki przetwarzania obrazów w badaniach nieniszczących metodami termografii stanów nieustalonych*, Materiały konferencji „Termografia i termometria w podczerwieni", Warszawa 1996.
[11] Minkina W., *Pomiary termowizyjne: przyrządy i metody*, Politechnika Częstochowska, 2004.
[12] http://www.flir.com
[13] Zawilska K, Jaeschke R, Tomkowski W. et al., *Polskie wytyczne profilaktyki i leczenia żylnej choroby zakrzepowo-zatorowej,* Aktualizacja 2009, Med Prakt, 2009.
[14] Nowak A., *Opracowanie metody diagnostycznej zakrzepicy żył głębokich w częściach dystalnych ciała z wykorzystaniem kamery termowizyjnej*, praca magisterska, Kraków 2015.

TECHNICAL TRANSACTIONS | **CZASOPISMO TECHNICZNE**
MECHANICS | MECHANIKA
5-M/2016

DOI: 10.4467/2353737XCT.16.291.6123

ANNA WIŚNIEWSKA, ANETA LIBER-KNEĆ*

INFLUENCE OF A SKIN TISSUE ANISOTROPY ON MECHANICAL HYSTERESIS

WPŁYW ANIZOTROPII TKANKI SKÓRNEJ NA HISTEREZĘ MECHANICZNĄ

Abstract

The mechanical properties of a pig's skin as a human skin substitute in the studies carried out *in vitro* are used in surgery and engineering design. The investigation included the uniaxial tensile test and cyclic loading-unloading tests of a swine skin. The values of dissipated energy and energy dissipation ratio for first, fifth and tenth hysteresis loop of every examined sample were obtained. In the investigation, the skin anisotropy was taken into consideration. The estimation of the influence of various levels of load on the values of the measured parameters was also made.

Keywords: mechanical properties, energy dissipation, skin, animal samples, hysteresis

Streszczenie

Właściwości mechaniczne tkanki skórnej świni jako substytutu skóry ludzkiej w badaniach *in vitro* są wykorzystywane w chirurgii i projektowaniu inżynierskim. Badania obejmowały przeprowadzenie próby jednoosiowego rozciągania oraz wykonanie testów cyklicznego obciążania-odciążenia dla skóry świni. Otrzymano wartości energii dyssypacji oraz współczynnika pochłaniania energii dla pierwszej, piątej i dziesiątej pętli histerezy mechanicznej każdej zbadanej próbki. We wszystkich przeprowadzonych badaniach uwzględniono anizotropową budowę tkanki skórnej. Oceniono także wpływ różnych poziomów zastosowanego obciążenia na wartości mierzonych parametrów.

Słowa kluczowe: właściwości mechaniczne, dyssypacja energii, tkanka skórna, próbki zwierzęce, histereza

* D.Sc. Ph.D. Eng. Anna Wiśniewska, Ph.D. Eng. Aneta Liber-Kneć, Institute of Applied Mechanics, Faculty of Mechanical Engineering, Cracow University of Technology.

1. Introduction

The skin is a non-homogeneous material, which has a complicated multilayered anatomy structure. It displays viscoelastic mechanical properties and *in vivo* it is subjected to a pre-stress, which is unequal distributed on its surface. The areas of reduced tension are mapped by Langer`s lines [1–4]. Their direction is perpendicular to the long axis of muscles lying under the skin [1].

From a mechanical point of view, skin can be treated as a composite material with a highly-hierarchical structure. Due to the complex anatomy structure, skin tissue is a strongly anisotropic material. Basic mechanical properties of the skin are largely influenced by the structural arrangement and orientation of the collagen fibers [5, 6]. The viscoelastic behavior of skin tissue is shown in the hysteresis in the stress-strain relationship. Hysteresis is defined as the energy lost within the tissue between loading and unloading. Hysteresis is caused by internal friction of a material. This internal friction is responsible for dissipating mechanical strain energy to heat. When the skin is stimulated repetitively with constant load peak, the load-deformation curves shift to the right in a load-elongation diagram and the hysteretic effects diminish. By repeated cyclic, eventually a steady state is reached at which no further change will occur (the tissue is preconditioned) unless the cyclic routine is changed [7].

The description of mechanical properties of the skin is still an open question, not only from the theoretical point of view, but also from an experimental aspect. There is no one definite standard that has been established in testing skin tissue. The knowledge obtained in mechanical tests is used in dermatology as well as in traumatology and plastic surgery, especially in view of the aging and fatigue features. It is also used in the engineering design of medical robots and surgical instruments [8].

In the case of the investigation of living tissue, the availability of research material is limited, especially if the study would concern human tissues. An important limit of such tests consists of ethical considerations. Much greater freedom is characterized by investigation of animal tissues. Therefore, in many studies, substitutes are used [9, 10]. These materials have a structure and properties as similar as possible to the original. In the case of the investigation of human skin tissue, a good substitute is swine skin. It has an anatomical structure very similar to that of human skin. Pig`s skin contains dermal collagen and elastic content that is more similar to humans than other laboratory animals [11, 5]. In the literature, the most commonly used tests to characterize pig's skin are uniaxial and biaxial tensile tests and relaxation tests [12, 13]. However, the data obtained in tensile tests are often very different. This difference results from the biological variety among animals, the sensitivity of biological tissues to test and storage conditions of samples, problems with obtaining samples of identical dimensions (e.g. various thickness), as well as from the anisotropic character of the skin [14]. The Young's modulus of the pig's skin varies between 7.6 MPa and 62.6 MPa, the tensile strength varies between 2,5 MPa and 15.7 MPa [12, 15–17].

The aim of the study was an estimation of the influence of skin anisotropy and various levels of load on mechanical hysteresis under cyclic loading-unloading of swine skin.

2. Material and methods

2.1. Samples preparation

In the study, the skin from a domestic pig, which weighed ca. 110 kilograms and was 6 months old, was used. Firstly, patches of skin from the back were extracted. The skin and adipose tissues were separated. Rectangular samples, in the same geometric dimensions: 100 mm in length and 10 mm in width, were made. There is no standard for testing skin tissue and literature review showed that e.g. the width of sample can be in the range between 5 and 12,7 mm [12, 18]. Therefore, the geometry size of skin samples was selected according to PN-EN ISO 527-2. Specimens were taken in three directions: parallel, perpendicular and at an angle 45 degrees (oblique) to the backbone (Fig. 1). The average thickness of the samples was 2,27±0,19 mm.

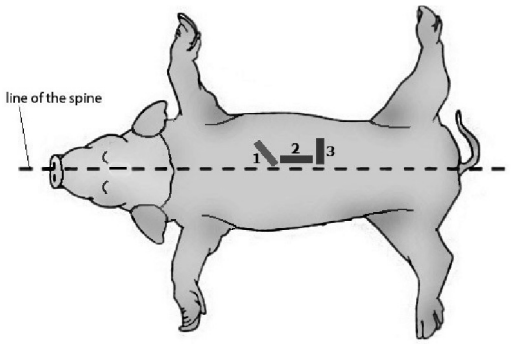

Fig. 1. Direction of samples taken from swine`s back (1 – oblique, 2 – parallel, 3– perpendicular) in relation to the backbone line

In order to better store the biological material, the specimens were frozen at the temperature of –18°C and defrosted in the period of 1 hour at room temperature before the test.

2.2. Research methods

The mechanical properties under static tension were determined with the use of the MTS Insight 50 testing machine. The samples were mounted using flat clamps and they were extended at the speed of 5 mm/min. The measurement base of the sample was 50 mm. Each set of samples for tension testing (the samples divided according to the direction of their taking) contained a minimum of 5 samples. The determined values of mechanical parameters: Young's modulus (E_1 in the first phase of elongation, E_2 in the second phase of elongation), the tensile strength (UTS) and the strain at break were shown as the average values with a standard deviation (X ± SD).

Repeated loading cycles were made for three levels of load: 30 N, 65 N and 100 N and for three directions of the taken samples. The applied tensile load was within the elastic limit of

the skin. The test was made with the use of MTS Insight 50 testing machine. The loading as well as the unloading was conducted at a constant rate of 5 mm/min. Initial sample length was $l_0 = 50$ mm.

The cyclic loading-unloading tests consisted of 10 loading-unloading cycles. Three hysteresis loops for each level of load were registered (first, fifth and tenth). On the basis of the received data, the force-elongation characteristics were obtained. These curves were used to calculate dissipated energy (the area of loop) and energy dissipation ratio (dissipated energy/energy during loading) in each loading cycle. Also, examples of strain versus time curves were shown, and on their basis values of residual strain were calculated. Eighteen samples were taken, two samples for each set of research direction and load level. The calculated values of energy of dissipation, energy dissipation ratio and residual strain were shown with a standard deviation.

3. Results

The anisotropy of the skin tissue had a considerable impact on its mechanical parameters. The research shows that the best mechanical parameters characterized samples taken parallel to the spine. The lowest values were obtained for the perpendicular samples (Tab. 1).

Table 1

The average values of obtained mechanical properties

Research direction (to the backbone)	Maximum force [N]	UTS [MPa]	Strain [%]	Young`s modulus E_1 [MPa]	Young`s modulus E_2 [MPa]
perpendicular	242.42±81.93	10.61±3.18	43.39±8.60	2.35±0.28	35.53±3.97
parallel	522.70±95.91	22.06±3.31	45.16±3.68	2.46±0.35	72.28±6.56
oblique (45°)	484.26±55.66	21.18±2.32	44.32±5.91	2.39±0.27	63.89±8.75

As a result of the cyclic loading-unloading tests of the swine skin tissue, stress-strain characteristics for the three various load levels (30 N, 65 N, 100 N) and with respect to skin's anisotropy were obtained (Fig. 1 to 3).

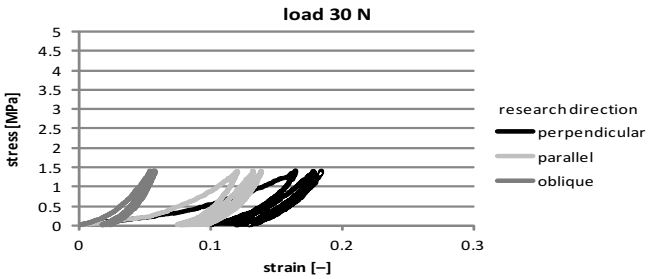

Fig. 2. Comparison of hysteresis loops (1st, 5th and 10th) obtained under load of 30 N for three directions of samples taken

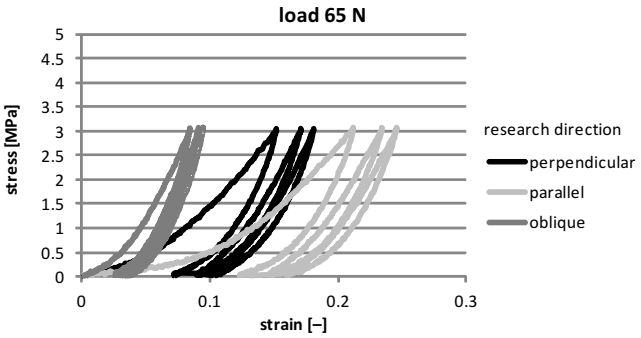

Fig. 3. Comparison of hysteresis loops (1st, 5th and 10th) obtained under load of 65 N for three directions of samples taken

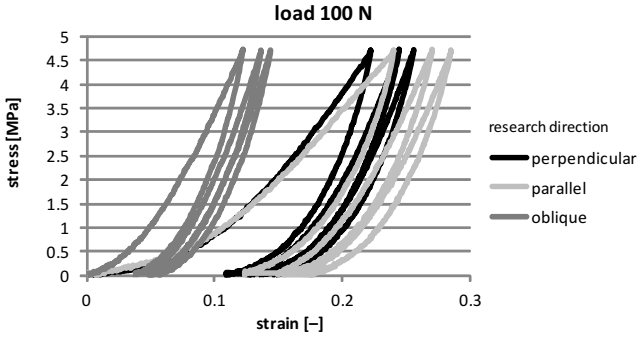

Fig. 4. Comparison of hysteresis loops (1st, 5th and 10th) obtained under load of 100 N for three directions of samples taken

The maximum value of the stress reached at the load of 30 N was 1.42 MPa (peaks of each hysteresis loops). For the last, tenth loop, the value of the maximum strain was 18.4–18.6% for perpendicular samples, 12.1–13.8% for parallel samples and 4.8–5.8% for oblique samples (Fig. 2). When the load of 65 N was used, the maximum value of the stress was 3.08 MPa. Instead, the value of the maximum strain for the last loop was in the range of 18.1–18.7% (perpendicular samples), 24.6–25.2% (parallel samples), 9.5–10.7% (oblique samples). The application of load of 100 N resulted in obtaining maximum stress with a value of 4.73 MPa. The values of the maximum strain for the tenth loop were 24.8–25.5% for the perpendicular samples, 25.4–28.4% for the parallel samples and 14.3–21.5% for the oblique samples.

In Figs. 2 to 4, difference between the area of the first hysteresis loop and the following loops have been seen. At every examined load level and research direction, the first hysteresis loop had a definitely higher value of the surface area than other loops. The values of the surface area of each registered loop were calculated and shown as energy of dissipation in Figs. 5 to 7. The highest value of the energy dissipated was observed in the first cycle of loading-unloading test (in the first hysteresis loop) for all directions of the taken samples. An increase of the number of loading cycles caused a decrease of the value of dissipated

energy. The percentage reduction of these values was presented in Tab. 2. For perpendicular samples under the load of 30 N, the average value of energy dissipation for the first loop was 56.79±0.81 mJ. The average value of the energy dissipation for the first loop for parallel samples under the load of 30 N was 31.72±3.94 mJ. The smallest differences between each loop were shown for oblique samples. The average value of energy dissipation for the first loop (under the load of 30 N) was 8.7±0.91 mJ.

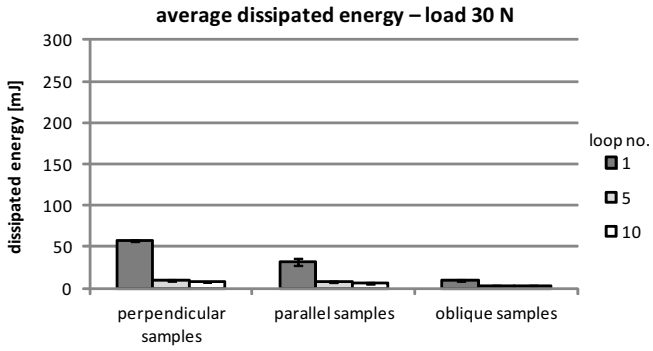

Fig. 5. Values of dissipated energy under the load of 30 N

Under the load of 30 N, for the perpendicular samples the value of dissipated energy was the highest (Fig. 5). At this load level, parallel samples exhibited less ability to energy dissipation. Oblique samples obtained the worst result. The level of applied load (30 N) corresponded to the first phase of elongation test, in which elastin fibres are mainly responsible for the stretching mechanism. At this stage, collagen fibers remain folded, so their contribution in energy absorption is negligible [19, 20]. Therefore, in the case of low value of load, participation of more oriented collagen fibers in parallel samples had no effect on energy dissipation. At larger loads, parallel samples absorbed more energy than perpendicular and oblique samples (Fig. 3 and 4). This may results from the fact that most of the collagen fibers are arranged longitudinally to the line of the spine of animals and energy supplied to the skin is partly dissipated by collagen fibers during their ordering in the direction of the applied force [18].

The highest value of the energy has been dissipated during investigation of parallel samples. For the first loop, the average value of energy dissipation for parallel samples was 124.95±9.89 mJ. For perpendicular samples, the average value of dissipated energy in the first loop (under the load of 65 N) was 92.72±1.44 mJ. The smallest differences between each loop for oblique samples can be seen. The average value of energy dissipation for the first loop was 35.38±2.60 mJ.

For perpendicular samples, in the first loop, the average value of energy dissipation was 189.98±14.13 mJ. The greatest values of dissipated energy for parallel samples can be seen. The average value of this parameter, at this load level (100 N), for the first loop, was 198.29±72.53 mJ. The smallest values of energy dissipation were for oblique samples. In the first loop the average value of this energy was 125.48±45.02 mJ. In the case of the highest value of applied load as well as parallel and oblique samples, the large spread of the average

value of energy dissipation can be seen. These results may be caused by differences in the specimens' thickness or the area of the taken specimen, and requires testing with the use of a larger number of samples.

Table 2

Differences of values of energy dissipation between loops under the load of 30 N

Research direction	Loop no.	Percentage reduction of values of energy dissipation (relative to the first loop)%		
		30 [N]	65 [N]	100 [N]
perpendicular	5	83.39	75.75	76.81
perpendicular	10	87.92	77.79	79.93
parallel	5	77.55	76.33	75.70
parallel	10	80.88	80.64	79.61
oblique	5	66.95	61.45	70.53
oblique	10	70.46	65.72	73.67

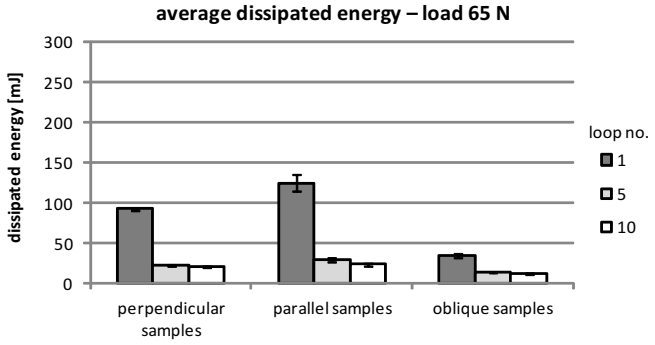

Fig. 6. Values of dissipated energy under the load of 65 N

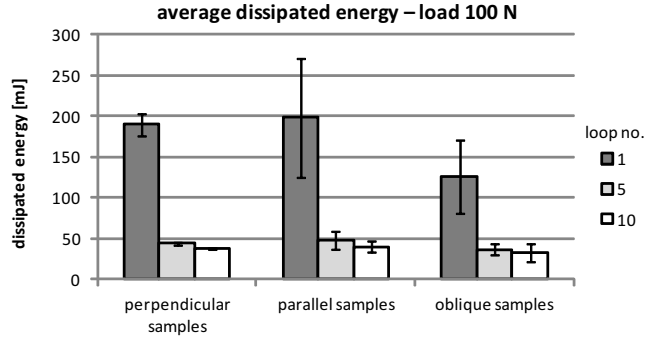

Fig. 7. Values of dissipated energy under the load of 100 N

Analyzing data from the above graphs (Fig. 5–7) relatively slight differences between values of energy dissipation for fifth and tenth loop in the margin of error can be noticed. This results from a certain stabilization of this parameter after few loading-unloading cycles.

By analyzing the obtained values of the energy dissipation ratio (Fig. 8–10), the fact that, at each load level, an increase of the number of loading cycles caused a decrease of the values of this ratio, may be seen. Differences between values of the energy dissipation ratio for fifth and tenth loop were inconsiderable. This is the result of stabilization of this parameter after few load-unload cycles.

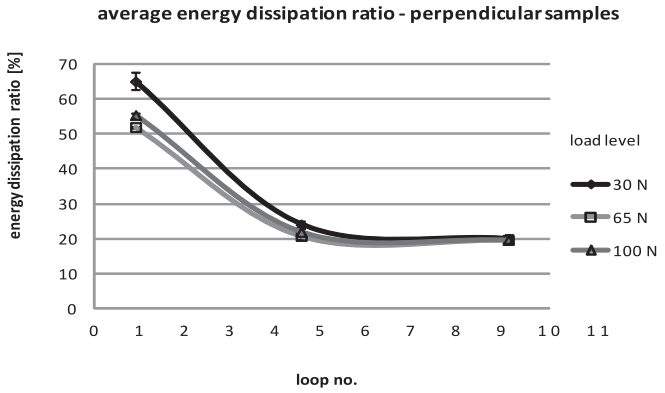

Fig. 8. Values of energy dissipation ratio under three load levels for perpendicular samples

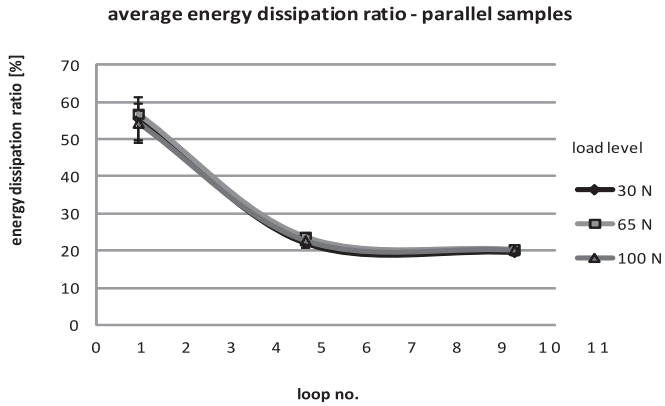

Fig. 9. Values of energy dissipation ratio under three load levels for parallel samples

In Fig. 11, examples of strain versus time curves under the load of 30 N were shown. The stages of cyclic loading-unloading can be recognized for these curves. In the loading phase, the value of strain increased and in the unloading phase, it decreased to the value of residual strain which occurred immediately after the first loading-unloading cycle. This behavior resulted from the viscoelastic nature of skin tissue. In Tab. 3, the values of residual strain for

the tested samples were shown. The values of residual strain increased with the number of loading cycles (number of hysteresis loops). The highest values of residual strain under the load of 30 N were obtained for perpendicular samples and under higher loads for parallel samples. This trend was similar to that observed in the case of energy of dissipation.

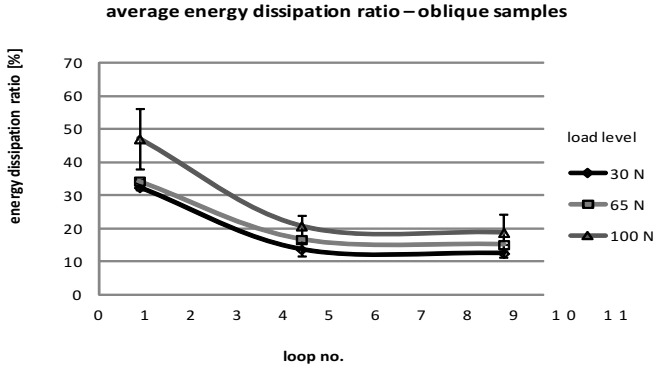

Fig. 10. Values of energy dissipation ratio under three load levels for oblique samples

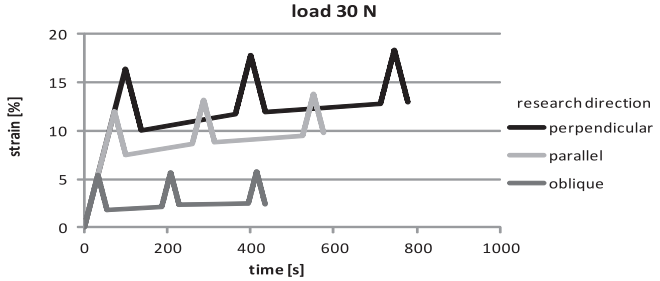

Fig. 11. Examples of strain versus time curves under the load of 30 N

Table 3

Comparison of values of residual strain for tested samples

Load [N]	Loop no.	Residual strain [%]		
		Perpendicular	Parallel	oblique
30	1	10.59±0.79	6.09±1.97	1.45±0.47
	5	12.50±0.78	7.43±1.95	1.90±0.60
	10	13.32±0.48	8.41±1.95	2.01±0.53
65	1	7.44±0.29	11.76±0.82	2.91±0.41
	5	9.50±0.41	14.59±0.27	3.60±0.39
	10	10.41±0.12	16.19±0.21	3.91±0.54
100	1	11.61±1.04	12.36±0.08	6.25±3.49
	5	14.06±0.66	15.05±0.39	7.95±4.39
	10	15.02±0.54	16.57±1.14	8.89±4.58

4. Conclusion

The results confirm that like human skin, pig skin is a highly dissipative material exhibiting non-linear mechanical behavior. Based on the research of the mechanical properties obtained in the uniaxial tensile test and cyclic loading-unloading tests of the skin tissue samples taken in three directions in relation to the swine`s backbone, the huge influence of anisotropy of the skin on its properties can be confirmed. The conducted uniaxial tensile test showed that the best mechanical parameters were obtained for the parallel samples. The lowest values were revealed by the perpendicular samples. Instead, oblique samples medium values of every obtained parameter were achieved. The mechanical parameters of the swine skin are comparable with values describing the human skin [19, 21]. This confirmed that swine skin is a good material for the substitution of human skin in vitro researches.

The test under loading and unloading showed that the skin anisotropy influenced on mechanical hysteresis. At a low load level (30 N) the perpendicular samples obtained the highest value of dissipated energy. But at a higher load level (65 N, 100 N), the highest value of dissipated energy was achieved by parallel samples. At every examined load level for oblique direction of samples taken, the smallest surface area of hysteresis loops was observed. The increase of load values resulted in a higher value of the dissipated energy for all directions of samples taken. The stabilization of the value of energy dissipation between fifth and tenth loop was shown. Similar results were obtained for dog skin by Bismuth et al. [21]. At every examined load level, the first hysteresis loop had a higher surface area than other loops. This tendency was in reasonable agreement with the results obtained by Ehret et al. [22].

Characterization of the mechanical properties of pig skin is important and allows for it to be used as an animal model for human skin disease. Skin hysteresis is especially useful to absorb the energy from high forces that may be experienced during accidental impacts.

References

[1] Szotek S., Będziński R., Kobielarz M., Gąsior-Głogowska M., Komorowska M., Maksymowicz K., Hanuza J., Hermanowicz K., *Właściwości skóry ludzkiej uzyskane w testach mechanicznych i techniką spektroskopii Ramana*, Engineering of Biomaterials (Inżynieria Biomateriałów), vol. 12(89–91), 2009, 207–209.

[2] Arumugam V., Naresh M.D., Sanjeevi R., *Effect of strain rate on the fracture behaviour of skin*, Journal of Biosciences, vol. 19(3), 1994, 307–313.

[3] Gallagher A.J., Ní Anniadh A., Bruyere K., Otténio M., Xie H., Gilchrist M.D., *Dynamic Tensile Properties of Human Skin*, IRCOBI Conference Proceedings, 2012.

[4] Edwards Ch., Marks R., *Evaluation of Biomechanical Properties of Human Skin*, Clinics in Dermatology, vol. 13(4), 1995, 375–380.

[5] Shergold O.A., Fleck N.A., Radford D., *The uniaxial stress versus strain response of pig skin and silicone rubber at low and high strain rates*, International Journal of Impact Engineering, vol. 32(9), 2006, 1384–1402.

[6] Ní Annaidh A., Bruyere K., Destrade M., Gilchrist M.D., Maurini C., Otténio M., Saccomandi G., *Automated estimation of collagen fibre dispersion in the dermis and its contribution to the anisotropic behaviour of skin*, Annals of Biomedical Engineering, vol. 40(8), 2012, 1666–1678.
[7] Fung Y.C., *Biomechanics. Mechanical properties of living tissues*, Springer, USA, 1993.
[8] Misra S., Ramesh K.T., Okamura A.M., *Modeling of Nonlinear Elastic Tissues for Surgical Simulation*, Computer Methods in Biomechanics and Biomedical Engineering, vol. 13(6), 2010, 811–818.
[9] Karimi A., Rahmati S. M., Navidbakhsh M., *Mechanical characterization of the rat and mice skin tissues using histostructural and uniaxial data*, Bioengineered, vol. 6(3), 2015, 153–160.
[10] Wang Y., Marshall K.L., Baba Y., Lumpkin E.A., Gerling G.J., *Compressive Viscoelasticity of Freshly Excised Mouse Skin Is Dependent on Specimen Thickness, Strain Level and Rate*, PLoS One, vol. 10(3), 2015.
[11] Swindle M.M., Makinhttp://vet.sagepub.com/content/49/2/344.full-aff-2 A., Herronhttp: //vet.sagepub.com/content/49/2/344.full-aff-3 A.J., Clubb Jr F.J., Frazier K.S., *Swine as Models in Biomedical Research and Toxicology Testing*, Veterinary Pathology, vol. 49 (2), 2012, 344–356.
[12] Żak M., Kuropka P., Kobielarz M., Dudek A., Kaleta-Kuratewicz K., Szotek S., *Determination of the mechanical properties of the skin of pig fetuses with respect to its structure*, Acta of Bioengineering and Biomechanics, vol. 13 (2), 2011, 37–43.
[13] Liu Z., Yeung K., *The preconditioning and stress relaxation of skin tissue*, Journal of Biomedical and Pharamaceutical Engeeniring, 2:1, 2008, 22–28.
[14] Geerligs M., *Skin layer mechanics*, Ph.D. Thesis, Technische Universiteit Eidhoven, 2010, 27–30.
[15] Łagan S., Liber-Kneć A., *Charakterystyka anizotropowych właściwości mechanicznych skóry świni*, Engineering of Biomaterials (Inżynieria Biomateriałów), vol. 17(128–129), 2014, 61–63.
[16] Lim J., Hong J., Chen W.W., Weerasooriya T., *Mechanical response of pig skin under dynamic tensile loading*, International Journal of Impact Engineering, vol. 38, 2011, 130–135.
[17] Pailler-Mattei C., Bec S., Zahouani H., *In vivo measurements of the elastic mechanical properties of human skin by indentation tests*, Medical Engineering & Physics, vol. 30(5), 2008, 599–606.
[18] Ní Annaidh A., Bruyere K., Destrade M., Gilchrist M. D., Otténio M., *Characterising the Anisotropic Mechanical Properties of Excised Human Skin*, Journal of the Mechanical Behavior of Biomedical Materials, vol. 5(1), 2012, 139–148.
[19] Hendriks F. M., *Mechanical Behaviour of Human Skin in Vivo*, Nat.Lab. Unclassified Report 820, Philips Research Laboratories, 2001.
[20] Szotek S., Będziński R., Kobielarz M., Żywicka B., Pielka S., Kuropka P., *Badanie właściwości mechanicznych skóry*, Engineering of Biomaterials (Inżynieria Biomateriałów), vol. 11(81–84), 2008, 77–79.

[21] Bismuth C., Gerin C., Viguier E., Fau D., Dupasquier D., Cavetier L., David L., Carozzo C., *The biomechanical properties of canine skin measured in situ by uniaxial extension*, Journal of Biomechanics, vol. 47, 2014, 1067–1073.

[22] Ehret A.E., Hollenstein M., Mazza E., Itskov M., *Porcine dermis in uniaxial cyclic loading: sample preparation, experimental results and modeling*, Journal of Mechanics of Materials and Structures, vol. 6(7–8), 2011, 1125–1135.

CONTENTS

TREŚĆ